

Wave Simulation in Truncated Domains for Offshore Applications

Wave Simulation in Truncated Domains for Offshore Applications

Proefschrift

ter verkrijging van de graad van doctor
aan de Technische Universiteit Delft,
op gezag van de Rector Magnificus prof. ir. K.C.A.M. Luyben,
voorzitter van het College van Promoties,
in het openbaar te verdedigen op vrijdag 13 januari 2012 om 12:30 uur door

Petrus Reinier WELLENS

ingenieur offshore techniek
geboren te Rotterdam

Dit proefschrift is goedgekeurd door de promotoren:

Prof. dr. ir. R.H.M. Huijsmans

Prof. dr. A.E.P. Veldman

Samenstelling promotiecommissie:

Rector Magnificus voorzitter

Prof. dr. ir. R.H.M. Huijsmans Technische Universiteit Delft, promotor

Prof. dr. A.E.P. Veldman Rijksuniversiteit Groningen, promotor

Prof. dr. P. Ferrant École Centrale de Nantes

Prof. dr. ir. W.S.J. Uijtewaal Technische Universiteit Delft

Prof. dr. ir. B. Koren Rijksuniversiteit Leiden

Dr. ir. M.J.A. Borsboom Deltares

Dr. ir. T. Bunnik MARIN

Prof. dr. ir. J.A. Pinkster Technische Universiteit Delft, reservelid

This research was financially supported by the Dutch technology foundation STW (grant GWI.6433).

ISBN 978-94-6169-196-5

©Peter Wellens, 2012. No part of this book may be reproduced, stored in a retrieval system, or transmitted in any form or by any means without permission from the author.

The photograph on the cover shows La Jument, a lighthouse 300m off the coast of Ushant Island, Brittany, France. The photograph was taken by Jean Guichard (www.jean-guichard.com) and made available to the author for illustrating the cover of this thesis, for which Mr. Guichard is gratefully acknowledged.

Typesetting by L^AT_EX 2_ε.

Printed by Optima Grafische Communicatie, Rotterdam.

Summary

Wave Simulation in Truncated Domains for Offshore Applications

Subject and main objective

There is a desire to assess extreme wave loads on offshore structures like Floating Production, Storage and Offloading (FPSO) vessels, either for design, or for evaluation when circumstances near the structure change. Design formulae for extreme wave loads are scarce and have limited validity for specific structures. Simplified theory, such as linear potential theory, which is often used for motion analysis of offshore structures, does not represent the hydrodynamics involved in a wave impact with sufficient accuracy. For this reason, extreme wave loads are often assessed in physical experiments at model scale. Extreme wave loads may also be simulated by means of detailed numerical modeling. COMFLOW is the name for a numerical method specifically developed for simulating wave impact events. Simulation of wave impacts on offshore structure with COMFLOW is the subject of this thesis.

Simulations should represent wave interaction with the structure as if it were out at sea. For reasons of efficiency, the computational domain can not be much larger than the offshore structure it contains. Wave simulation in computational domains of limited size requires special measures to reduce spurious reflection of waves at the boundaries of the domain. The main objective of this thesis is to find or develop means to efficiently reduce spurious reflection from the boundaries in COMFLOW.

Numerical method

COMFLOW is based on the Navier-Stokes equations. For the derivation of the numerical method in COMFLOW, a finite volume discretization for Cartesian grids has been adopted. The discretization yields a skew-symmetric operator for the convective term and a symmetric operator for the viscous term in the momentum equation, resembling the symmetry properties of the analytical operators. Forward Euler time discretization is applied, in which the pressure term is evaluated implicitly. Substituting the discrete momentum equation in the discrete continuity equation gives a Poisson equation for the pressure which is solved iteratively by means of Successive

Over-Relaxation (SOR) with an optimal choice for the relaxation coefficient in case the absorbing boundary condition derived in this thesis is not applied in the simulation. When the absorbing boundary condition is required, the Poisson equation (with additional terms resulting from the discretization of the absorbing boundary condition that do not fit the typical Poisson-stencil) is solved with a general sparse-matrix solver, in which the stabilized Bi-Conjugate Gradient (BiCGSTAB) iteration method is combined with an Incomplete Lower-Upper preconditioner (ILU(ϵ)).

The free surface in COMFLOW is advected by means of an improved Volume of Fluid (iVOF) algorithm. The improvement consists of a local height function that aggregates fluid in a stencil of three cells in all spatial directions when fluxing fluid. The local height function reduces mass loss and so-called flotsam and jetsam, a numerical artifact consisting of disconnected droplets of fluid approximately one grid cell in size.

Spurious wave-energy dissipation

In coarse-grid simulations, a specific amount of grid-size-dependent numerical viscosity is applied to obtain a velocity field without spatial instabilities, effectively resulting in a first-order upwind discretization of the convective term in the momentum equation. Upwind discretization induces spurious wave energy dissipation, which is undesirable because it reduces the forces involved in a wave impact on the structure. As a result, the grid size needs to be chosen sufficiently fine to make sure that the structure in the simulation endures the full impact for the wave condition that was specified. A better discretization than first-order upwind for the convective term can reduce spurious wave-energy dissipation. With a better discretization the grid size can be chosen less fine, resulting in more efficient simulations.

In this thesis, a Lax-Wendroff discretization with a min-max flux limiter was evaluated for the convective term in the momentum equation in simulations with standing waves. Standing wave simulations are an efficient means to investigate the effect of different discretizations on the reduction of wave energy dissipation, because all the physics of wave motion are included without disturbances from incoming wave or absorbing boundary procedures. The reduction of wave-energy dissipation with Lax-Wendroff discretization was limited compared to first-order upwind discretization of the convective term in the momentum equation.

It was hypothesized and found that also the free surface displacement algorithm was a source for wave-energy dissipation, because VOF with piecewise-constant interface reconstruction (Simple Line Interface Construction, SLIC) includes a first-order upwind discretization of the fluid flux. The discretization of the fluid flux can be improved when Piecewise-Linear Interface Construction (PLIC) is adopted. The reduction of wave-energy dissipation of PLIC compared to SLIC was limited as well.

A considerable decrease of the wave-energy dissipation was only obtained by combining PLIC in the free surface displacement algorithm with Lax-Wendroff discretization of the convective term in the momentum equation in propagating wave simulations. In these simulations, the combination of PLIC and Lax-Wendroff gives 2% wave-energy dissipation over two wave lengths, whereas the original combination of SLIC and first-order upwind in the convective term gives 18% wave-energy dissipation.

Wave generation

In COMFLOW, waves are commonly generated by specifying velocities as a Dirichlet boundary condition at the inflow. The velocities originate from wave theory. Well-known wave theories for steep waves are Stokes 5th order theory and stream function theory (Rienecker-Fenton), for which analytical solutions are available. In this thesis, Rienecker-Fenton solutions are used to generate regular waves at the boundary. It was investigated how well COMFLOW represents these analytical solutions by means of a grid convergence study. We considered both the free surface elevation and the vertical profile of the horizontal velocity two wave lengths away from the inflow boundary. The free surface in wave crests was approximated reasonably well by COMFLOW for the finest grid that was considered; in wave troughs, however, there remained a considerable difference between COMFLOW and the analytical solution. The reason for the differences during wave troughs is not well understood and further research is required. Also for the velocity profile during a wave crest there were differences: not at the free surface, where we would have expected them because of the large gradients in the velocity, but the differences were mainly near the bottom. This is also part of continued research.

Steep irregular waves were generated in COMFLOW by using velocities from linear wave theory with multiple frequency components, and by using velocities obtained from solutions of a Finite-Difference Finite-Element Method (termed FDFEM in this work), which is a non-linear potential flow solver. The two generation methods were compared as follows. The solution for the surface elevation from the FDFEM method at a certain location was used as a reference solution. Velocity output from the FDFEM solution was taken two wave lengths' distance before the reference location and imposed onto the COMFLOW domain. The COMFLOW solution at the reference location was then compared to the reference solution. It was found that the COMFLOW solution for the free surface elevation agrees well with the FDFEM solution.

A similar procedure was applied for wave generation with velocities obtained from linear theory, but now the surface elevation from the FDFEM solution some distance before the reference location was used. This surface elevation was decomposed into its Fourier-components. For each component, linear potential theory gives the velocities and the combination of all these velocities provides the total velocity signal that is imposed onto the COMFLOW domain as a boundary condition. Again, the COMFLOW solution for the free surface at the reference location was compared to the FDFEM solution. Now, it was found that there are differences between the two solutions that do not decrease with increasing grid resolution. It is therefore concluded that linear theory should not be used for irregular wave generation when the COMFLOW solution is to be compared with experimental results.

Reducing spurious wave reflection at domain boundaries

Waves reflect from computational domain boundaries when no special measures are taken to prevent reflection. Dissipation zones are often used near domain boundaries

to induce a rapid decrease of wave energy so that when waves reach the boundary and reflection occurs, the wave height has reduced to such an extent that spurious reflection does not interfere with the processes near the structure.

Dissipation zones need to be several wave lengths long to be effective. In many cases, the part of the computational domain taken up by dissipation zones exceeds the size of the domain in which the wave interaction with the structure actually occurs. Dissipation zones take up a considerable amount of the total computational effort required for the simulation. Local absorbing boundary conditions are a more efficient alternative to dissipation zones. In this thesis, a local absorbing boundary condition for long-crested irregular waves is derived that is more efficient and more effective than a two-wave-lengths-long dissipation zone.

The absorbing boundary condition in this study includes an approximation of the dispersion relation which is accurate within a range of wave numbers (or, equivalently, frequencies). It also includes second-order vertical derivatives of the solution variables along the boundary. The differential equation for the absorbing boundary condition is discretized implicitly, combined with the discrete momentum equation and included in the Poisson equation for the pressure. Theoretically, the reflection coefficient, i.e. the ratio of outgoing wave amplitude and reflected wave amplitude, for this absorbing boundary condition can be as low as 2% for wave components within the range $0 < kh \leq 6$. In actual wave simulations with this boundary condition, the obtained reflection coefficient was 5%. There are two main reasons for the difference between the theoretical value for the reflection coefficient and the one that was obtained in simulations: 1. linear potential theory was used to derive the absorbing boundary condition, whereas the equations that COMFLOW solves for are non-linear; 2. the second-order vertical derivative cannot be solved near the free surface and needs to be approximated. The approximation used near the free surface is rather crude and requires attention in future research.

Validation in 3D

Experiments with a schematized model of a semi-submersible in waves were performed at MARIN. Waves were generated with a pivoting wave maker at one end of the basin. At the other end, a parabolic beach was installed to reduce spurious wave reflection. The model, which was approximately 1m long, was placed in the middle of the basin and was kept restrained during the experiment. Pressure sensors and wave gauges were placed at several locations around the columns of the model. Also the deck of the model was fitted with pressure sensors. During the experiments, there was violent wave interaction with the model: wave impacts occurred on both columns and many also reached the deck.

In COMFLOW, a similar setup was created. The computational domain extended over the full width of the basin. The side walls of the domain (x-z planes) were configured to represent the side walls of the basin. The incoming-wave boundary (x-y plane) was positioned approximately one typical wave length in front of the structure. Here, waves were generated by specifying the kinematics obtained from an FDFEM simulation that contained the entire basin, including wave maker and

spending beach. At the outflow end of the computational domain in COMFLOW, the absorbing boundary condition derived in this study was applied.

For stability reasons, the FDFEM simulation was performed with a relatively coarse grid and with a smaller water depth than the basin. For this reason, the waves in this simulation could only compare reasonably well to the waves in the experiment. And there was another issue. The position of the model relative to the wave board was not recorded with sufficient precision. At multiple output locations, the free surface elevation in the FDFEM simulation was compared to the free surface in an undisturbed test (without structure). The position where the simulation results best resemble the measurements was selected as most likely location for the model in the simulation.

Keeping in mind that the waves in the simulation were slightly different from the waves in the experiment - not only as a result of model errors, but also because the true water depth in the experiment could not be represented in the FDFEM simulation the comparison between COMFLOW and the experiment turns out rather well. Pressures and surface elevations in COMFLOW show good agreement with the measurements.

The 3D validation of COMFLOW was also an important test for the absorbing boundary condition that was developed in this thesis. The simulations show that the boundary condition can be applied in practical simulations with good results. These simulations could not be performed with a dissipation zone on a desktop computer, because with a dissipation zone it did not fit in memory. It would have been interesting to compare results between a 3D simulation with an absorbing boundary condition and one with a dissipation zone. On the other hand, we can conclude that the absorbing boundary condition enables us to perform simulations that could not be run on a desktop PC before the boundary condition was there.

Samenvatting

Golfsimulaties voor Offshoretoepassingen in Domeinen van Beperkte Grootte

Onderwerp en doel

Er is de wens om extreme golfbelastingen op offshore constructies zoals Floating Production Storage and Offloading schepen (FPSO's) te kwantificeren, ofwel voor ontwerpdoeleinden, ofwel om nieuwe omstandigheden voor een constructie te beoordelen. Er zijn maar weinig ontwerpformules voor extreme golfbelastingen en ze zijn slechts beperkt geldig voor specifieke constructies. Vereenvoudigde vergelijkingen, zoals bijvoorbeeld die uit lineaire potentiaaltheorie voor golven, worden vaak gebruikt om bewegingsanalyses te doen, maar ze geven de hydrodynamica in een golfklap slechts beperkt weer. Om deze reden worden meestal experimenten op modelschaal uitgevoerd wanneer golfklappen belangrijk worden geacht. Extreme golfbelastingen kunnen echter ook met numerieke methodes gesimuleerd worden. Een numerieke methode die ontworpen is voor het simuleren van golfklappen, hebben we COMFLOW genoemd. Het simuleren van golfklappen op offshore constructies met COMFLOW is het onderwerp van dit proefschrift.

In simulaties moet de golfinteractie met de constructie worden gerepresenteerd zoals het op zee gebeurt. Het is niet efficiënt als het rekendomein heel veel groter is dan de constructie die gemodelleerd wordt. Golfsimulaties in een rekendomein van beperkte grootte vragen om extra aandacht voor randvoorwaarden om ongewenste reflectie van golven bij de randen van het domein te reduceren. Het voornaamste doel van dit onderzoek is om randvoorwaarden te vinden of te ontwikkelen om ongewenste reflectie bij de randen in COMFLOW te reduceren.

Numerieke methode

COMFLOW is gebaseerd op de Navier-Stokes vergelijkingen. Een Eindige Volumediscretizatie op een Cartesisch rooster is gebruikt om de numerieke methode af te leiden. Na discretizatie worden een scheef-symmetrische operator voor de convectieve term en een symmetrische operator voor de visceuze term verkregen; dat zijn dezelfde

symmetrieeigenschappen die de operatoren op continu niveau hebben. Voor de discretizatie in de tijd gebruiken we een Forward Eulermethode met de druk impliciet. Het substitueren van de discrete impulsvergelijking in de discrete continuïteitsvergelijking leidt tot een Poissonvergelijking voor de druk, die iteratief wordt opgelost. In veel simulaties wordt van Successive Over-Relaxation (SOR) met een optimale keuze voor de relaxatiecoëfficiënt gebruik gemaakt. In het geval van golfsimulaties met de randvoorwaarde die in dit proefschrift is afgeleid, kiezen we een gestabiliseerde Bi-Conjugate Gradient (BiCGSTAB) iteratiemethode, met een Incomplete Lower-Upper preconditioner (ILU(ϵ)).

Het vrij oppervlak in COMFLOW wordt verplaatst met een verbeterde Volume-of-Fluidmethode (iVOF). De verbetering bestaat eruit dat een lokale hoogtefunctie is gedefinieerd om vloeistof binnen een stencil van drie cellen in alle ruimtelijke richtingen, gezamenlijk te verplaatsen. Door de lokale hoogtefunctie wordt massabehoud verbeterd en wordt zogenoemde 'flotsam en jetsam' gereduceerd. Dit laatste is een benaming voor een numeriek artefact waarbij druppels met de afmeting van ongeveer een roostercel losraken van het voornaamste vloeistofdeel en niet meer verplaatst kunnen worden.

Ongewenste dissipatie van golfenergie

In simulaties op een grof rooster is een zekere hoeveelheid artificiële viscositeit nodig om een snelheidsveld zonder instabiliteit in de ruimte te krijgen. Effectief wordt met deze viscositeit een eerste-orde upwinddiscretizatie voor de convectieve term in de impulsvergelijking verkregen. Eerste-orde upwind leidt tot ongewenste dissipatie van golfenergie, waardoor golfklappen op de constructie wel eens niet zo hard zouden kunnen aankomen als de bedoeling was. Het rekenrooster moet fijn genoeg worden gekozen om de dissipatie terug te brengen tot een acceptabel niveau en zo de golfklap in zijn volle sterkte te laten plaatsvinden. Met een betere discretizatie dan eerste-orde upwind in de convectieve term van de impulsvergelijking, kan de dissipatie van golfenergie worden teruggebracht. Het rekenrooster kan dan grover worden gekozen, waardoor mogelijk sneller gerekend kan worden.

In dit proefschrift hebben we een Lax-Wendroffdiscretizatie met een min-max fluxlimiter in de convectieve term van de impulsvergelijking bekeken met staande-golfsimulaties. Het is handig om bij het evalueren van verschillende discretizaties naar simulaties met staande golven te kijken, omdat alle fysica van belang aanwezig is, maar mogelijke verstoringen door randvoorwaarden worden uitgesloten. Het effect van de Lax-Wendroffdiscretizatie viel nogal tegen toen de resultaten met die van eerste-orde upwind werden vergeleken.

Het werd verondersteld dat ook het verplaatsingsalgoritme voor het vrij oppervlak een bron voor dissipatie van golfenergie was, omdat VOF met een stukgewijs-constante reconstructie van het vrij oppervlak (SLIC) een eerste-orde upwind discretizatie van de vloeistofflux bevat. De discretizatie van de vloeistofflux kan worden verbeterd door naar een stukgewijs-lineaire reconstructie van het vrij oppervlak (PLIC) te gaan. In simulaties met staande golven zagen wij echter dat met PLIC de dissipatie van golfenergie niet heel veel minder was dan met SLIC.

Een aanzienlijke reductie van energiedissipatie werd pas verkregen toen PLIC voor het vrij oppervlak werd gecombineerd met de Lax-Wendroffdiscretizatie van de convectieve term van de impulsvergelijking. Dat bleek het duidelijkst in simulaties voor lopende golven; de combinatie gaf daar 2% golfenergiedissipatie over twee golfengtes ten opzichte van 18% dissipatie met de oorspronkelijke combinatie van SLIC en eerste-orde upwind voor convectie.

Golfgeneratie

In COMFLOW worden golven doorgaans gegenereerd door snelheden als Dirichletrandvoorwaarde aan de rand van het domein op te leggen. Deze snelheden komen uit golftheorie. Bekende golftheorieën zijn Stokes 5^e-orde en stream function-theorie (Rienecker-Fenton); hiervoor zijn analytische oplossingen beschikbaar. In dit proefschrift zijn voornamelijk golven gegenereerd met Rienecker-Fentonoplossingen. We hebben onderzocht hoe goed COMFLOW de analytische oplossingen kon reproduceren. Daartoe werd zowel het vrij oppervlak, als het verticale profiel van de horizontale snelheid vergeleken in een roosterconvergentiestudie. Voor het fijnste rooster kwam in COMFLOW het vrij oppervlak tijdens golftoppen goed overeen met de analytische oplossing. In een golfdal was er voor hetzelfde rooster nog een aanzienlijk verschil. Dit is nog niet goed begrepen en onderdeel van vervolgonderzoek. Ook voor het snelheidsprofiel ten tijde van een golftop waren er verschillen. Niet in de buurt van het vrij oppervlak, waar we ze vanwege de grote gradiënten in de snelheid hadden verwacht, maar juist dichtbij de bodem. Ook dit moet verder onderzocht worden.

Steile, onregelmatige golven werden in COMFLOW gegenereerd op twee manieren: de eerste is met snelheden ontleend aan lineaire golftheorie (meerdere frequentiecomponenten); de tweede manier is door snelheden te gebruiken uit simulatieresultaten van een externe methode. De externe methode die hierbij gebruikt werd, een niet-lineaire potentiaalmethod, hebben we de naam Finite-Difference Finite Element Method (FDFEM) gegeven. Deze twee golfgeneratiemethoden zijn onderling als volgt vergeleken. Eerst werd een simulatie gedaan met FDFEM. De oppervlakteuitwijking op een zekere locatie werd als referentieoplossing beschouwd. De snelheden uit FDFEM op een locatie enige afstand voor de uitvoerlocatie werden opgelegd aan COMFLOW op dezelfde locatie. Zo kon de oppervlakteuitwijking op de uitvoerlocatie uit COMFLOW worden verkregen en vergeleken met de referentieoplossing. De oppervlakteuitwijking in COMFLOW kwam goed overeen met het vrij oppervlak in FDFEM.

Een vergelijkbare procedure werd gebruikt om de generatieprocedure met lineaire frequentiecomponenten te evalueren. Alleen werden nu op enige afstand van de uitvoerlocatie niet de snelheden verkregen, maar het vrij oppervlak. De tijdreeks voor het vrij oppervlak werd met een Fouriertransformatie omgezet naar het frequentiedomein. In het frequentiedomein werden van alle golfcomponenten snelheidscomponenten gemaakt, die met een inverse transformatie weer naar tijdreeksen werden omgezet. Met de tijdreeksen voor de snelheid werden golven gemaakt. Vervolgens werd op de uitvoerlocatie het vrij oppervlak in COMFLOW met de referentieoplossing uit FDFEM vergeleken. Bij deze methode bleven, ook na roosterverfijnen, verschillen

tussen COMFLOW en FDFEM bestaan. De conclusie hiervan is dat golven niet met snelheden uit lineaire theorie gegenereerd moeten worden als de COMFLOWoplossing later met metingen uit een experiment vergeleken moet worden.

Ongewenste golfreflectie verminderen bij domeinranden

Zonder maatregelen zijn de randen van rekendomeinen volledig reflecterend. Bij domeinranden worden daarom vaak dissipatiezones gebruikt om de golfenergie over een relatief korte afstand te reduceren, opdat de golven, zodra ze bij de rand aankomen en reflecteren, onvoldoende hoogte hebben om nog tot verstoringen nabij de constructie te kunnen leiden.

Dissipatiezones hebben meerdere golf lengtes nodig om effectief te kunnen zijn. In veel gevallen nemen de dissipatiezones zelfs meer ruimte in beslag dan het deel van het rekendomein dat nodig is om de golfinteractie met de constructie te simuleren. Dat kan efficiënter. Lokale absorberende randvoorwaarden zijn een alternatief voor dissipatiezones en hebben niet al die ruimte nodig. In dit proefschrift wordt een absorberende randvoorwaarde afgeleid voor langkammige, onregelmatige golven, die efficiënter is en effectiever dan een dissipatiezone van twee typische golf lengtes.

Voor de afleiding van de absorberende randvoorwaarde hebben we de dispersierelatie voor een bepaalde (beperkte) set golfgetallen nauwkeurig benaderd. Deze benadering is, samen met tweede-orde verticale afgeleiden van de oplossingvariabelen in het binnengebied, onderdeel geworden van de randvoorwaarde. De differentiaalvergelijking die zo verkregen wordt, is gediscrètiseerd en gecombineerd met de discrete impulsvergelijking. Het resultaat is een uitdrukking voor de druk op het nieuwe tijdsniveau die met de Poissonvergelijking gecombineerd is. Theoretisch kan de maximale waarde van de reflectiecoëfficiënt, dat is de verhouding van uitgaande golfamplitude en gereflecteerde golfamplitude, slechts 2% groot worden voor dimensieloze golfgetallen tussen 0 en 6. In echte simulaties wordt de maximale reflectiecoëfficiënt ongeveer 5%. Het verschil tussen de theoretische en de daadwerkelijk verkregen waarde van de reflectiecoëfficiënt komt hieruit voort: 1. in de afleiding van de randvoorwaarde is lineaire potentiaaltheorie gebruikt, terwijl de vergelijkingen in COMFLOW niet-lineair zijn; 2. de tweede-orde afgeleide in de verticaal kan niet tot voorbij het vrij oppervlak worden opgelost. Bij het vrij oppervlak moet deze benaderd worden. De benadering die we hier gebruiken hebben is nogal grof en daar moet in verder onderzoek aandacht aan besteed worden.

Validatie in 3D

Bij MARIN zijn experimenten gedaan met een geschematiseerd model van een semi-submersible in golven. Golven werden gegenereerd met een roterend golfschot aan een zijde van de tank. Aan de andere zijde was een parabolisch strand aanwezig waar golfbreken optreedt om ongewenste reflectie van golven te reduceren. Het model was ongeveer 1 meter lang en is in het midden van de tank geplaatst. Er waren druksensors op de kolommen en het dek van het model aangebracht en langs de kolommen en rondom het model waren golfhoogtemeters geplaatst. Tijdens de experimenten vond

heftige golfinteractie met het model plaats. Golfklappen troffen beide kolommen en verscheidene golfklappen bereikten het dek.

In COMFLOW werd de hele breedte van het tank gemodelleerd. De zijwanden van het rekendomein (in x-z-richting) waren volledig reflecterend, net als de zijwanden van de tank. De hele lengte van de tank paste niet in een rekendomein. De inkomende golfrand (in x-y-richting) werd daarom op ongeveer een typische golflengte voor de constructie geplaatst. Hier werden golven gemaakt door snelheden uit een FD-FEM-simulatie voor te schrijven. Aan de uitstroomzijde van het domein werd de absorberende randvoorwaarde uit dit proefschrift gebruikt om golfreflectie te reduceren.

Vanwege stabiliteitsproblemen is de FDFEM-simulatie op een redelijk grof rooster uitgevoerd met een waterdiepte die kleiner was dan in de tank. Om deze reden konden de golven in FDFEM hoogstens redelijk met die uit het experiment overeenkomen. En er was nog iets aan de hand. Achteraf bleek dat de positie van het model ten opzichte van het golfschot niet met voldoende nauwkeurigheid was geregistreerd. Daarom hebben we op verschillende locaties de oppervlakteuitwijking in FDFEM vergeleken met die uit een ongestoorde proef (zonder constructie) van het experiment. De locatie waar de twee het best overeenkwamen werd in COMFLOW als positie van het model gebruikt.

Als je bedenkt dat de golven in simulaties toch iets anders waren dan in het experiment – niet alleen vanwege modelfouten, maar ook omdat de waterdiepte in het model niet overeenkwam met de tank – dan pakt vergelijking tussen COMFLOW en het experiment best goed uit. Drukken en oppervlakteuitwijkingen uit COMFLOW komen goed overeen met de metingen.

De 3D validatie van COMFLOW was ook een belangrijke test voor de absorberende randvoorwaarde die hier werd afgeleid. Uit de simulaties blijkt dat de randvoorwaarde met goed gevolg kan worden ingezet voor praktische simulaties. Deze simulaties zouden niet met een dissipatiezone op een PC kunnen worden uitgevoerd, omdat de som met deze resolutie dan eenvoudigweg niet in het geheugen zou passen. Het zou interessant zijn geweest om voor deze simulatie de verschillen tussen dissipatiezone en absorberende randvoorwaarde te beschouwen. Aan de andere kant, kunnen we hieruit ook opmaken dat door de absorberende randvoorwaarde nu simulaties uitgevoerd kunnen worden die voorheen niet mogelijk waren.

Contents

Summary	v
Samenvatting	xi
1 Introduction	1
1.1 Offshore	1
1.2 Waves	2
1.3 Experiments	3
1.4 Numerical simulation	4
1.5 This research	5
1.6 Outline	6
2 Mathematical model	9
2.1 Governing equations	9
2.2 Boundary conditions	12
3 Numerical model	15
3.1 Domain and grid	15
3.2 Continuity equation	17
3.3 Momentum equation	17
3.3.1 Convection	19
3.3.2 Diffusion	20
3.3.3 Pressure and gravity	21
3.3.4 Time discretization	23
3.3.5 Stability	24
3.4 Free surface	25
3.5 Boundary conditions	27

4	Free surface waves	31
4.1	Definitions	31
4.2	Accuracy of wave simulations	32
4.3	Simplifications	34
4.4	Standing waves	35
4.4.1	Method of testing	35
4.4.2	Velocity extrapolation at the free surface	37
4.4.3	Free surface reconstruction	40
4.4.4	Convective term in the momentum equation	44
4.4.5	Flux limiters	46
4.5	Propagating waves	47
4.6	Discussion	50
5	Incoming and outgoing waves	53
5.1	Boundaries and boundary conditions	55
5.1.1	Dirichlet for the velocity	56
5.1.2	Dirichlet for the pressure	56
5.1.3	Neumann for the pressure	57
5.2	Wave generation	58
5.2.1	Regular waves	59
5.2.2	Irregular waves	63
5.2.3	Discussion	66
5.3	Preventing reflection	67
5.3.1	Dissipation zones	67
5.3.2	Matching to external solutions	69
5.3.3	Non-reflecting boundary conditions	70
5.4	Discussion	72
6	Generating absorbing boundary condition	75
6.1	Literature overview	75
6.1.1	Short-crested waves	76
6.1.2	Dispersive waves	78
6.1.3	Incoming and outgoing waves	79
6.2	Motivation	80
6.3	Derivation	82

6.4	Stability	86
6.5	Incoming and outgoing waves	90
6.6	Numerical implementation	91
6.6.1	Discrete equations	91
6.6.2	Bottom and free surface	94
6.7	Waves under an angle with the boundary	95
6.8	Results	97
7	Validation study	105
7.1	Introduction	105
7.2	Experiment	106
7.3	Simulation	108
7.3.1	Grid study	108
7.3.2	Sensitivity study	109
7.3.3	Irregular wave simulation	111
7.4	Discussion	115
8	Concluding remarks	119
	Bibliography	123
	A Potential theory for waves	127
	B Reflection coefficient	129
	Dankwoord	133
	Curriculum Vitae	136

Chapter 1

Introduction

The main topic of this research is the numerical simulation of extreme wave behaviour near offshore structures. Here, we expound on the position of numerical simulation in the discipline of Offshore Engineering and formulate an introductory account of what is to come in the remainder of this thesis.

1.1 Offshore

The ocean is without end. Explorer ships sail the ocean continuously, while they scan the ocean floor – mapping it, performing seismic tests, interpreting test results – ever in search of unproven offshore deposits of oil and gas. During exploration, prospectors are sometimes caught in heavy storms, which induce large vessel motions and even water on deck, but are hardly ever fierce enough to endanger resuming operation when the peak of the storm has past. And, oftentimes, weather forecasting will have foretold when and where the worst of the storm will strike, sufficiently far in advance for the ship to go around.

Weather forecasting may benefit ships, more permanent installations at sea are not as mobile and will suffer the worst of a storm when it hits. Once an offshore field is in production, the platform where the post-processing of oil and gas takes place, will be connected to the sea bed in more ways than one. This is obvious for bottom founded structures, which have dominated the offshore industry during the first decades of its existence, in the shallower waters nearshore. But also floating production platforms, that have become widespread in recent years, in deeper water, still require mooring or dynamic positioning to keep them in position. And they are connected to the well heads at the sea bed by multiple arrays of risers, transporting oil from the bed to the sea surface (see Fig. 1.1).

Systems with disconnectable turrets exist (complex structures with risers and mooring lines, around which the floater can turn to keep its bow in head waves), but in most cases offshore platforms are designed to remain in place and safely endure environmental loading during the economic life time of the structure. It is the responsibility

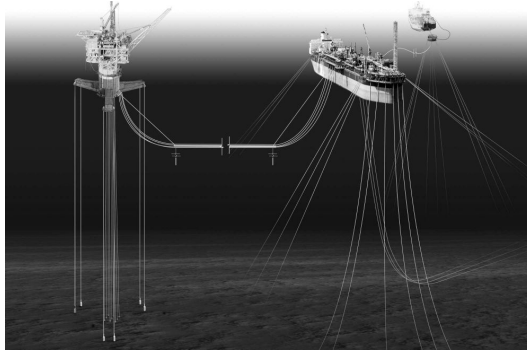


Figure 1.1: *Conceptual design by Atlantia Offshore Ltd. Tension-leg platform with well heads and risers connected to the sea bed. The TLP connects to an FPSO some distance away.*

of the design team to determine the maximum loading, that has a certain probability of occurring within this time, and to design the structure to survive these loads.

1.2 Waves

Structures at sea are subject to a variety of environmental loads; during normal operation, but especially in survival conditions. Currents are always present, exerting a constant but hardly ever critical force on the mooring system of the structure. Mild winds and waves yield slight variations in force on top of the constant drag component imposed by the current. But it is only during heavy storms that forces resulting from wind and waves become significant.

Strong winds can inflict damage to the structure above the free surface, although the damage is mostly restricted to non-critical components such as radar towers and other extruding elements. In spite of the inconvenience, the effect of heavy wind is of minor importance compared to the damage inflicted by an impacting wave. Wind may reach velocities of up to three hundred kilometers per hour, but the density difference between water and air of a factor one thousand makes the consequences of water impact all the more dramatic.

Design engineers will try to prevent deck impact at all time. A safe minimum distance is kept between the highest possible wave the structure can encounter, and the deck. The distance between free surface and deck is called air gap and determining a safe air gap is a balancing act between economics and probability. The question becomes: how to determine the maximum wave height that has a certain, low probability of occurring during the life time of the structure? Satellite measurements have made statistics of the wave climate available for locations all around the world. But the wave height near a structure does not depend on the undisturbed wave alone.

A large structure locally changes the undisturbed free surface elevation. Linear potential theory for waves acknowledges three contributions to the free surface elevation in the surroundings of a structure in water: (1) undisturbed incoming waves as if the structure were not there, (2) diffracted waves due to the presence of the structure and (3) radiated waves resulting from the motion of the structure. For complex structure geometries, the latter two contributions to the free surface elevation near the structure can only be determined by experiments on model scale or numerical simulation.

1.3 Experiments

Experiments on model scale are carried out during later stages of the design process. The basic outline of the structure based on design rules and some preliminary calculations will then have been completed. Experiments are used to test the performance of the structure in terms of, for instance, motions for floaters, or run-up and consecutive deck impact for bottom founded structures, as if the structure was out at sea. To that end, relevant sea states are created in an experimental wave basin with the structure, on scale, in position in the basin. During the experiment the motion of the structure is monitored and measurements of surface elevation and (impact) pressure are taken.

To generate waves, wave boards are installed along one or more sides of the experimental wave basin. A single wave board along the entire side makes long crested waves, segmented wave boards are used to generate short crested waves. In modern wave basins, such as the Offshore Basin at the Maritime Research Institute Netherlands (MARIN), wave generation is just one of the features available: an experiment can include waves, current and wind at the same time.

Unfortunately, the information that can be obtained from an experiment is limited. Constructing a model of the structure is expensive and constructing multiple models or making minor adjustments to the model during the experiments is not always possible. The number of sea states that can be tested is restricted by the time made available in the planning of the basin operator. And during a commercial experiment, only local measurements of the surface elevation and flow velocities can be taken and never measurements in the entire basin. It may not be relevant to know the position of the free surface in the whole basin, but when flow velocity measurements are concerned, the global flow pattern around the underwater part of the structure can lead to an important understanding of and may indicate ways to improvement of its (motion) behaviour.

Experiments are almost always performed on model scale. Scaling laws are available, as well as recommendations from systematic series of experiments, to convert measurement data on model scale to full scale results. The extrapolation towards full scale is often uncertain for several reasons. Important physical effects may not be included in the conversion, or systematic series may not be available for the structure geometry under consideration. An indication of the scale effects for arbitrary structure geometries would be of great value.

For reasons of model scale, flexibility, limited time in the basin and measurements of

a global nature, numerical simulation of a structure in waves can contribute greatly to the results available from an experiment.

1.4 Numerical simulation

Numerical simulation of structures in waves can at present only contribute to, but not replace physical experiments. It can probably never completely replace experiments. There are simply too many parameters a numerical solution depends on, to ever claim with certainty that the obtained result is as it would be in reality. Among these parameters are the type of modeling, the numerical approximation of the model equations, the grid, the algorithm and the implementation. And this list is far from complete.

For mild, operational wave conditions, linear 3D Boundary Element Methods (BEM) in the frequency domain have become the offshore industry standard to determine the motions of a floating structure. Linear BEM methods are an implementation of the linearized model equations for conservation of mass and momentum (rotation-free), with linearized boundary conditions at the free surface and near the structure. Only the underwater part of the structure is modeled and quadrilateral elements are used to describe the underwater geometry. For each element, or panel, an equation can be formulated and the system of equations can be rewritten to a matrix equation, where the left-hand side matrix is completely filled. The matrix is generally small and can be solved with a direct method in a small amount of time. One matrix equation is solved per wave frequency and per wave direction, but still, the total computation time for all frequencies and directions is generally short.

Linearized theory is used far beyond the range of its formal validity with good results for the vessel's motions, but the results in terms of fluid kinematics become poor for truly steep waves. Higher order BEM methods exist, to second order in the frequency domain [45], to higher order mostly in the time domain [43]. In higher order methods the free surface is gridded by panels as well, which significantly adds to the number of panels required for a simulation. But as the number of panels increases and the order of the method increases, it becomes increasingly difficult and time consuming to set up the (full) matrix equation and to solve it.

In many types of steep wave simulation, it is more efficient to approximate the model equations by means of a field method [6]. When overturning waves are present in the simulation, the bookkeeping concerned with the position and the numbering of the boundary elements becomes prohibitively difficult; then the use of a field method comes highly recommended. In a field method the entire domain – and not only the boundary – is fitted with grid cells and one equation is solved for each cell (see Fig. 1.2). Compared to boundary element methods, the system of equations is larger, but sparse and very efficient sparse matrix solvers (“Poisson solvers”) are available that are generally faster for a comparable problem. Grids can be boundary fitted and adapting to moving geometries in time [49], or they are fixed and the geometry intersects with the grid, the intersection being different as the structure moves through the grid and as a function of time [14]. An advantage of conforming grids is that the

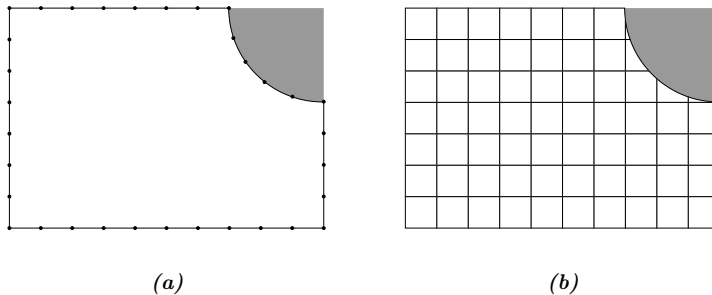


Figure 1.2: A boundary element grid in (a) vs. a field method grid in (b).

boundary and the location where boundary conditions need to be imposed, is clearly defined, whereas for intersected grids this is less so. A disadvantage of conforming grids is that the domain needs to be regrided when the position of the geometry changes.

For this research, the free surface treatment is what truly sets numerical methods apart. A grid can adapt to the free surface in the same way it can adapt to a moving geometry. But when the free surface is overturning as a result of wave breaking or due to run-up against a structure, adaptive grids are no longer possible. For extreme free surface events only three methods are suitable. In the level-set method the free surface is not a sharp interface, but rather diffuse: several layers of cells are used to capture the position of the free surface. The Volume-of-Fluid (VOF) method does retain a sharp interface. Here, fluid fragments are transported from one cell to another. After fluid convection has taken place, the free surface can be reconstructed from the new filling rates of the cells. In contrast to everything mentioned above, the Smooth-Particle-Hydrodynamics (SPH) method is a meshless method where fluid particles of finite size directly exchange momentum with others inside a region of influence surrounding each particle [37].

1.5 This research

The research contained in this thesis adds to a numerical method, that can simulate extreme wave impact hydrodynamics against structures. The method is based on the Navier-Stokes equations for conservation of mass and momentum. The discrete equations have been obtained by means of the finite volume method on a fixed, Cartesian grid. The method has adopted the ‘cut-cell method’ to describe the structure geometry; as a result, cells in this method can contain both part of the structure and be partially filled with fluid. The free surface is convected with an improved VOF method, where a local height function is used to overcome issues with mass conservation and disconnecting droplets, that troubled the original VOF method developed

by Hirt and Nichols [27].

Previous work on the numerical method contained in the COMFLOW program revolved around applications as diverse as liquid sloshing in satellites in zero-gravity circumstances [16], moving structures in water [14], blood flow through pulsating arteries [35] and wave impact loading on offshore structures [32]. The research with offshore applications was continued and organised as joint industry project, headed by MARIN, which attracted support from over twenty participating companies, well known in the offshore industry. The objective and aim of the project was:

“To develop a dedicated and well validated numerical tool for the offshore industry to study complex free surface problems, which is flexible in its application and has a coupling possibility to the other tools of participants.”

External funding from the Dutch technology foundation STW was used to employ two PhD students, working on different, new aspects of the numerical method. One has been based at the University of Groningen and has successfully finished his work on implementing two-phase (water and air) flow for extreme free surface events in offshore environments [54]. The other has been stationed at Delft University of Technology and his work is reported in the present document.

The objective of the work in this thesis is to find or devise methods to generate waves in numerical domains and to prevent reflection from its boundaries. Methods for wave generation and reflection prevention have been incorporated in the numerical method and the COMFLOW program. The topic of generating and absorbing waves by means of well designed boundary conditions is of crucial importance to the simulation of waves inside a domain. Adequate boundary conditions improve the quality of wave simulations and can save computation time and memory. See Chapter 5 and 6 for a discussion about boundary procedures.

A side aim in this research has been to assess the performance of the free surface displacement algorithm with regard to the propagation of waves. The numerical method discussed in this thesis is known to dissipate wave energy over time and propagated distance. The dissipation is quantified and it is shown in Chapter 4 that an improved reconstruction of the free surface, along with an improved convection scheme, can reduce wave energy dissipation.

1.6 Outline

Before the actual results of the research in this thesis are discussed, first the analytical equations that describe fluid flow are introduced in Chapter 2. The equations are concerned with conservation of mass, conservation of momentum and the evolution of the free surface over time.

Chapter 3 contains the discrete representation of the analytical equations mentioned above and it gives an account of how the equations are solved in our numerical method.

With Chapter 4 we arrive at a detailed discussion about the free surface displacement method, about how it performs in wave simulations and about how to improve and mitigate undesired side effects, such as artificial diffusion of wave energy.

The focus of this research is on generating waves and preventing reflection. Classic boundary conditions for simulating waves in numerical domains are the subject of Chapter 5: it provides an overview of the available literature on this subject and it reports on the performance in terms of reflection of several methods that have been considered.

The generating absorbing boundary condition in Chapter 6 has been newly devised for implementation in COMFLOW. It was found that absorbing boundary conditions in the literature were either of insufficient quality or close to impossible to combine with our numerical method. The generating absorbing boundary condition for long-crested dispersive waves in this thesis is both accurate for sea states often found in offshore environments, and practical to implement. Results of performance tests are included.

Simulation results, validated by experiments, have been included in Chapter 7. The simulations include a semi-submersible platform in relatively deep water and a gravity base structure in relatively shallow water. In the experiment measurements were taken of free surface elevations and pressures at key positions around the structure; the measurements are compared to simulation results at the same location.

And, finally, to conclude the discussion, observations regarding the method and the results obtained from application of the method to offshore structures in waves, have been collected in Chapter 8 along with several statements with recommendations for future research.

Chapter 2

Mathematical model

The transition between observation and numerical results is mediated by mathematical models. A quite general model that describes fluid flow has been attributed the name Navier-Stokes equations. It is a set of equations that describe the conservation of mass and momentum, the latter being derived from Newton's second law applied to a fluid.

Both water and air are considered fluids and the same equations apply to either fluid. At sea we mostly observe the interface between water and air. It is when structures at sea, such as ships or platforms, protrude through the interface, that effects occur we wish to quantify.

In the application area of offshore engineering the effects are dominated by water, since water as a result of the density difference carries more momentum. In other areas, such as naval architecture applied to sailing yachts, the flow of air is of equal importance for the functioning of the ship as a whole.

The sea and structures at sea exchange momentum. Offshore structures generally move only at very low velocities and are on average located at one position. But when a structure is caught in a heavy storm, the sea can cause large motions and inflict serious damage. In order to compute the forces leading to potential damage, we try to solve the equations that describe fluid flow. The equations are given in this chapter.

2.1 Governing equations

The Navier-Stokes equations are a simplified representation of reality. It is not possible and unnecessary to go down to the molecular level to model fluid flow on the scale that we are interested in. The fluid is thought to be a homogeneous medium with equal properties in all directions and continuum mechanics is used to describe its behaviour.

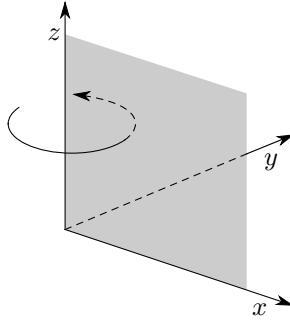


Figure 2.1: Right-handed Cartesian axis system showing the three main directions. The xz -plane is highlighted and the direction of positive rotation is given.

First the axis system is defined. In this thesis a right-handed Cartesian coordinate system is adopted as depicted in Fig. 2.1. The coordinate axes are indicated by $\mathbf{x} = (x, y, z)^T$.

The equations in this thesis are mostly formulated and discussed in 2D in the xz -plane (highlighted in Fig. 2.1). They can easily be generalized to 3D. Where this is not apparent or requires additional attention, it will be made explicit.

Now, a control volume Ω is introduced in Fig. 2.2. The change of mass inside the control volume is equal to the flow of mass over the boundary Γ of the control volume:

$$\int_{\Omega} \frac{\partial \rho}{\partial t} d\Omega + \oint_{\Gamma} (\rho \mathbf{u}) \cdot \mathbf{n} d\Gamma = 0. \quad (2.1)$$

In (2.1), ρ is the density of the fluid. The density is a scalar. The velocity is a vector and represented by $\mathbf{u} = (u, v, w)^T$, in which u , v and w are the velocities in the three coordinate directions. The vector normal to the volume boundary is denoted by \mathbf{n} . Eq. (2.1) is known by the name *continuity equation*.

A similar control volume can be used to derive the equation for the conservation of momentum. The change of momentum inside the volume depends on the transport of momentum over the volume boundary, an external force \mathbf{f} acting on the entire volume and a contribution from the normal and tangential stresses:

$$\int_{\Omega} \frac{\partial(\rho \mathbf{u})}{\partial t} d\Omega + \oint_{\Gamma} \rho \mathbf{u} (\mathbf{u} \cdot \mathbf{n}) d\Gamma + \oint_{\Gamma} p \mathbf{n} d\Gamma - \oint_{\Gamma} \left(\mu (\nabla \mathbf{u} + \nabla \mathbf{u}^T) - 2/3 \mu \nabla \cdot \mathbf{u} \right) \cdot \mathbf{n} d\Gamma - \int_{\Omega} \rho \mathbf{f} d\Omega = 0. \quad (2.2)$$

Here, the pressure is represented by p and μ is the dynamic viscosity. The viscosity depends on temperature and in less extent on the ambient pressure. Temperature

variation is not included in this research. Therefore, in the remainder of this thesis the viscosity can be assumed constant.

The external force, in absence of further external loading, is equal to gravity:

$$\mathbf{F} = \begin{pmatrix} 0 \\ 0 \\ -g \end{pmatrix}. \quad (2.3)$$

In our applications water can be considered incompressible. For incompressible fluids $\partial\rho/\partial t = 0$ and as a result, using Gauss' divergence theorem:

$$\oint_{\Gamma} \mathbf{u} \cdot \mathbf{n} \, d\Gamma = \int_{\Omega} \nabla \cdot \mathbf{u} \, d\Omega = 0. \quad (2.4)$$

After substitution of (2.4) into Eq. (2.2), the momentum equation for an incompressible, newtonian fluid is obtained:

$$\int_{\Omega} \frac{\partial \mathbf{u}}{\partial t} \, d\Omega + \oint_{\Gamma} \mathbf{u} (\mathbf{u} \cdot \mathbf{n}) \, d\Gamma + \frac{1}{\rho} \oint_{\Gamma} p \mathbf{n} \, d\Gamma - \nu \oint_{\Gamma} \nabla \mathbf{u} \cdot \mathbf{n} \, d\Gamma - \int_{\Omega} \mathbf{f} \, d\Omega = 0, \quad (2.5)$$

in which ν is the kinematic viscosity, $\nu = \mu/\rho$.

The equations above cannot be solved analytically. They have to be approximated to obtain results. One approach is to set up a system of discrete equations and solve the system numerically with a computer. In this thesis, in the next chapter, a numerical method is described to do just that. Computers, however, have only recently become powerful enough to perform practical simulations.

In the past, meaningful results have been obtained by means of another approach: simplification of the equations themselves. The concept of *irrotationality*, where $\nabla \times \mathbf{u} = 0$, allows for the introduction of a potential function Φ , whose derivatives yield the velocity in the direction of the derivative.

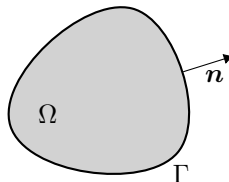


Figure 2.2: Control volume, in which the equations governing fluid flow are formulated. The volume is indicated by Ω , whereas the boundary of the control volume is denoted by Γ . The vector \mathbf{n} shows the direction normal to the boundary.

The following holds for the potential:

$$\nabla\Phi = \begin{pmatrix} u \\ v \\ w \end{pmatrix}. \quad (2.6)$$

Many flow types may be considered as irrotational and the use of the potential leads to a reduced set of equations that can be solved analytically for these flow types. With the potential the continuity equation becomes:

$$\nabla^2\Phi = 0, \quad (2.7)$$

which is the well known Laplace equation.

And after integration, the momentum equation becomes the Bernoulli equation, which may be applied along a streamline:

$$\frac{\partial\Phi}{\partial t} + \frac{1}{2}|\nabla\Phi|^2 + \frac{p}{\rho} - \mathbf{F} = C, \quad (2.8)$$

in which \mathbf{F} is the integrated force vector and C is an integration constant.

Eqs. (2.7) and (2.8) have been used to derive analytic solutions for regular propagating waves. This is shown in Appendix A about potential wave theory. Potential wave theory is used in Chapter 5 to generate waves in numerical simulations.

Free surface

The continuous equations for conservation of mass and momentum are valid in one fluid. In offshore applications, however, many of the phenomena that need to be considered during the life time of a structure at sea, occur in the interface between water and air. The interface between water and air is called free surface.

The actual position of the free surface, $S(\mathbf{x}, t)$, in time and space can be resolved from the conservation of one of these fluids, in this case water:

$$\frac{DS}{Dt} = \frac{\partial S}{\partial t} + \mathbf{u} \cdot \nabla S = 0. \quad (2.9)$$

If water is considered incompressible, then $\nabla \cdot \mathbf{u} = 0$ and (2.9) can be rewritten to:

$$\frac{DS}{Dt} = \frac{\partial S}{\partial t} + \nabla \cdot (\mathbf{u}S) = 0. \quad (2.10)$$

2.2 Boundary conditions

To obtain a solution to the system of partial differential equations describing fluid flow, boundary conditions need to be imposed. In closed volumes, natural boundary conditions can be imposed at the boundary:

$$\mathbf{u} = 0. \quad (2.11)$$

Eq. 2.11 describes that there is zero flow through the boundary (in normal direction). When there is flow through the boundary, other boundary conditions are required. In chapters 5 and 6 equations are derived for waves propagating through the boundary; in section 5.1 boundary conditions for other types of flow are discussed.

The flow along the boundary, in tangential direction, is also zero. This is often referred to as the no-slip condition. When the free-slip condition is imposed, the derivative in normal direction to the boundary of the velocity along the boundary is zero:

$$\frac{\partial u_t}{\partial n} = 0, \quad (2.12)$$

where n denotes the normal direction and the subscript t indicates the tangential direction.

When the equations for fluid flow are resolved in both water and air, the balance of forces at the free surface follows from the equations themselves. In case the equations are solved only in water, the free surface is a formal boundary and boundary conditions need to be imposed. The boundary conditions at the free surface follow from the equilibrium of forces in normal direction:

$$-p + 2\mu \frac{\partial u_n}{\partial n} = -p_0 + \sigma \kappa, \quad (2.13)$$

and in tangential direction:

$$\mu \left(\frac{\partial u_n}{\partial t} + \frac{\partial u_t}{\partial n} \right) = 0. \quad (2.14)$$

Here, again, the indices n and t denote the normal direction and the tangential direction. The surface tension is represented by σ and the curvature of the free surface by κ . Eqs. (2.13) and (2.14) are formulated under the assumption that the fluid is incompressible and that the pressure in air is constant and equal to p_0 .

On the scale of offshore structures, the stress resulting from the surface tension is negligible and in offshore applications the parameter σ is often set to zero.

Chapter 3

Numerical model

In COMFLOW the governing equations for fluid flow are evaluated on finite size control volumes to formulate a discrete representation of the continuity and the momentum equation. Control volumes are defined with respect to grid cells and the combination of cells is called the domain. In this chapter, the discrete system of equations is derived. It also shows the method to convect the free surface.

3.1 Domain and grid

In our method we have adopted a Cartesian grid, where the grid lines are kept aligned with the coordinate axes. The grid is structured, but not necessarily uniform; it allows for a modest amount of stretching.

A structured Cartesian grid has a number of clear advantages in contrast to an unstructured grid. The discretization is more straightforward and the step towards higher order discretization can more easily be made. Then again, there are also disadvantages to a structured grid: when a small grid distance is desired for accuracy at one location where large gradients are expected, then the grid distance remains small throughout the domain. In general, a structured grid requires more grid cells than an unstructured grid.

Impermeable structures within the domain are represented by a cut-cell method [51], where the structure intersects with the grid. The intersection results in cells that can be filled with both fluid and (part of the) structure at the same time. The cut-cell method is more accurate than a staircase representation of a structure and allows for the same flexibility that is inherent to a boundary-fitted unstructured grid.

Fig. 3.1 shows a grid cell, in which part of the cell is filled by a section of structure and the other part filled by water. The normalized volume aperture that can be filled by water is denoted by F^b . The part of the cell that is taken up by structure, then, is $(1 - F^b)$. Where the structure cuts through a cell face, the normalized surface aperture A^n – where n can denote any of x , y and z – is a measure of the face

segment that is open to flow. Fig. 3.3 shows the position of the solution variables

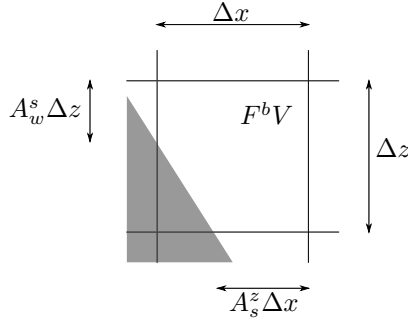


Figure 3.1: Grid cell, which is cut by a section of structure with the positions of the velocities in the cell faces. The volume aperture F^b accounts for the amount of fluid the cell can contain. The face apertures A^n define which part of the cell face is open to flow. In this figure the total volume of the cell is $V = \Delta x \Delta z$.

within a cell. Velocities are positioned in the cell faces and the pressure inside a cell is located in the middle. A grid with staggered solution variables allows for a compact stencil and avoids the use of special measures to prevent point-to-point oscillations that can be observed in collocated grids, where the solution variables within a cell are all positioned at the same location.

Cells can also be partially filled with fluid. In other words, the free surface intersects with the grid in much the same way a structure does. The volume F^s keeps track of the amount of fluid occupying the cell. F^s can never be larger than the volume aperture F^b .

In the domain a labelling system identifies similar cells that call for similar processing. In this discussion the same labels are used. There is a distinct order in which cells are labelled. Firstly, **Empty** cells are identified; they do not contain fluid, but can become filled at later time. Consecutively, **Surface** cells are labelled; they are partially filled with fluid and border to E-cells. S-cells are thought to contain the free surface. Finally, **Fluid**-cells can be selected and they border to S-cells and other F-cells. Away from the free surface F-cells are mostly completely filled with fluid.

Boundary cells can border to any of the cells mentioned before. The cells indicated by B are filled entirely by the structure that intersects with the grid. In these cells, F^b is zero and they cannot contain any fluid. A visual representation of cells in the gridded domain is given in Fig. 3.2.

E	E	F	E	S	E	E	E	E
E	E	S	S	F	S	E	E	E
S	S	F	F	F	F	S	S	S
F	F	F	F	F	F	B	F	F
F	F	F	F	F	B	B	B	F

Figure 3.2: The labeling system identifies Fluid cells, Surface cells, Empty cells and Body cells

3.2 Continuity equation

The control volume for the continuity equation coincides with a grid cell. Part of the control volume can be occupied by a section of structure, as shown in Fig. 3.3. Here, the velocities are shifted towards the center of the face section that is open to flow. Since the velocity is assumed constant along one cell face, the actual position of the velocity on a face is irrelevant.

The continuity equation is given in (2.1). For incompressible flow it is restated here:

$$\oint_{\Gamma} \mathbf{u} \cdot \mathbf{n} d\Gamma = 0.$$

The equation can be approximated by accounting for the mass fluxes over the faces of the control volume. The mass flux over the eastern cell face is $\mathcal{F}_e = u_e A_e^x \Delta z$. The same goes for the northern, western and southern face. The discrete continuity equation then becomes:

$$(u_e A_e^x - u_w A_w^x) \Delta x + (w_n A_n^z - w_s A_s^z) \Delta z = 0. \quad (3.1)$$

3.3 Momentum equation

The momentum equation for incompressible flow consists of: 1. a time derivative, 2. a convective part, 3. a diffusive part, 4. a pressure contribution and 5. an external force working on the entire volume. The composing parts are indicated in the following

equation:

$$\underbrace{\int_{\Omega} \frac{\partial \mathbf{u}}{\partial t} d\Omega}_{1.} + \underbrace{\oint_{\Gamma} \mathbf{u} (\mathbf{u} \cdot \mathbf{n}) d\Gamma}_{2.} + \underbrace{\nu \oint_{\Gamma} \nabla \mathbf{u} \cdot \mathbf{n} d\Gamma}_{3.} - \underbrace{\frac{1}{\rho} \oint_{\Gamma} p \mathbf{n} d\Gamma}_{4.} + \underbrace{\int_{\Omega} \mathbf{F} d\Omega}_{5.} = 0.$$

The time discretization is separated from the space discretization. The control volume for the momentum equation is shown in Fig. 3.4. The control volume has been shifted in space with respect to the control volume of the continuity equation. The space discretization of the time derivative in x -direction is obtained by applying the midpoint rule:

$$\int_{\Omega} \frac{\partial u}{\partial t} d\Omega = \frac{\partial u_c}{\partial t} \frac{F_w^b \Delta x_w + F_e^b \Delta x_e}{2} \Delta z, \quad (3.2)$$

in which the size of the control volume has been computed as the average of volume apertures on either side of the control volume.

The time derivative has not been approximated yet; its discrete counterpart will be introduced later in this chapter, when the space discretization of the remaining terms in the momentum equation has been discussed.

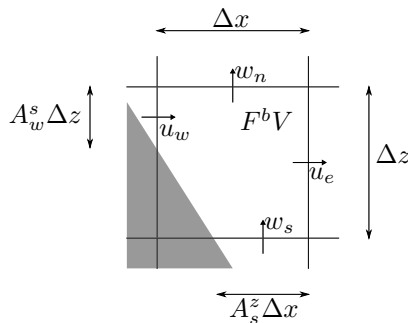


Figure 3.3: Control volume for the continuity equation. The control volume coincides with a grid cell. The velocities to determine the fluxes over the faces of the control volume are positioned in the middle of the part of the cell face that is open to flow.

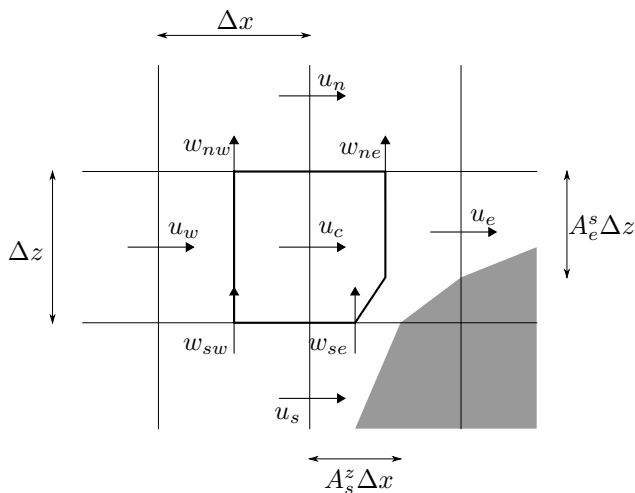


Figure 3.4: Control volume for the momentum equation in the presence of a cut cell. The velocities and distances to approximate the convective term of the momentum equation are shown at their respective positions in the grid. The velocities required for the fluxes over the faces of the control volume are obtained by interpolation.

3.3.1 Convection

The convective term of the momentum equation in x -direction is as follows:

$$\int_{\Gamma} u (\mathbf{u} \cdot \mathbf{n}) d\Gamma.$$

To approximate this equation, again, fluxes over the faces of the control volume have to be determined. In these fluxes the distinction has to be made between the *convected* quantity, u , and the *convecting* mass flux, $(\mathbf{u} \cdot \mathbf{n}) d\Gamma$, with which u is convected. These terms are treated differently.

The convecting mass flux has to be determined at the face of the control volume, depicted in Fig. 3.4. The face of the control volume is always midway in between cell faces or between a cell face and a geometry boundary. The mass flux, therefore, is determined as the average of the velocities on either side of the control volume face. For the convecting mass flux at the eastern face this yields:

$$\mathcal{F}_e^m = \frac{1}{2} (u_c A_c^x + u_e A_e^x) \Delta z \quad (3.3)$$

Note that the averaging is independent of grid size and remains the same on non-uniform grids. It does depend on whether a cell has been cut by the structure.

As mentioned, the convected quantities, in this case the velocity u , are treated differently. The velocity u has to be determined at the eastern control volume face as well, but a factor α is introduced in the interpolation between velocities on either side of the volume face:

$$u = \alpha u_c + (1 - \alpha) u_e.$$

The factor α is used to specify an upwind bias in the interpolation. When the mass flux over the volume face is positive, setting α to 1 yields a full upwind discretization and setting α to 0.5 yields a central discretization. It is known from analysis of the convection/diffusion equation that central discretization is second order accurate, but gives spatial instabilities, so called ‘wiggles’, on coarse grids.

Upwind discretization is first order accurate and is free of wiggles on any mesh size. Compared to central discretization, upwind discretization of the convective term in the momentum equation gives additional, ‘artificial’ viscosity of the order of the mesh size. On coarse grids the additional viscosity is much larger than the physical viscosity ν ; it keeps solutions free of wiggles.

Combining the mass flux with the convected quantity u and rearranging terms, gives the convective flux over the eastern control volume face:

$$\mathcal{F}_e^c = \frac{1}{2} \mathcal{F}_e^m (u_c + u_e) + \frac{1}{2} \alpha |\mathcal{F}_e^m| (u_c - u_e). \quad (3.4)$$

Note that in case α equals 1, an upwind discretization is obtained with Eq. (3.4), regardless of the direction of mass transport. For completeness, the convective flux through the northern face is also given below; other fluxes can be determined in a similar manner:

$$\mathcal{F}_n^c = \frac{1}{2} \mathcal{F}_n^m (u_c + u_n) + \frac{1}{2} \alpha |\mathcal{F}_n^m| (u_c - u_n), \quad (3.5)$$

in which the mass flux is found to be $\mathcal{F}_n^m = \frac{1}{2} (w_c A_c^z + w_e A_n^z) \cdot \frac{1}{2} (\Delta x_w + \Delta x_e)$.

3.3.2 Diffusion

The diffusive term of the momentum equation in x -direction is stated here:

$$\nu \oint_{\Gamma} \nabla u \cdot \mathbf{n} d\Gamma.$$

The proper way to approximate the relation above on a non-uniform grid with cut cells has been presented by Dröge in [11]. His application was the Direct Numerical Simulation (DNS) of flow around a cylinder. In that type of application it is imperative that the formation of the boundary layer is represented correctly and that the flow separation point is predicted accurately.

Extreme wave impact loads on structures are mostly convection driven and the scale of offshore structures is such that, in general, coarse grids are used in engineering.

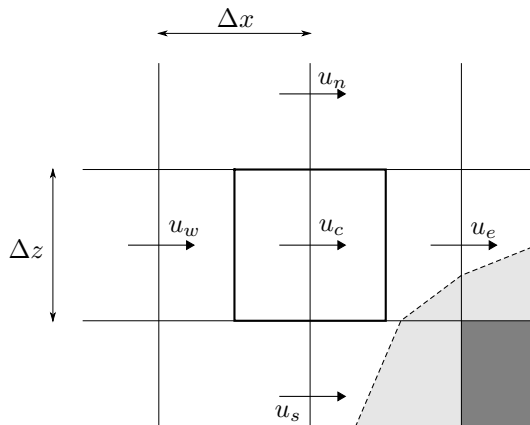


Figure 3.5: For the diffusive term in the momentum equation, the control volume is defined as if the structure has a staircase geomery. The fluxes are based on the uncut cell size.

Upwind discretization of the convective term in the momentum equation is the only suitable choice on coarse grids. And in case of upwind discretization on coarse grids, the total diffusion is dominated by the artificial viscosity.

Then it becomes a question of conscience: why overcomplicate matters and model the diffusive term at all? It is true that for coarse grids diffusion is dominated by artificial viscosity. But artificial viscosity depends on the grid size. For finer grids the artificial viscosity becomes smaller until for truly fine grids it is of the same order as the physical viscosity. For this situation we still want a discretization of the diffusive term that becomes more accurate for smaller mesh sizes.

The discretization adopted here does not account for cut cells; it is derived as if the structure is represented by means of a staircase approximation. The diffusive flux over the eastern control volume face in Fig. 3.5 then becomes:

$$\mathcal{F}_e^d = \int_{\Delta} z \frac{\partial u}{\partial x} dz = \frac{\Delta z}{\Delta x_e} (u_e - u_c). \quad (3.6)$$

And, again, to be complete, the flux over the northern volume face is given by:

$$\mathcal{F}_e^d = \int_{\Delta} x \frac{\partial u}{\partial z} dx = \frac{\Delta x}{\Delta z_n} (u_n - u_c). \quad (3.7)$$

3.3.3 Pressure and gravity

The pressure term in vertical z -direction is as follows:

$$\oint_{\Gamma} p n_z d\Gamma.$$

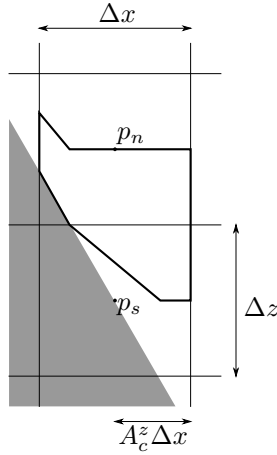


Figure 3.6: When the pressures along all the faces of the control volume have been integrated, the approximation of the pressure term in the momentum equation is found to only depend on the pressure difference and the central cell face aperture.

The pressure has to be evaluated along the faces of the control volume in Fig. 3.6. The pressure is assumed constant within a cell and with this in mind the pressure ‘fluxes’ can be determined. Note that these fluxes are actually forces that follow from pressure integration over a volume face.

The force in vertical direction only depends on the horizontal distance over which the pressure is evaluated, irrespective of the orientation of the control volume face. When all faces have been accounted for, the pressure term becomes:

$$\oint_{\Gamma} p n_z d\Gamma = p_n \Delta x - p_n (1 - A_c^z) \Delta x - p_s A_c^z \Delta x, \quad (3.8)$$

which can be simplified to:

$$\oint_{\Gamma} p n_z d\Gamma = (p_n - p_s) A_c^z \Delta x. \quad (3.9)$$

In most simulations in this thesis, gravity is the only external force. The proper discretization of the gravity term given below, should follow a similar path as the discretization of the pressure, since in hydrostatic situations the change in pressure can only be attributed to gravity, $\nabla p = -g$.

The external force in vertical z -direction is equal to gravity:

$$\int_{\Omega} -g d\Omega.$$

Using Gauss' theorem the volume integral can be rewritten to a surface integral along the boundary of the control volume in Fig. 3.6:

$$\int_{\Omega} -g d\Omega = \int_{\Omega} \nabla(-gz) d\Omega = \oint_{\Gamma} -gzn d\Gamma.$$

The gravity 'fluxes' over the vertical volume faces in horizontal direction are evaluated at the same elevation. They are of equal size but opposite in direction. In vertical direction the fluxes over the horizontal volume faces are evaluated at different elevations. The integral then becomes:

$$\oint_{\Gamma} -gzn d\Gamma \approx -gA_c^z \Delta x (z_n - z_s) = -gA_c^z \Delta x \Delta z. \quad (3.10)$$

When Eq. (3.9) is combined with (3.10) above, we find that the result is the discrete alternative of $\nabla p = -g$ and that we have found the proper discretization of the external force term. It would not have been possible to include the face aperture A_c^z in the discretization of the gravity force, if the step from volume integral to surface integral had not been made.

3.3.4 Time discretization

The fluxes that were found in the previous sections can be rewritten to matrix coefficients multiplied by vectors that contain the discrete solution variables. We then obtain a divergence matrix \mathcal{M} for the discrete continuity equation:

$$\mathcal{M}\mathbf{u}_d = 0, \quad (3.11)$$

where \mathbf{u}_d contains the discrete velocities.

For the terms in the discrete moment equation we obtain a convective matrix \mathcal{C} , a diffusive matrix \mathcal{D} and a gradient matrix \mathcal{G} . The entire discrete momentum equation then becomes:

$$\mathcal{V} \frac{\partial \mathbf{u}_d}{\partial t} = -\mathcal{C}(\mathbf{u}_d) \mathbf{u}_d - \frac{1}{\rho} \mathcal{G} \mathbf{p}_d + \nu \mathcal{D} \mathbf{u}_d + \mathbf{F}_d. \quad (3.12)$$

In (3.12) \mathcal{V} is a diagonal matrix that contains the control volume size, \mathbf{p}_d is a vector containing the discrete pressures and \mathbf{F}_d is a vector that accounts for the discrete external force, which includes grid information. For the convective term this notation has been chosen to show that it is a nonlinear term and that elements of the vector \mathbf{u}_d have been used to construct the matrix.

Now, explicit forward Euler in time is used for the temporal discretization. The velocities in nonlinear terms of the momentum equation are chosen at the old time level t^n . The velocities in the continuity equation are chosen at the new time level t^{n+1} to ensure a divergence free velocity field at this level. As a result, also the pressure needs to be evaluated at the new time level.

When the superscripts that indicate the time level are added to the solution variables, the system of equations becomes:

$$\mathcal{M}\mathbf{u}_d^{n+1} = 0, \quad (3.13)$$

$$\mathcal{V} \frac{\mathbf{u}_d^{n+1} - \mathbf{u}_d^n}{\Delta t} = -\mathcal{C}(\mathbf{u}_d^n) \mathbf{u}_d^n - \frac{1}{\rho} \mathcal{G} \mathbf{p}_d^{n+1} + \nu \mathcal{D} \mathbf{u}_d^n + \mathbf{F}_d^n. \quad (3.14)$$

Now, the predictor velocity $\tilde{\mathbf{u}}_d$ is introduced. This auxiliary vector will contain the contributions of convection, diffusion and external forcing at the old time level:

$$\tilde{\mathbf{u}}_d^n = \mathbf{u}_d^n - (\mathcal{C}(\mathbf{u}_d^n) \mathbf{u}_d^n - \nu \mathcal{D} \mathbf{u}_d^n - \mathbf{F}_d^n). \quad (3.15)$$

With the predictor velocity, the discrete momentum equation becomes:

$$\mathbf{u}_d^{n+1} = \tilde{\mathbf{u}}_d^n - \Delta t \mathcal{V}^{-1} \frac{1}{\rho} \mathcal{G} \mathbf{p}_d^{n+1}. \quad (3.16)$$

The momentum equation is substituted into the continuity equation in Eq. (3.14). The pressure vector on the new time level t^{n+1} remains on the left-hand side of the equation. The predictor velocity is shifted to the right-hand side of the equation. With the property that $\mathcal{G} = -\mathcal{M}^T$ we observe that a discrete Poisson equation for the pressure is obtained:

$$\mathcal{M} \mathcal{V}^{-1} \mathcal{M}^T \mathbf{p}_d^{n+1} = \frac{\rho}{\Delta t} \mathcal{M} \tilde{\mathbf{u}}_d^n. \quad (3.17)$$

When the pressure vector at the new time level has been resolved, the velocity vector at the new time level \mathbf{u}_d^{n+1} can be found from Eq. (3.16).

3.3.5 Stability

The convective matrix derived above is a skew-symmetric operator. The diffusive matrix is a symmetric negative definite operator. Verstappen and Veldman [51] present an evaluation of the kinetic energy. Due to the symmetry properties of the discrete convective operator, there is no artificial increase of energy and energy is only dissipated as a result of diffusion.

Dröge and Verstappen [12] show that convective stability for first-order upwind discretizations is guaranteed as long as the Courant number based on the uncut cell size remains smaller than one:

$$\left| \frac{u}{\Delta x} + \frac{v}{\Delta y} + \frac{w}{\Delta z} \right| \Delta t \leq 1 \quad (3.18)$$

Diffusive stability is obtained when the following criterion is satisfied:

$$2\nu \left(\frac{1}{\Delta x^2} + \frac{1}{\Delta y^2} + \frac{1}{\Delta z^2} \right) \Delta t \leq 1 \quad (3.19)$$

The diffusive term in the momentum equation was already determined as if cells were uncut. Therefore also this criterion is based on the uncut cell size.

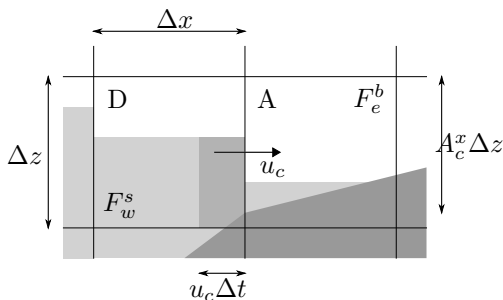


Figure 3.7: Flux of fluid from the donor cell D to the acceptor cell A . The flux depends on the velocity, time step and cell face aperture A_c^x . Limiter functions are applied to ensure that the D -cell is not drained beyond its contents F_w^s , and the A -cell not filled beyond its capacity F_e^b .

3.4 Free surface

The fluid displacement method in COMFLOW was originally introduced as the Volume Of Fluid-method by Hirt and Nichols. In this method, fluid fragments are convected from one cell to another, after which the position of the free surface is resolved by reconstructing it from the filling rates of cells. Fluid convection satisfies the following equation, which is the equivalent of Eq. (2.10) applied to the fluid volume of a single cell:

$$\int_{\Omega} F^s d\Omega + \oint_{\Gamma} F^s (\mathbf{u} \cdot \mathbf{n}) d\Gamma = 0. \quad (3.20)$$

When the fluid convection for all cells has been determined, the position of the free surface can be reconstructed from the new fluid distribution. From Eq. (3.20) we find that the change in fluid volume can be determined by accounting for the fluxes over the cell faces. The convective term in the fluid displacement equation shows strong resemblance to the convective term in the momentum equation.

The flux over a cell face in horizontal x -direction, when the horizontal velocity u_i is positive, can be approximated as follows:

$$\mathcal{F}_w^s = F_w^s u_c \Delta t A_c^x \Delta z. \quad (3.21)$$

Sufficiently far away from the free surface the net flux from (and to) a cell is zero. Near the free surface, however, the flux to and from cells will change their filling rate. Depending on the sign of the velocity at a cell face, the cell will become a donor or an acceptor cell (see Fig. 3.7).

Sometimes the flux from a cell might drain the cell beyond its fluid content. Or a cell might be filled beyond its capacity. Overfilling and overdraining are prevented by limiter functions. For the exact form of the limiter functions, refer to [27].

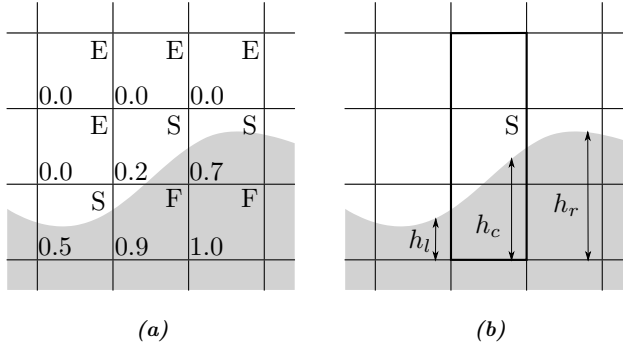


Figure 3.8: Instead of fluxing the individual VOF-values, shown in (a), the local height function h_c in (b) is used to convect the aggregated fluid in the array around the central S-cell. In this figure $h_l = 0.5$, $h_c = 1.1$ and $h_r = 1.7$.

Still, because the donor-acceptor algorithm is applied in multiple directions, and each direction is dealt with individually, cells may sometimes be filled or drained beyond their capacity. In the Hirt and Nichols VOF method, cells with $F^s > F^b$ are artificially set back to F^b . Cells with $F^s < 0$ are set back to zero. As a result, mass can be lost or gained during a simulation, which is undesirable.

Local height function

Due to the cell-by-cell approach in the original VOF-method, fluid is displaced without consideration for the position of the main fluid body. Consequently, fluid particles can disconnect from the free surface. If the size of these particles is of the order of the grid size, they can no longer be convected by means of velocities stemming from the numerical method. The particles become frozen and will stay in position for the remainder of the simulation. Disconnecting droplets have become known under the name *flotsam and jetsam* [41] and are a well know artefact of the VOF-method.

In this numerical method, a local height function is used to reduce both the occurrence of flotsam and jetsam, and mass loss due to round-off errors. With a local height function the cell-by-cell approach is abandoned and an array of cells is used to convect fluid. Depending on the orientation of the free surface, fluid from multiple connecting cells is redistributed in such a way that the aggregated fluid connects with the main body of fluid. The aggregated fluid is stored in a scalar function value and the function value is used to convect fluid, instead of the filling rates of the individual cells. In this research an array of three cells in each direction is used, see Fig. 3.8.

According to Kleefsman et al. [33], a local height function reduces the number of disconnecting droplets to a great extent and brings down mass loss to practically nothing.

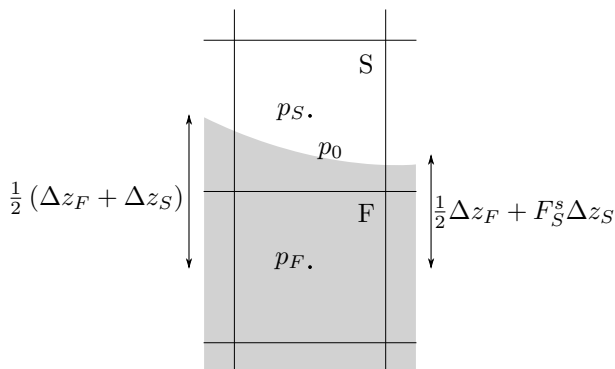


Figure 3.9: The pressure in a S -cell p_S is obtained from interpolation towards the reference pressure p_0 . The interpolation depends on the orientation of the free surface.

3.5 Boundary conditions

Picture the domain as a box with side faces, a bottom face and a top face. The bottom face of the domain is impermeable by design, as is the top face of the domain. Impermeability is obtained by setting the following boundary condition:

$$\mathbf{u} \cdot \mathbf{n} = 0. \quad (3.22)$$

The side walls of the domain can either be open or closed. Closed walls result from application of the same boundary condition in Eq. (3.22) above. Open boundaries are discussed in Chapter 5.

The main concern with respect to boundary conditions in this section goes out to the free surface. In simulations where field equations for pressure and velocity are only solved in water, the free surface functions as a formal boundary and boundary conditions need to be applied.

Pressure at the free surface

The term $\mathcal{M}\mathcal{V}^{-1}\mathcal{M}^T\mathbf{p}_d$ in Eq. (3.17) cannot be continued beyond the free surface. Therefore, boundary condition (2.13) for the tension in normal direction to the boundary is applied. On the scale of offshore structures being impacted by waves with wave lengths in the order of the length of the structure, the effect of viscosity and surface tension in the boundary condition can safely be ignored.

At the free surface, the effect of atmospheric pressure is modeled by imposing a reference pressure p_0 at the exact position of the free surface. The value of the pressure in a surface cell then follows from interpolation towards this reference pressure:

$$p_S = \alpha p_0 + (1 - \alpha) p_F, \quad (3.23)$$

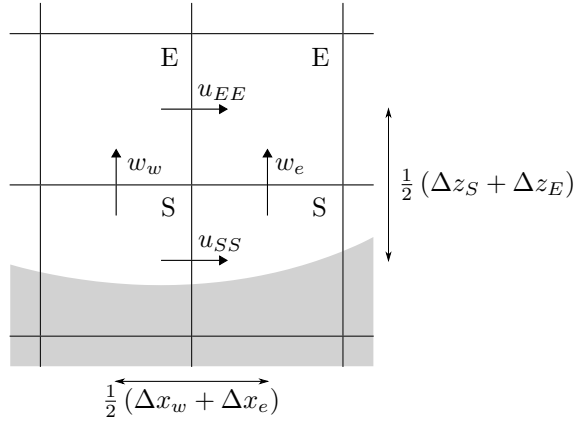


Figure 3.10: Boundary condition for the velocity at the free surface when it is nearly horizontal. SE-velocities are extrapolated from within the main body of the fluid. The direction of extrapolation depends on the orientation of the free surface. EE-velocities stem from the tangential stress condition.

in which p_S is the pressure in a S-cell and p_F is the pressure in a F-cell closest to the free surface. The direction of interpolation depends on the orientation of the free surface. Assuming the free surface is almost horizontal and the direction of interpolation vertical, then the interpolation coefficient becomes (see Fig. 3.9):

$$\alpha = \frac{\Delta z_F + \Delta z_S}{\Delta z_F + F_S^s \Delta z_S}. \quad (3.24)$$

Velocities at the free surface

Velocities near the free surface are indicated with the labels of the cells they are in between of; the velocity between two F-cells is then labeled as a FF-velocity. In our numerical method, a momentum equation is solved for FF-, FS- and SS-velocities. Near the free surface, when SS-velocities need to be computed, the stencil is incomplete and boundary conditions for the velocity are required.

Boundary conditions are formulated for SE- and EE-velocities. They are treated differently. SE-velocities are obtained by extrapolation from the main body of the fluid. Either constant or linear extrapolation is applied. Linear extrapolation leads to more accurate wave simulations, but according to [32] it can result in instabilities and very high velocities near the free surface. The difference between constant and linear extrapolation is further explored in Chapter 4.

EE-velocities are obtained from the tangential stress condition in Eq. (2.14). It is formulated in normal and in tangential direction. Here we keep the orientation of the

free surface grid aligned. When the free surface is (almost) horizontal, the following condition is applied:

$$\frac{\partial u}{\partial z} + \frac{\partial w}{\partial x} = 0.$$

The approximation to the equation above is found from central differencing. We then obtain for the EE-velocity in Fig. 3.10:

$$u_{EE} = u_{SS} - \frac{\Delta z_S + \Delta z_E}{\Delta x_w + \Delta x_e} (w_e - w_w). \quad (3.25)$$

Chapter 4

Free surface waves

The numerical method in COMFLOW will be used for wave impact simulations on offshore structures. In this chapter, the simulation of waves without a structure in the domain is investigated. Simulations for standing and propagating waves are analyzed and results are compared to analytical wave theory.

4.1 Definitions

The free surface waves discussed in this research are disturbances of the interface between water and air. In the absence of external forcing a free surface in a closed domain will be a plane perpendicular to the direction of gravity. Wind can cause disturbances and so can, for instance, ships as they travel through the water/air interface.

Regardless of how they are made, disturbances in the free surface do not stay in one position. As they propagate away from the source of the disturbance, waves continually exchange potential energy for kinetic energy and vice versa. When the surface elevation is measured at a fixed position, the resulting signal will be an oscillation around some mean level.

Free surface waves have a number of interesting characteristics, which are more easily discussed when several key concepts regarding waves have been defined in advance. The mean level, around which the variation takes place, will be called the mean surface level, abbreviated as MSL. It is customary in offshore applications to have the origin of the axis system in MSL, with the vertical axis in z -direction pointing upwards.

The variation around MSL is the surface elevation as a function of time and space, $\zeta = f(t, x, y)$. Regular free surface waves with surface elevations much smaller than one, can be described by periodic functions, such as:

$$\zeta = a \cos(t, x, y). \quad (4.1)$$

The amplitude of the wave is then denoted by a .

Wave crests are (local) maxima of the function describing a wave. Reversely, wave troughs are minima. The vertical distance between a wave crest and a consecutive wave trough is called wave height, H . The distance in time from one wave crest to another is the period, T . Similarly then, λ can be defined as the wave length, which is the distance in space between two consecutive wave crests. Note that the preceding parameters only make sense when waves are regular.

Period and wave length are often converted to their reciprocal parameters: the frequency ω and the wave number k . It is customary in offshore engineering to express these parameters as angles in radians. Then:

$$\omega = \frac{2\pi}{T} \text{ and } k = \frac{2\pi}{\lambda}.$$

Water is a dispersive medium: long waves propagate faster than short waves. The wave length depends on the frequency of the regular wave and the water depth, h . The water depth is the distance between MSL and the bottom. Without bottom topology variation, the bottom is defined by the plane $z = -h$. For steeper waves, the wave length for a given frequency also depends on the wave height. This is a nonlinear effect.

The equation that describes the interdependence between propagation (or phase) velocity, c , and wave length is called *dispersion relation*. The dispersion relation for small amplitude waves is derived in Appendix A about potential wave theory. The phase velocity and the dispersion relation will often be used in the chapter about the absorbing boundary condition, Chapter 6. It will be stated there and thoroughly discussed.

The variables described above are combined in Fig. 4.1. With the basic wave parameters defined, we can investigate how well waves and wave behaviour are represented within the numerical method described in Chapter 3. Investigation is performed by careful inspection of the simulation results and comparison to (simplified) theory.

4.2 Accuracy of wave simulations

The numerical method incorporated in the COMFLOW program is designed to be robust and accurate in terms of pressures and surface elevations in simulations of violent free surface impact events. Examples of these events are, for instance, a dambreak against a structure in the flow [32] and internal liquid sloshing inside models of liquid natural gas (LNG) tanks [54].

Another type of simulation tries to realistically reproduce free surface impact events in ocean environments. The impact events, then, are the result of the interaction between free surface waves and a bottom founded or floating structure at sea. This introduces the additional requirement for the numerical method to accurately simulate the creation and propagation of free surface waves *before* the interaction with the structure leads to violent impact events.

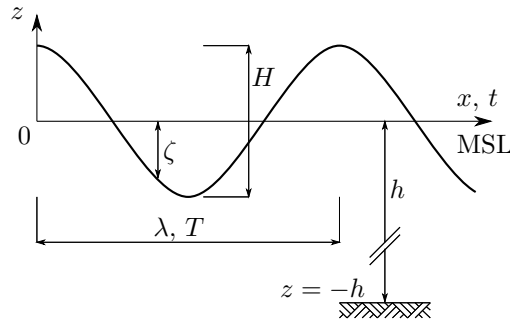


Figure 4.1: Wave parameter definitions.

The robustness introduced above comes at a price. Upwind discretization of the convective terms in the momentum equation gives stable results on coarse grids, but also introduces *artificial viscosity*. Artificial viscosity contributes significantly to energy dissipation in the system.

Another, often under-appreciated source for artificial energy dissipation is the free surface displacement method [31]. The *donor/acceptor* algorithm (DA) introduced by Hirt and Nichols [27] can be considered as an upwind discretization of the convective term in the free surface transport equation. No vocabulary such as ‘artificial viscosity’ has yet been attributed to this form of upwind discretization, but it leads to wave energy dissipation nonetheless.

Surface elevation and (potential) energy are very much related. The result of numerical energy dissipation is that the surface elevation of simulated waves, expressed in the wave height, becomes smaller over time and propagated distance. The effect of upwind discretization is stronger in steeper waves (see Fig. 4.4a). In very steep waves, a significant part of the wave height can get lost to energy dissipation over as little as one wave length’s distance.

Numerical methods for mild wave behaviour near a structure, such as 3D Boundary Element Methods (BEM) in the frequency domain, have been around for over twenty years [38]. Extensive simulations with 3D BEM software can be performed within the hour. The added value of the time intensive numerical method described above, is in simulating extreme free surface events in steep waves. It is, therefore, of key importance that waves remain steep until they reach the structure.

In this chapter the effect of upwind discretization of the convective terms in either the momentum equation or the transport equation of the free surface, is quantified and improving alternatives are introduced.

4.3 Simplifications

To study the individual contributions of the upwind discretization of the convective terms and the DA method to the overall dissipation of energy, a simplified method is introduced.

We wish to consider only the *additional* dissipation as a result of the numerical scheme. There is also true, physical dissipation of energy due to the diffusive term in the momentum equation. The dissipation as a result of viscous, diffusive effects is temporarily ignored by performing simulations in which the kinematic viscosity ν is equal to zero.

Only one phase is considered, which means that the discrete equations are only solved in that part of the domain that contains fluid (water). The addition of a second fluid in the form of air above the free water surface and the discretization of the density transition from water to air can lead to additional dissipation of energy [54].

The final simplification is that a height function is introduced to describe the surface elevation. A height function is sufficiently adequate to describe waves before breaking. In comparison to the donor/acceptor algorithm, however, it is far simpler to work out concepts for improving the accuracy of the free surface description.

The height function is determined by integration of the continuity equation in vertical direction:

$$\int_{-h}^{\zeta} \left(\frac{\partial u}{\partial x} + \frac{\partial w}{\partial z} \right) dz = 0. \quad (4.2)$$

Rewriting the integral yields:

$$\frac{\partial}{\partial x} \int_{-h}^{\zeta} u dz - u \frac{\partial \zeta}{\partial x} - u \frac{\partial h}{\partial x} + w|_{-h}^{\zeta} = 0. \quad (4.3)$$

Note in (4.3) that if the bottom is impermeable, then $w|_{-h}$ is zero. Also note that in the absence of bottom variation, $\partial h/\partial x = 0$. The remaining terms exactly equal the time derivative of the surface elevation in the kinematic free surface boundary condition in Appendix A:

$$\frac{\partial \zeta}{\partial t} + u \frac{\partial \zeta}{\partial x} - w|_{\zeta} = 0. \quad (4.4)$$

After substitution of this equation, the resulting relation for the height function in analytical form equals:

$$\frac{\partial \zeta}{\partial t} + \frac{\partial}{\partial x} \int_{-h}^{\zeta} u dz = 0. \quad (4.5)$$

Note that (4.5) is a conservation law in contrast to (2.10) in Chapter 2.

For the horizontal position, where the surface elevation ζ is to be considered, we consider a vertical column of grid cells. The surface elevation will be evaluated midway in between column faces in alignment with the horizontal position of the pressure points in that column. In hydrostatic situations, then, the pressure at multiple elevations in the column can be directly resolved from the surface elevation.

The vertical column of grid cells is chosen to be the control volume, in which we approximate Eq. (4.5). Forward Euler is used for the time derivative and the change in volume depends on the fluxes over the column faces:

$$\zeta_c^{n+1} = \zeta_c^n - \frac{1}{\Delta x_c} (\mathcal{F}_e - \mathcal{F}_w), \quad (4.6)$$

in which \mathcal{F}_e and \mathcal{F}_w are the fluxes over the eastern and western control volume face.

The total flux over the control volume face consists of the summation of fluxes from individual cells. For F-cells the flux is equal to

$$\mathcal{F}_F = u_F \Delta t \Delta z_F. \quad (4.7)$$

In S-cells the flux depends on the surface elevation. The surface elevation within a cell is assumed to be constant. The flux from an S-cell can then be determined as

$$\mathcal{F}_S = u_S \Delta t (\zeta_c - z_s), \quad (4.8)$$

where z_s is the vertical coordinate at the south side of the S-cell.

The flux calculation from the S-cell has been illustrated in Fig. 4.2. It shows the surface elevation in a column of cells midway in between vertical column faces. The surface cell has been enlarged. The surface elevation is assumed constant within cell columns and the fluxes at S-cell faces are determined using this assumption.

4.4 Standing waves

4.4.1 Method of testing

To test the free surface displacement method and *only* the displacement method, standing wave simulations are performed. Standing waves can be simulated in a closed domain with natural boundary conditions. A closed domain removes the need for wave generation and absorption at the boundary, which can interfere with the results and the interpretation of these results.

Still, standing wave simulations are well suited to assess the performance of the numerical method for free surface events [44], because all the important dynamics are included: a free surface is present, which can be steep, and the steeper the wave, the larger the velocity gradients will be. Large velocity gradients are essential. In small amplitude standing wave simulations, nonlinear effects are negligible and hardly any energy dissipation is present, because the system will effectively be a set of linear equations approximated with central discretization.

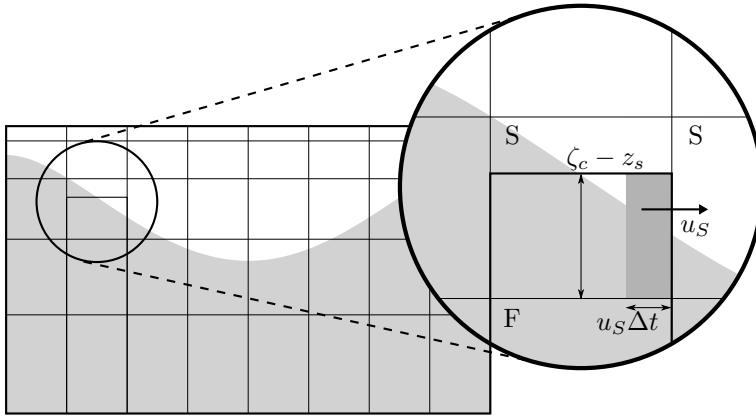


Figure 4.2: Flux from an S-cell. The flux over the eastern cell face is indicated by the dark grey area. The flux volume depends on the horizontal velocity in the cell face and the position of the free surface.

The initial condition of the standing wave simulations in this chapter, is a free surface prescribed by means of a cosine function with a certain amplitude. At time t_0 the free surface is released and a harmonic solution of the free surface is obtained. As the amplitude of the cosine function is increased, higher harmonics in the free surface elevation are generated. This is a nonlinear effect, in which energy transfer of a certain base mode towards higher harmonics takes place.

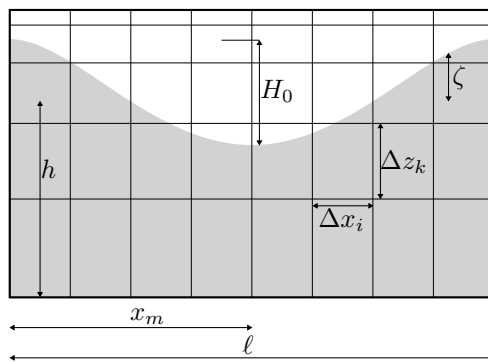


Figure 4.3: Setup of the standing wave simulation.

The surface elevation is measured in the middle of the domain. The remaining parameters are summarized in Table 4.1 and shown in Fig. 4.3:

Table 4.1: Domain and grid

Parameter	Symbol	Value
Water depth	h	10m
Domain length	ℓ	50m
Measurement position	x_m	25m
Horizontal grid distance	Δx	1m
Vertical grid distance	Δz_{min}	0.5m
Vertical grid distance	Δz_{max}	1m
Vertical stretch factor	ξ	1.05 [-]
Time step	Δt	0.01s
Simulated time	T	500s

Over time the surface elevation at a certain measurement location will become gradually lower. In absence of physical energy dissipating mechanisms, the reduction of the surface elevation can only be attributed to artificial energy dissipation of the numerical scheme.

Below, two situations are depicted. Figure 4.4 shows the surface elevation at the measurement location over time for increasingly larger amplitude waves. The dissipation over time is represented by the decreasing wave height over time, made dimensionless by the initial wave height. It is plotted on logarithmic scale. There is no dissipation for very small amplitudes, but when waves become steeper, the rate of dissipation increases. On the left of Fig. 4.4 the actual free surface for the largest amplitude wave ($\zeta_a = 2m$) is shown; this wave will be the reference case in this chapter.

The rate of dissipation depends on the grid size. Increasing the resolution leads to a reduced rate of dissipation. A grid convergence study has been performed to show what the solution will be, when there is less dissipation in the system. It also shows what is to be expected of the improved numerical methods discussed in this chapter. This is depicted in Fig. 4.5.

4.4.2 Velocity extrapolation at the free surface

In one-phase mode, the free surface is an actual boundary and boundary conditions for pressure and velocity at the free surface are required. In section 3.5 the current boundary conditions are described. The pressure at the free surface is determined by interpolation towards a reference pressure p_0 . SE-velocities are obtained by constant extrapolation from within the flow field and EE-velocities stem from the boundary condition that describes the balance of forces at the free surface.

Without viscosity and a boundary layer at the free surface - and on the scale of all our (offshore) applications this is almost always justified - the way the EE-velocities are determined is rather arbitrary. Constant extrapolation of these velocities is another choice and as can be seen from Fig. 4.6 the dissipation over time shows similar behaviour. The line indicated by 'Reference' in this figure, and similar figures in this

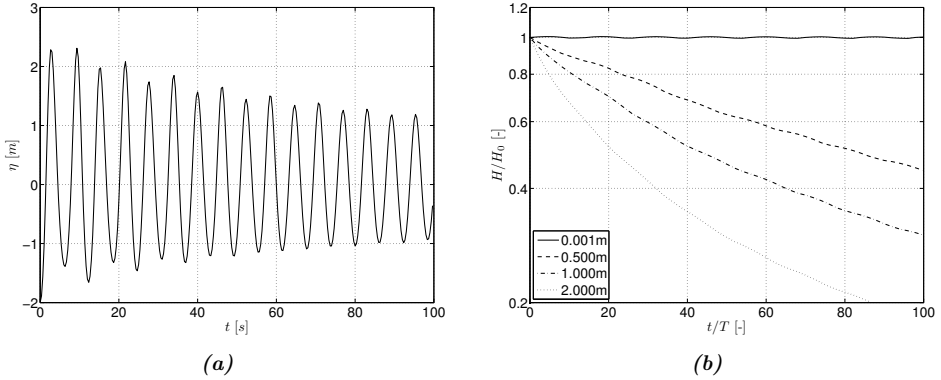


Figure 4.4: Dissipation in standing waves. In (b), steeper waves have a larger rate of dissipation. In (a), the actual free surface as a function of time for the largest amplitude wave in (b).

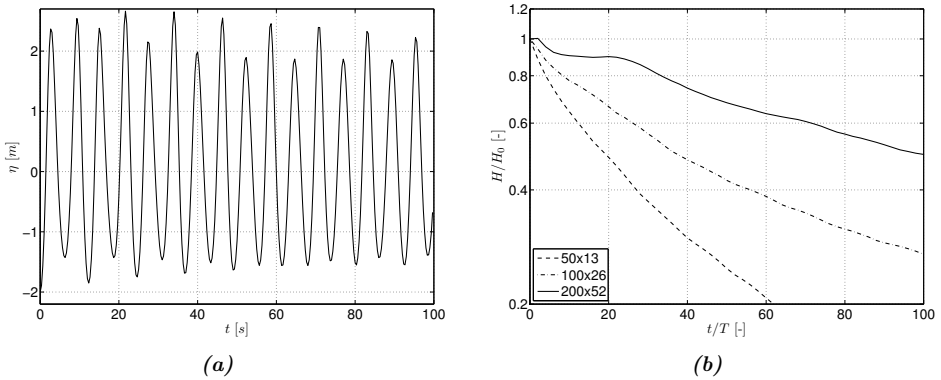


Figure 4.5: Dissipation in log-scale in standing waves when the grid resolution is increased. The initial wave height is equal to $H_0 = 4\text{m}$. The actual free surface for the finest mesh size is shown on the left.

chapter, is the dissipation as a function of time of the original method described in Chapter 3.

The dissipation behaviour over time changes, however, when instead of constant extrapolation, linear extrapolation is applied to determine both the SE and the EE-velocities. The direction of the extrapolation depends on the orientation of the free surface. If the free surface is assumed to be (almost) horizontal, the SE velocity, in this case a vertical velocity, and the EE-velocity, a horizontal velocity, are extrapolated in the vertical direction from below, see Fig. 3.10.

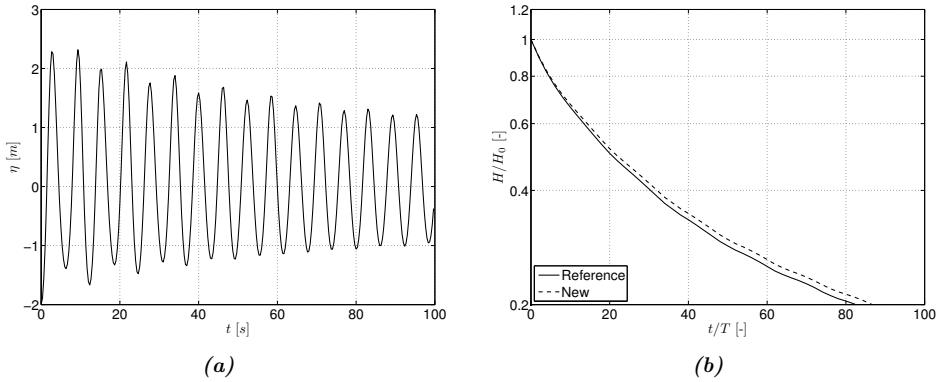


Figure 4.6: Damping of the original method with boundary conditions for the EE-velocities at the free surface, compared with constant extrapolation for these velocities. The initial wave height was $H = 4\text{m}$ and results are presented on log-scale.

When linear extrapolation is applied there is less dissipation. The behaviour of the surface elevation over time is almost the same, but after an equal number of periods, more of the surface elevation remains in the case of linear extrapolation compared to the original method. The surface elevation and the dissipation behaviour compared to the original method are shown in Fig. 4.7.

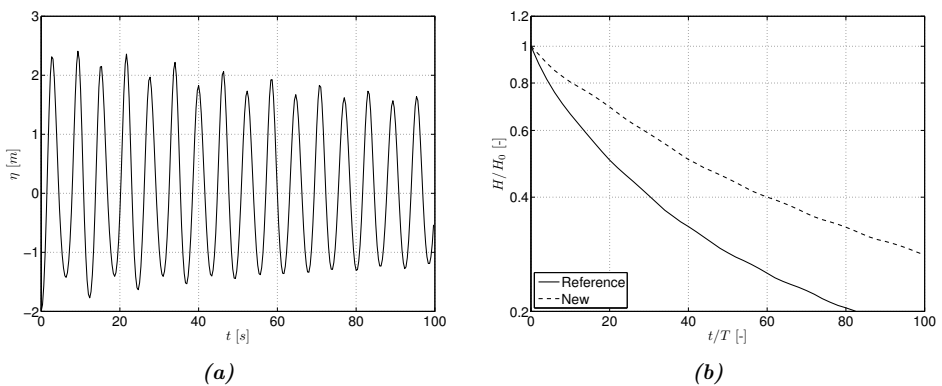


Figure 4.7: Damping on log-scale when the velocities at the free surface are determined by linear extrapolation. The initial wave height was $H = 4\text{m}$.

4.4.3 Free surface reconstruction

The volume-of-fluid VOF method of its own accord does not explicitly resolve the free surface. Instead, when determining the fluid configuration at the new time level t^{n+1} , it shifts around fluid fragments from one cell to another with the velocities throughout the body of the fluid. The new fluid distribution is administered by means of filling rates of cells, which relates the fluid volume in the cell to the cell volume itself.

Although the filling rates do not specify the exact position of the free surface, it can be reconstructed approximately from the filling rates by considering the filling rate in one cell in relation to the filling rates in the surrounding cells. Free surface reconstruction positions the fluid within a cell in such a way that the transition in the free surface between cells becomes less discontinuous.

The process of free surface reconstruction is best illustrated by a series of consecutive images that show the most basic reconstruction techniques. The images are shown in Fig. 4.8. The left-most illustration shows the filling rates, or VOF-function values, without an indication of where the free surface might be. No reconstruction has taken place.

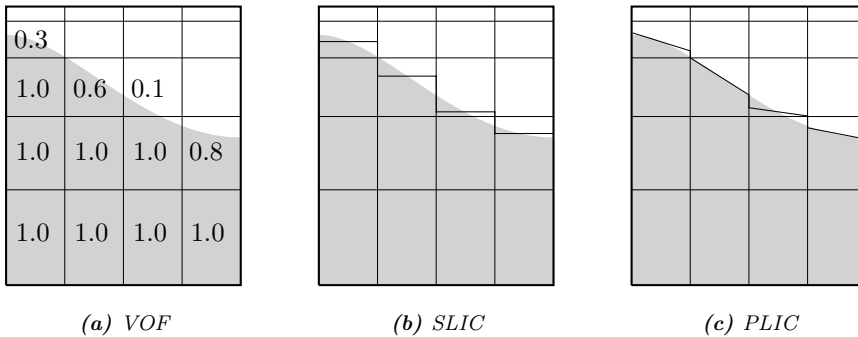


Figure 4.8: Methods of free surface reconstruction.

The illustration in the middle shows the free surface when the free surface is kept grid aligned. The configuration of the fluid within a cell is determined from the filling rates of the surrounding cells. This method of reconstruction is often referred to as simple line interface calculation or SLIC. The free surface of the wave, which is represented by the VOF-function values, is approximated rather crudely and the transitions in the free surface between cells are staircased and discontinuous.

On the right, in Fig. 4.8c, a much better free surface approximation is depicted. The free surface is still a straight line (or a plane in 3D), but the normal to the free surface, the free surface orientation, is not necessarily grid aligned. In the piecewise linear interface calculation (PLIC) the transitions in the free surface are still discontinuous, but the errors associated with the discontinuities are greatly reduced compared to the SLIC method.

One of the most apparent numerical errors in performing simulations with the SLIC free surface reconstruction is the occurrence of *flotsam and jetsam* [41]. These are droplets that disconnect from the main body of the fluid due to the poor representation of the free surface in combination with the donor/acceptor algorithm. Another numerical error often encountered in literature is that SLIC is not mass preserving as a result of round-off errors when SLIC is combined with the donor-acceptor algorithm.

Some authors [16] combine SLIC with a local height function to prevent disconnecting droplets and to ensure mass conservation. The local height congregates fluid fluxes from multiple cells and transports them as a whole from one set of cells to another. The number of cells, of which the fluid fluxes are combined, varies among authors. In our method, 3×3 cells in 2D are used, Afkhami and Bussmann [1] use 3×5 cells. The local height function, they reason, saves them the computational cost of using a PLIC method, which is reportedly [54] very time consuming.

While disconnecting droplets are reduced and the loss of mass is prevented by using SLIC free surface reconstruction and a local height function, other numerical errors remain. One, often unappreciated, aspect of the donor-acceptor algorithm is dissipation. In essence, the donor-acceptor algorithm is an upwind discretization of a transport equation. Upwind discretization of the convective term in the momentum equation (see Chapter 3) is known for its dissipative properties and that it leads to artificial viscosity. Upwind discretization of the convective term in the fluid transport equation also induces artificial diffusion.

This section intends to quantify the dissipation and present an alternative. The height function (note: *not* local height function) introduced in a previous section is combined with the concept of piecewise linear reconstruction (PLiC) of the free surface. The slope of the free surface within an S-cell is calculated and the slope is used to determine the amount of fluid that can be fluxed from that cell.

The slope a_i of the free surface within a cell in 2D depends on the surface elevation to the left and the elevation to the right of this cell. It may be regarded as a central discretization of the free surface gradient $\partial\zeta/\partial x$. On a uniform grid:

$$a_i = \frac{\zeta_{i+1} - \zeta_{i-1}}{\Delta x_i + \Delta x_{i+1}}. \quad (4.9)$$

The surface elevation is defined in the center of the cells. The surface elevation itself is not a volume. But when the surface elevation ζ_i within a column of cells is assumed constant, as has been done to determine the volume fluxes across cell faces, then Fig. 4.9a shows that ζ_i diminished by the z -value of the bottom face of the S-cell does represent a sort of volume:

$$V_S = \Delta x_i (\zeta_i - z_S). \quad (4.10)$$

Reconstruction of the free surface must not change the volume V_S in the S-cell in order to conserve mass. Mass conservation on the level of a cell is required for two reasons: first and foremost because the method of reconstruction needs to be combined with

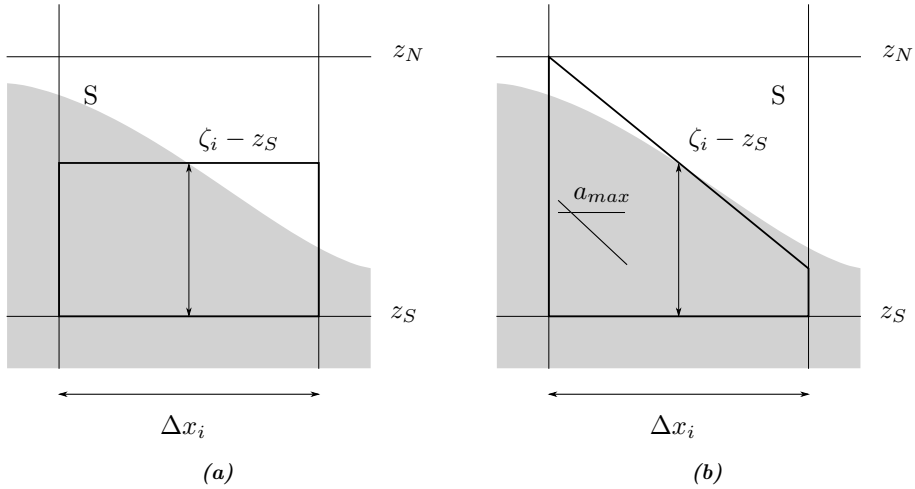


Figure 4.9: Volume in an S-cell. Left shows the volume when SLIC is used. Right shows the maximum slope of the free surface reconstruction when the volume is required to stay the same.

the donor/acceptor algorithm; secondly because the fluid cannot be shifted towards cells where velocities are not defined. Therefore, the slope of the free surface needs to be limited. This is shown in Fig. 4.9b. Once the reconstructed free surface at a cell face reaches the top or bottom of the cell, the maximum slope is obtained. This implies that:

$$|a_i| \leq \min \left(\frac{2(\zeta_i - z_S)}{\Delta x_i}, \frac{2(z_N - \zeta_i)}{\Delta x_i} \right). \quad (4.11)$$

The slope limiter reduces the accuracy of the piecewise linear reconstruction, but a consistent mass conserving alternative in combination with the height function is not readily available.

Once the slope in an S-cell has been calculated, the fluxes at the cell faces are determined. The flux follows from an integration of the fluid distribution function over a distance $u_i \Delta t$. The fluid fluxed from the cell equals

$$\mathcal{F}_i = \left(\zeta_i + \frac{a_i}{2} \Delta x_i \right) u_i \Delta t - \frac{a_i}{2} (u_i \Delta t)^2, \quad (4.12)$$

when u_i is positive. When u_{i-1} is negative, the fluid flux equals

$$\mathcal{F}_{i-1} = \left(\zeta_i - \frac{a_i}{2} \Delta x_i \right) u_{i-1} \Delta t + \frac{a_i}{2} (u_{i-1} \Delta t)^2. \quad (4.13)$$

The fluid fluxes are indicated schematically in Fig. 4.10.

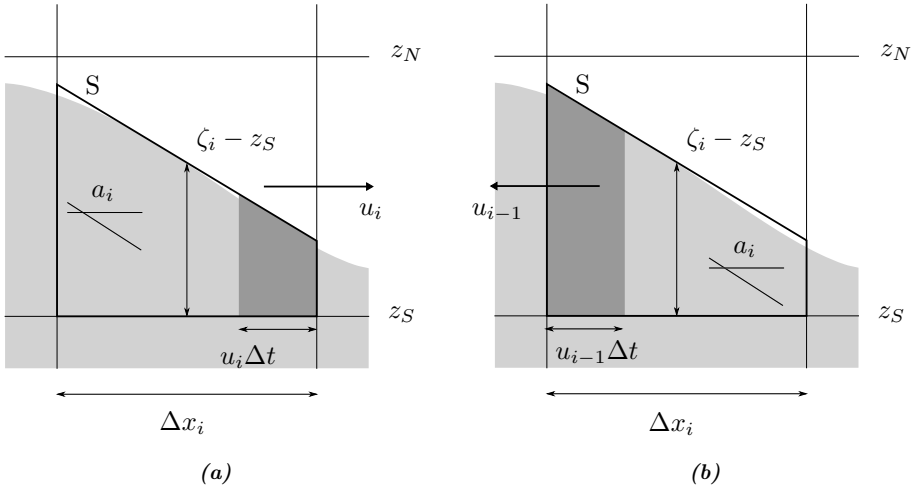


Figure 4.10: Fluxes from an S-cell when PLIC is applied.

The piecewise linear reconstruction of the free surface has been applied in a standing wave simulation. The parameters for this simulation are the same as in Table 4.1. The surface elevation at the measurement position in the middle of the domain is plotted as a function of time in Fig. 4.11. Compared to the original method, the dissipation over time shows the same behaviour. The dissipation, however, is slightly less: after 20 periods, 65% of the original wave height remains.

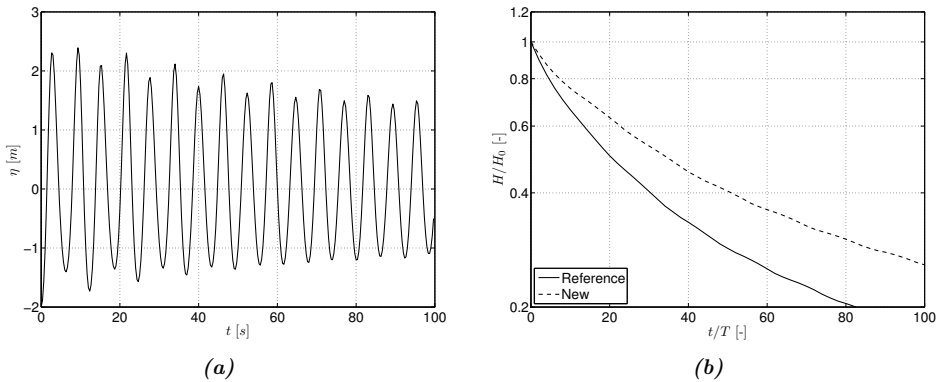


Figure 4.11: Wave damping on log-scale when piecewise linear reconstruction of the free surface is used instead of piecewise constant reconstruction. The initial wave height was $H = 4\text{m}$.

4.4.4 Convective term in the momentum equation

The original method described in Chapter 3 uses either upwind or central discretization of the convective term in the momentum equation. The central discretization possesses the energy conserving properties, but requires a certain minimum grid spacing to be free of spatial instabilities ('wiggles'). The minimum grid spacing requirement is usually too demanding for a desktop pc to perform a simulation with an offshore application.

Offshore applications, with a focus on impact calculations, do not require an accurate representation of boundary layers. The default option in these simulations is almost always a first order upwind discretization of the convective term. First order upwind introduces artificial viscosity and it can be seen that first order upwind not only has an effect on boundary layers, but also on the overall energy level in the system. As a result of artificial viscosity, the surface elevation in standing wave simulations rapidly decays over time.

Other discretizations of the convective term in the momentum equation are possible. Since central discretization is not available, some use second order upwind discretization to reduce energy dissipation [54] during simulations. Second order upwind requires a larger stencil. The larger stencil cannot be used at boundaries, such as the bottom, solid walls on either side of the domain and also the free surface. At those locations first order upwind discretization is used, which implies that the space discretization throughout the domain is a combination of first order upwind and second order upwind.

Second order upwind also has a very restrictive stability limit for the time integration. Second order upwind discretization of the convective term in combination with Forward Euler time discretization requires a CFL criterion which is much smaller than one. [54] therefore also chooses a higher order time discretization. The Adams-Bashforth time discretization is an explicit time integration method that combines information from two consecutive time levels to determine the solution variables at the new level.

In our numerical method, the grid locations where solution variables are determined, can change from one time level to the other. To apply Adams-Bashforth time integration at these locations then requires information that has never before been determined. One option to deal with the lack of information is to extrapolate variables to those locations when required. Another option is to apply the default forward Euler time integration at those locations. The time integration procedure then varies between cells. Also note that the time integration procedure of the free surface convection is still Forward Euler.

The discretization of the convective term in the momentum equation can be improved without the need for a larger stencil at the boundaries and without the need for another time integration method to overcome the reduced stability properties of the higher order spatial discretization method.

Lax-Wendroff discretization techniques combine the time and spatial discretization. The solution variables at the new time level follow from an interpolation of the vari-

ables at the old level in the space-time plane. For a proper discretization of the convective term, solution variables at the faces of the momentum control volume are required, see Fig. 4.12.

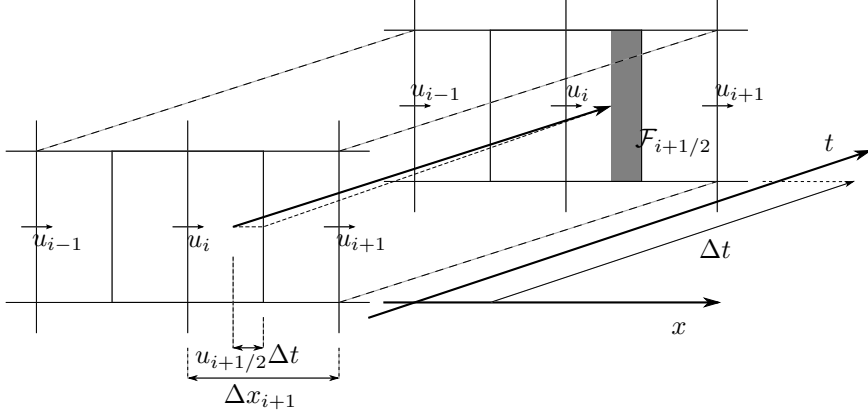


Figure 4.12: Lax-Wendroff discretization of the momentum flux. To determine the flux over the plane $x_{i+1/2}$ an interpolation is performed between u_i and u_{i+1} . The interpolation coefficients depend on the direction of $u_{i+1/2}$ and the time step Δt .

The interpolation depends on the direction of the velocity at the cell face. When $u_{i+1/2} \geq 0$, linear interpolation for the flux at cell face $x_{i+1/2}$ according the Lax-Wendroff method yields

$$\mathcal{F}_{i+1/2} = \mathcal{F}_{i+1/2}^m \left[\frac{\left(\frac{\Delta x_{i+1}}{2} + u_{i+1/2} \Delta t\right) u_i + \left(\frac{\Delta x_{i+1}}{2} - u_{i+1/2} \Delta t\right) u_{i+1}}{\Delta x_{i+1}}, \right] \quad (4.14)$$

in which $\mathcal{F}_{i+1/2}^m$ is the mass flux $u_{i+1/2} \Delta z$.

In Eq. (4.14) one can recognize a local CFL-criterion, which will be denoted by

$$\eta_{i+1/2} = \frac{u_{i+1/2} \Delta t}{\Delta x_{i+1}}. \quad (4.15)$$

Thus, when the velocity at the face of the momentum volume is positive, the flux at that face becomes

$$\mathcal{F}_{i+1/2} = \mathcal{F}_{i+1/2}^m \left[u_i + \left(\frac{1}{2} - \eta_{i+1/2}\right) (u_{i+1} - u_i) \right] \quad (4.16)$$

and when mass flux $\mathcal{F}_{i+1/2}^m$ is negative

$$\mathcal{F}_{i+1/2} = \mathcal{F}_{i+1/2}^m \left[u_i + \left(\frac{1}{2} + \eta_{i+1/2}\right) (u_{i+1} - u_i) \right]. \quad (4.17)$$

The fluxes at the remaining faces of the momentum control volume can be determined in a similar manner. With all convective fluxes known, the predictor velocity \tilde{u} can be calculated as in Eq. 3.15.

The Lax-Wendroff method is stable by design for CFL smaller than one.

4.4.5 Flux limiters

The Lax-Wendroff discretization as implemented is sensitive to spatial instabilities. If initially no wiggles are present, they will not be generated during a simulation. In our method, however, they will always be present. The extrapolation of velocities at the free surface, as described in section 4.4.2, is inherently imperfect.

The extrapolation introduces a deviation from the rest of the method, resulting in a discontinuity of either the first derivative (constant extrapolation) or the second derivative (linear extrapolation). The discontinuity generates wiggles and these wiggles at the free surface are transported downward into the body of the fluid, see Fig. 4.13.

To prevent wiggles the Lax-Wendroff method described above can be extended with flux limiters. The flux limiter used will adhere to the Total Variation Diminishing (TVD) concept. The following limiter function, Ψ , is introduced:

$$\Psi = \min(\max(0, r_i), 1), \quad (4.18)$$

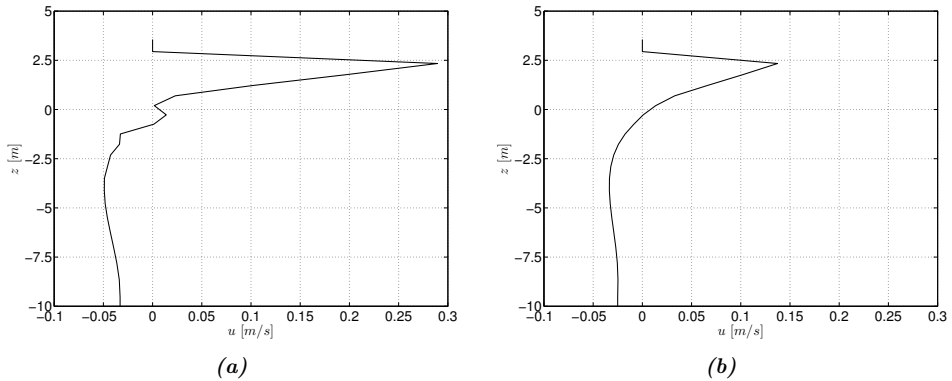


Figure 4.13: Horizontal velocity profile in vertical direction at $t = 2.5s$ and $x = 21.5m$ when the Lax-Wendroff convection scheme is used. In (a) wiggles are present. When flux limiters are used on top of the Lax-Wendroff scheme, there are no wiggles, but the velocities are significantly reduced.

in which:

$$r_i = \left(\frac{u_i - u_{i-1}}{\Delta x_i} \right) \left(\frac{u_{i+1} - u_i}{\Delta x_{i+1}} \right)^{-1}. \quad (4.19)$$

The limiter function is included into the flux calculation as in Eq. (4.20). When $\mathcal{F}_{i+1/2}^m \geq 0$:

$$\mathcal{F}_{i+1/2} = \mathcal{F}_{i+1/2}^m \left[u_i + \left(\frac{1}{2} - \eta_{i+1/2} \right) \Psi(r_i) (u_{i+1} - u_i) \right] \quad (4.20)$$

and when $\mathcal{F}_{i+1/2}^m \leq 0$:

$$\mathcal{F}_{i+1/2} = \mathcal{F}_{i+1/2}^m \left[u_i + \left(\frac{1}{2} + \eta_{i+1/2} \right) \Psi(1/r_{i+1}) (u_{i+1} - u_i) \right]. \quad (4.21)$$

When the velocities vary only mildly ($r_i \geq 1$), then the simulation benefits from the full potential of the Lax-Wendroff discretization and there will hardly be any dissipation. In the case of larger variations, increasingly less of the Lax-Wendroff discretization is used, until for large variations in velocity, $r_i \leq 0$, the limiter function is zero and upwind is the resulting discretization. Upwind will give the maximum amount of dissipation in order to prevent wiggles.

The results of the Lax-Wendroff discretization, extended with flux limiters, for the standing wave simulation are shown in Fig. 4.14. In this simulation Lax-Wendroff for convection has been combined with the piecewise linear reconstruction of the free surface. The surface elevation at the measurement location shows clear benefit from the improvements that have been suggested in this chapter. The standing wave simulation now shows less dissipation than the original method described in Chapter 3. Whereas the standing wave lost 50% of the initial wave height after 20 periods in Fig. 4.6, this has been reduced to 25% in Fig. 4.14.

4.5 Propagating waves

Different discretization methods to reduce wave energy dissipation in standing wave simulations have been discussed. Linear extrapolation of the velocities at the free surface was found to improve the results compared to the original method, as well as a piecewise linear reconstruction of the free surface and a different discretization of the convective term in the momentum equation.

The different methods will now be applied to the simulation of propagating waves. This chapter will not go into the generation of waves, nor will it show how to prevent wave reflection at the boundaries. These aspects of wave simulations will be discussed in Chapter 5 and 6. The main concern here is to quantify wave energy dissipation in simulations of propagating waves.

Waves in this experiment are regular and propagate in positive x -direction. Therefore, the wave height will decrease in this direction as a result of energy dissipation. The

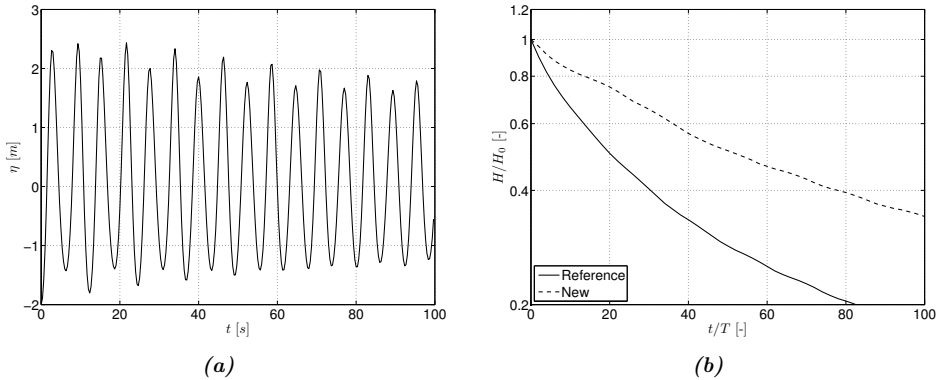


Figure 4.14: Wave damping on log-scale when the Lax-Wendroff for the convective term in the momentum equation is used, compared with upwind discretization in the original method. The initial wave height was $H = 4m$.

initial wave height is four meters at a period of six seconds. The water depth is ten meters. For this period, wave height and water depth, the wave length is close to fifty meters. Considering the ratio of wave height to wave length and wave length to water depth, these are mildly steep waves in shallow water and, as a result, nonlinear terms in the system of equations are considerable.

Reflected waves are not allowed to contaminate the results. The length of the domain is to be such, that reflection is prevented during the simulation. The fastest wave components propagate at $c = \sqrt{gh}$ and the domain length following from the criterion of no reflection is equal to $L = \sqrt{gh}T_{max}$, where T_{max} is the duration of the simulation. The duration should be long enough for a stable wave system to develop. A stable wave system is free of initialization effects and is obtained when the wave height at one location no longer varies in time. After 140 seconds this is true for at least ten consecutive wave lengths. The wave parameters and the numerical parameters, are summarized in Table 4.2.

As a first estimate of what to expect from the more accurate discretization methods, a grid convergence study with the original method is performed. In the grid convergence study, the grid was kept uniform. Cells measure $1m$ in both directions for the coarsest grid and the mesh size is reduced once to $0.5m$ and a second time to $0.25m$. Results for the dissipation as a function of the position in the domain are shown in Fig. 4.15. As the mesh width decreases, dissipation is reduced. On the finest grid, there is a distance of about one wave length, in which there is no visible dissipation. This is thought to originate from the discrepancy between the analytical solution imposed at the boundary and the discrete solution inside the domain. After one wave length a stable solution is obtained. The dissipation coefficient can be obtained from the slopes of the lines in Fig. 4.15.

Table 4.2: Domain and grid

Parameter	Symbol	Value
Water depth	h	10m
Horizontal grid distance	Δx	1m
Vertical grid distance	Δz_{min}	0.5m
Vertical grid distance	Δz_{max}	1m
Vertical stretch factor	ξ	1.05 [-]
Time step	Δt	0.01s
Simulated time	T	150s
Domain length	ℓ	1500m
Measurement position	t_m	140s

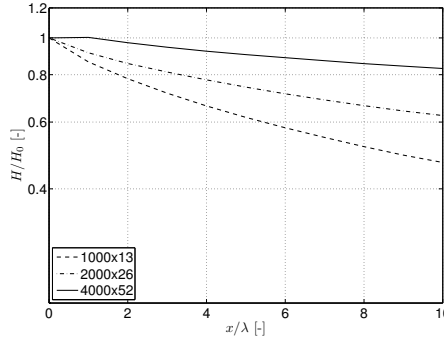


Figure 4.15: Dissipation of wave energy as waves propagate through the grid. Three different grids were used to obtain these results. As the grid resolution increases, the dissipation is reduced.

In Fig. 4.16 the surface elevation as a function of the horizontal position is plotted at time $t = 140s$. The figure also shows the normalized wave height on logarithmic scale, from which the dissipation coefficient can be found. These results have been obtained with the original method in COMFLOW. When the method features the techniques that have been described above – linear extrapolation of the velocities at the free surface, piecewise linear reconstruction of the free surface and the Lax-Wendroff scheme with flux limiters – less wave energy is dissipated over distance. This is shown in Fig. 4.17, where the original method is compared to the improved method.

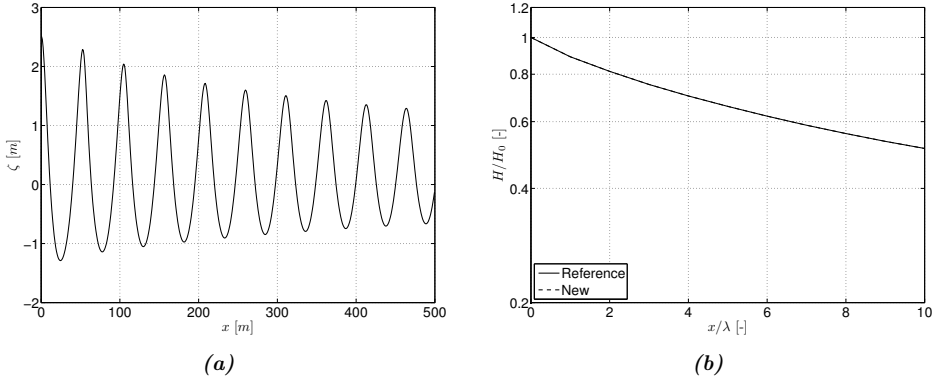


Figure 4.16: In (a) on the left, the surface elevation as a function of the horizontal position at $t = 140\text{s}$. The surface elevation has been obtained with the original numerical method in COMFLOW. In (b), the normalized wave height at several consecutive wave lengths. It is plotted on logarithmic scale to visualize the dissipation coefficient.

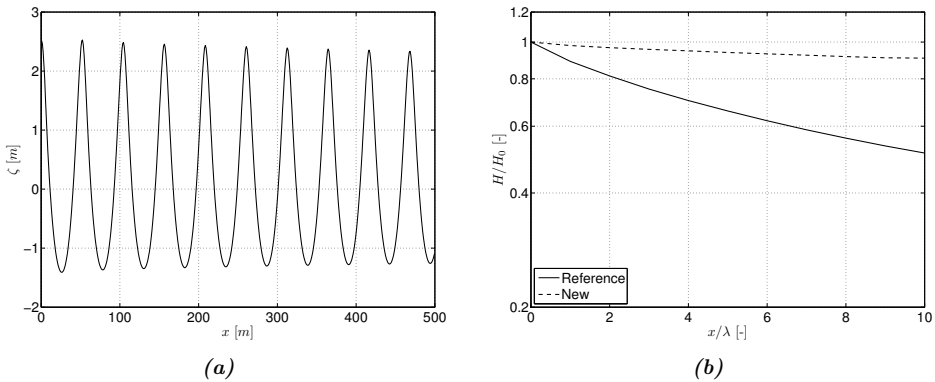


Figure 4.17: Wave energy dissipation, when instead of the original method, linear extrapolation of the velocities at the free surface, piecewise linear reconstruction of the free surface and the Lax-Wendroff method with flux limiters are used.

4.6 Discussion

Standing waves

When the dissipation as a function of time in the standing wave simulations is compared to the dissipation as a function of location in the propagating wave simulations

(Fig. 4.18), it is found that the Lax-Wendroff method with flux limiters gives better results for propagating waves than it does for standing waves. More specifically, the Lax-Wendroff method in Fig. 4.18 performs worse than the upwind method. This is puzzling, since the Lax-Wendroff scheme reduces to an upwind discretization when the limiter for very large gradients is set to zero. Results worse than upwind, then, are not expected. This subject is still a matter of ongoing research.

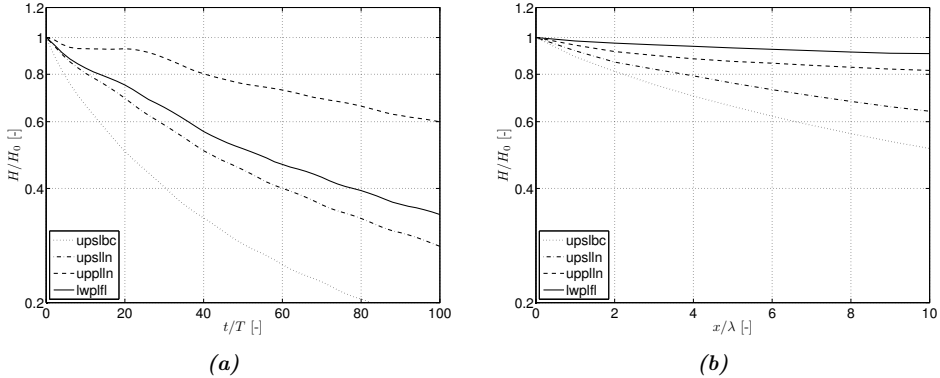


Figure 4.18: Wave energy dissipation for several combinations of discretizations. In (a), dissipation as a function of time in standing wave simulations. Combinations of two letter codes in the legend, such as ln for linear and sl for SLIC, were used to indicate methods. Then, upslbc indicates the original method. In (b), dissipation as a function of location in the propagating wave simulations.

Propagating waves

With regard to propagating waves, it has to be stressed again, that the numerical method in COMFLOW has not been developed for the main purpose of wave propagation. Its strength is in the accurate and stable simulation of highly distorted free surface configurations after wave impacts on structures and in the accurate representation of impact pressures.

The domain in an impact simulation is generally confined to the direct surroundings of the structure, with the domain boundaries not more than one or two significant (effective) wave lengths away from the structure. Dissipation is required for stable results. Unfortunately, dissipation also affects the representation of waves in the domain. Wave energy is dissipated as waves propagate through the domain, reducing the wave height of waves before they reach the structure.

In this chapter, it was found that wave dissipation is affected by the extrapolation of the velocities at the free surface. Linear extrapolation of the velocities gives less

dissipation than constant extrapolation. Dissipation also results from the free surface displacement algorithm: when piecewise linear reconstruction of the free surface is used rather than piecewise constant, wave energy dissipation is reduced. The final improvement was found in a different scheme for the convective term in the momentum equation. When the Lax-Wendroff method with flux limiters is used, the effect of artificial viscosity is reduced, resulting in less dissipation.

Relatively simple numerical techniques have been used to significantly bring back wave energy dissipation. In propagating wave simulations the energy dissipation, measured at a location four wave lengths away from the input boundary, has been reduced to just a couple of percent. In standing wave simulations, the energy dissipation after twenty periods has been reduced to 25%, when the Lax-Wendroff method is used. Considering the relative simplicity of the numerical techniques used in this chapter, further improvements in bringing back wave energy dissipation seem within reach. Additional research is required: it should consider (1) free surface reconstruction methods better than piecewise linear and (2) higher order convection schemes in the momentum equation.

Chapter 5

Incoming and outgoing waves

In the preceding chapters of this thesis, simulations have been discussed without much attention for the boundaries of the domain. The boundaries were mostly closed ($\mathbf{u} \cdot \mathbf{n} = 0$), except in the section about propagating waves. Here, velocities according to non-linear potential theory for waves were prescribed; that will be discussed later in this chapter.

A range of free surface phenomena, such as fuel sloshing inside satellites [16] and sloshing inside LNG tanks [54], can be simulated with closed boundaries. Offshore applications, however, often require open boundaries. To illustrate this requirement, several stages in the study of a green water event on the deck of an FPSO with subsequent impact are discussed [5].

Suppose our main interest is in the loads and pressures as a result of impact with a structure on deck. To this end a *breaking dam* or *dambreak* simulation is performed. The initial condition of dambreak simulation is a reservoir of water, which is released when the simulation starts. Water will flow in the direction of a structure some distance away. Fig. 5.1 shows an image of the flow when it impacts with the structure. Note that open boundaries are not required for this type of simulation, since there is no interest in what happens after the impact has past.

Experimental research has shown that the impact depends on the shape of the ship's bow. Numerical simulation can be employed to study the effect of a different bow flare on the resulting impact with the structure on deck. Now, the bow is carefully modelled, an initial condition with a reservoir of water is defined and, again, the water is released when the simulation starts. Fig. 5.2 shows the water as it goes over the deck and impacts with the structure. In agreement with the previous line of reasoning, open boundaries are not required for this simulation either.

From further research it was found that there is an influence of the wave system around the ship and the relative surface elevation in front of the ship, on the resulting green water event and impact. The situation of a ship in waves requires an entirely different domain setup, because now wave propagation and the motion of the ship need to be simulated accurately as well, see Fig. 5.3. In theory, the boundaries can

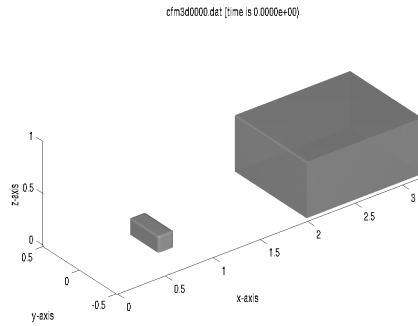


Figure 5.1: Dambreak against a structure in the path of the flow.

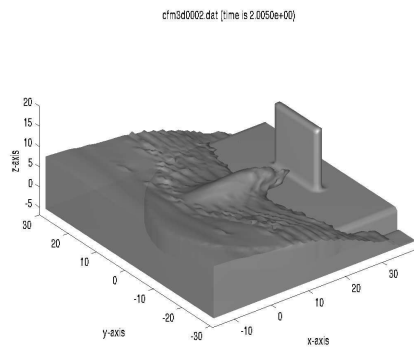


Figure 5.2: Dambreak against the bow of a ship.

remain closed, if the domain is chosen large enough to prevent spurious wave reflection from the boundaries. In practise, we have only limited time and memory available and we wish to dedicate these resources to the part of the ship where the impact will take place.

In simulations with waves around structures, the size of the domain without reflection is truncated, i.e. the boundary of a smaller domain is positioned close to the structure and boundary conditions are imposed *as if the structure was in the larger domain*. The boundary of the smaller domain is called an *artificial* or *open* boundary. In this chapter, boundary procedures for open boundaries are discussed.

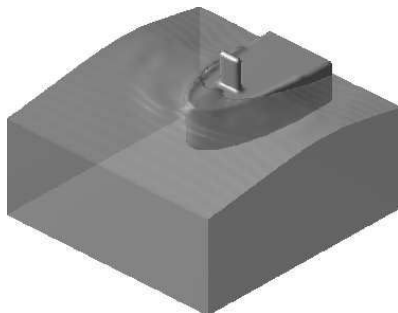


Figure 5.3: Green water on the deck of an FPSO in waves

5.1 Boundaries and boundary conditions

Fig. 5.4 shows a representation of a domain with boundary Γ , in which a smaller domain with artificial boundary \mathcal{B} has been defined. If Γ is infinitely far away from \mathcal{B} , the domain enclosed by Γ is called an *unbounded* domain. On \mathcal{B} , open boundary conditions are imposed for waves propagating from the larger domain to the smaller domain, and for waves originating from the smaller domain propagating toward the larger domain.

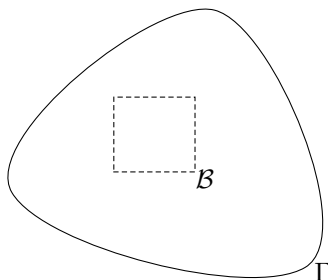


Figure 5.4: The natural boundary of a region is indicated by Γ . Within this region a domain with artificial boundary \mathcal{B} is created that is open to flow. In wave simulations boundary \mathcal{B} should be open to waves that go into the domain and waves that come out of the domain.

Waves from the larger domain toward the domain enclosed by \mathcal{B} are defined as *incoming* waves; waves in the reverse direction, toward the larger domain, are called *outgoing* waves. In the literature, boundary procedures for incoming waves are treated differently from procedures for outgoing waves. In this thesis, too, methods for wave generation at boundary \mathcal{B} are discussed separately from methods to prevent the reflection of outgoing waves. But we have to keep in mind that in offshore applications, boundaries are to be open for incoming waves and outgoing waves at the same time;

this is an important requirement for the design of a boundary procedure in our numerical method.

Before wave generation and spurious wave reflection are elaborated upon, the classic boundary conditions for open boundaries in numerical domains are discussed. We will also briefly show the way these boundary conditions are implemented in COMFLOW.

5.1.1 Dirichlet for the velocity

The Dirichlet condition specifies a certain value for a solution variable. If a velocity over a certain distance such as the water depth, is specified at the domain boundary, then, depending on the direction of the velocity, a fluid flux into or out of the domain is imposed. Note that solid wall boundary conditions are a subset of open boundary conditions. The prescribed velocity is then zero and there is no flux through the boundary.

Due to the fact that the solution variables are staggered over a cell, there are two configurations of the domain boundaries on either side of the domain. See Fig. 5.5. The domain boundaries are chosen to coincide with the position of the velocity in the cell. At one side of the domain, then, a halo cell or mirror cell is required to specify the velocity. Mirror cells are labeled with O. Mirror cells in the figures throughout this research are indicated by dashed lines. They are used to impose boundary conditions. The boundary itself is indicated by a bold solid line.

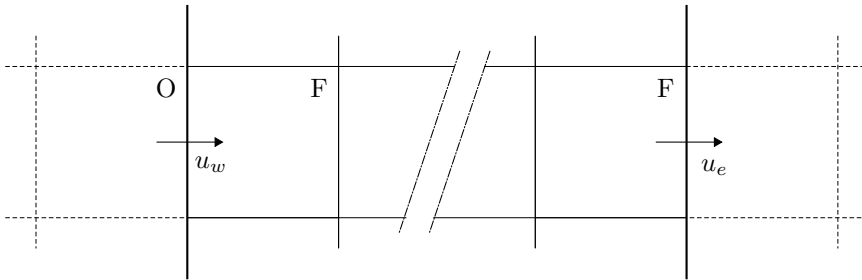


Figure 5.5: The boundary of the domain in horizontal direction. On the left of the domain a mirror cell is required to impose a Dirichlet condition for the velocity. These cells are labeled O. On the right of the domain the boundary coincides with the position of the horizontal velocity u_e in the F-cell.

5.1.2 Dirichlet for the pressure

Also pressures can be specified at the boundary of a domain. To specify a pressure, mirror cells on either side of the domain are required as shown in Fig. 5.6. A pressure

gradient over the domain boundary will generate an acceleration of the flow. From the acceleration a new velocity is determined and the velocity at the new time level is used, in turn, to calculate the fluid flux over boundary.

The momentum equation is discretized across the boundary. To obtain fluxes over the faces of the control volume that are outside the boundary, velocities need to be extrapolated beyond the boundary. Either constant or linear extrapolation from within the domain is used to obtain the velocities. They are indicated as u_w and u_e in Fig. 5.6.

In flow simulations the Dirichlet condition for the pressure is often used to prescribe a hydrostatic pressure variation at the boundary. The hydrostatic pressures are associated with a certain water level and this boundary condition will keep the average water level at the boundary fixed to a value.

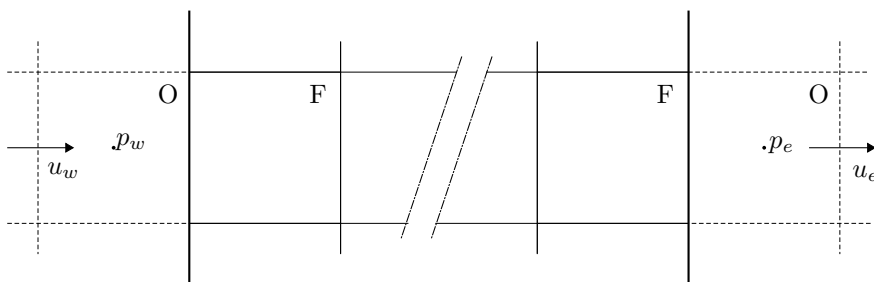


Figure 5.6: Mirror cells used to impose a Dirichlet condition for the pressure in horizontal direction. The velocities u_w and u_e are required to complete the discretization of the convective term across the boundary. They are obtained by constant or linear extrapolation.

5.1.3 Neumann for the pressure

Instead of specifying the pressure itself, we can specify the pressure gradient. Imposing the pressure gradient requires the same mirror cells as in Fig. 5.6, but in these cells an equation, which relates the pressure on the outside of the domain boundary to pressures on the inside, needs to be solved. The most common equation solved at the boundary is the following:

$$\frac{\partial p}{\partial n} = 0. \quad (5.1)$$

Eq. (5.1) allows for the effect of convection and diffusion over the boundary. To complete the stencil for the velocities at the boundary, the velocities u_w and u_e in Fig. 5.6 need to be extrapolated from the inside of the domain.

The classic Neumann condition for the pressure presented in this section is not well suited to prevent wave reflection, because it imposes zero acceleration. It works adequate in simulations of steady flow, but a boundary condition for waves needs to account for the time-varying wave dynamics near the boundary.

5.2 Wave generation

In experimental wave basins, waves are often generated by piston-type or flap-type wave makers. Piston-type wave boards generate waves by making a translational motion in normal direction to the wave board. They are mostly used in shallow water wave basins to generate long waves with a constant horizontal velocity (u) profile in vertical direction.

Short waves are generated by waves boards rotating around an underwater pivot point, see Fig. 5.7. The wave board is not a good approximation of the exponential horizontal velocity profile found in short waves and, therefore, spurious wave modes are generated in addition to the propagating waves the wave board means to create. The spurious wave modes include freely propagating waves, bound waves and evanescent waves, of which the amplitude decreases exponentially with greater distance from the wave board. Because of evanescent waves, a model-scale structure is always placed a certain distance away from the wave maker.

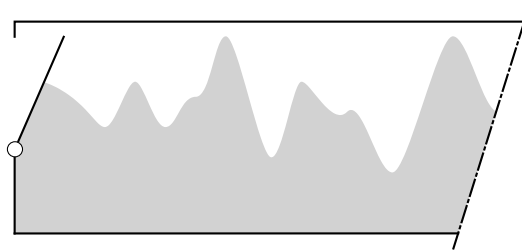


Figure 5.7: Wave basin where waves are generated with wave boards on the left-hand side of the basin.

The options to generate waves in experimental basins are limited, whereas the degrees of freedom in a numerical domain are far more numerous. In a numerical domain the ‘exact’ velocity profile, whether constant or exponential, can be imposed on the boundary by means of a Dirichlet condition for the velocity, see Fig. 5.8. The better the exact velocity profile is approximated, the fewer spurious wave modes are generated at the boundary. The velocities are found from either analytical wave theory or an external method, specifically designed for wave generation. Here, several methods for generating regular and irregular waves are examined.

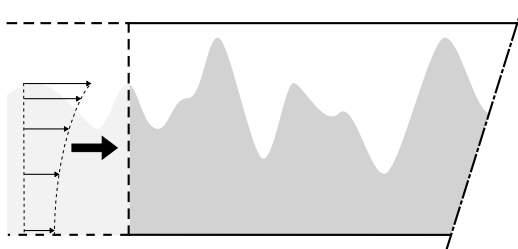


Figure 5.8: Numerical domain, in which waves are generated by means of the exponential velocity profile on the left-hand side of the domain.

5.2.1 Regular waves

Analytical theory is available for both small amplitude waves (with $ka \ll 1$) and steep, large amplitude waves. It is briefly summarized and results from steep regular wave simulations are presented, in which waves have been generated with velocities obtained from theory.

Linear potential theory

Consider the linearized Euler equations for irrotational flow with the following boundary conditions: (1) the impermeable bottom boundary condition, (2) the dynamic free surface boundary condition, stating that at the free surface, the pressure is equal to a reference pressure, and (3) the kinematic free surface boundary condition, which relates the change in position of the free surface to the vertical velocity. If, in addition, small amplitude waves with $\zeta_a \ll 1$ are assumed and the boundary conditions at the free surface are approximated by first order expansions around $z = 0$, we can derive an exact analytical solution to this system of equations in terms of the potential (see Appendix A):

$$\Phi = \frac{\zeta_a g}{\omega} \frac{\cosh k(h+z)}{\cosh kh} \sin(kx - \omega t).$$

Velocities are obtained from the potential by $\nabla\Phi = (u, v, w)^T$ and these velocities can be imposed on the boundary of the domain to generate regular waves. Linear theory is often used beyond its formal range of validity. The generation of steeper waves in numerical domains requires velocities from $z = 0$ to the actual position of the free surface at $z = \zeta$. In engineering, we have adopted two methods to determine these velocities.

The first method disregards the boundary at $z = 0$ and extends the exponential velocity profile toward $z = \zeta$. The second method, Wheeler stretching, was developed, because the velocities obtained from exponential extrapolation, were considered to overestimate the velocities in the actual wave crest. Wheeler stretching is a vertical

coordinate transformation, by means of which the velocity at $z = 0$ is positioned at $z = \zeta$ and a continuous profile between bottom and free surface is achieved.

Exponential velocity extrapolation and Wheeler stretching are compared when nonlinear stream function theory is discussed in the next section.

Non-linear stream function theory

Linear theory is only formally valid for small amplitude waves. In larger amplitude waves, the nonlinear terms in the system of equations become larger and can no longer be ignored. Linear potential theory uses a first order expansion of the solution variables around a mean value. Higher order expansions are possible: these are called Stokes' expansions. Stokes' expansions are formulated for deep water and mildly nonlinear waves.

The potential solution to the second order Stokes' expansion can still be derived by hand. For higher order expansions, numerical techniques are required. In the literature, Stokes' expansions go up to very high order [8]; practical implementations for use in a numerical method go up to fifth order [15].

Since Stokes' theory is limited to deep water and because higher order formulations become increasingly more difficult, Rienecker and Fenton [42] derived an approach that does not share these limitations. In Rienecker-Fenton theory for regular steep waves, the full solution is composed of a summation of N base stream function components with different unknown amplitudes:

$$\Psi(x, z) = B_0 z + \sum_{j=1}^N B_j \frac{\sinh jkz}{\cosh jkh} \cos jkx. \quad (5.2)$$

The summation of stream function components is substituted into the kinematic and dynamic free surface boundary condition at the actual free surface. In this way a system of nonlinear equations is obtained, where the primary unknowns are the amplitudes of the composing wave modes and the wave number they all share. The variables are solved for by Newton's method for a system of nonlinear equations. The Rienecker-Fenton solution is an analytical solution to the nonlinear system of equations, in which the only approximation is the truncation of the number of components, N .

Figure 5.9 compares velocity profiles for steep waves, in deep water and in shallow water. The velocity profiles have been determined with linear theory, Wheeler stretching, 5th order Stokes' theory and Rienecker-Fenton theory. There is a difference between Rienecker-Fenton and Stokes in shallow water. This was expected, because Stokes theory is limited to application in deep water. Since Stokes' theory is an expansion around the mean free surface, the approximation near the free surface is better than near the bottom. The comparison also shows that Wheeler stretching does not give better results; Wheeler stretching should not be used to impose steep regular waves. In this thesis, we have adopted Rienecker-Fenton theory to generate waves at the boundary.

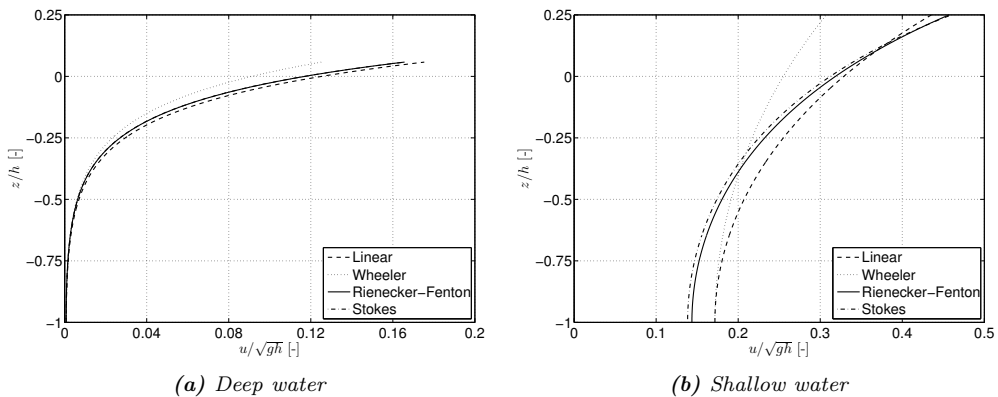


Figure 5.9: Velocity profile in a steep wave. The profiles have been determined with several analytical wave theories for regular waves.

Results

Rienecker-Fenton theory is used to generate steep regular waves in a domain. The water depth is $10m$ and the length of the domain L_D is chosen such, that reflection from the downstream boundary is prevented during the time of the simulation. It can be determined by considering the shallow water limit of the phase velocity $L_D = \sqrt{gh}t_{max}$.

Simulations are started from rest and the velocity signal at the boundary is ramped up over two wave periods to minimize initialization errors. Fig. 5.10 shows the free surface over two wave lengths from the boundary where waves with $H = 4m$ and $T = 6s$ are generated, after 24 periods have past. A stable solution over this distance has been obtained, i.e. that the wave height at a given position no longer changes in time. Different grid resolutions have been compared amongst each other and with theory. The surface elevation in the coarse grid simulations does not approximate the free surface well. With higher grid resolutions, the numerical solutions approach the Rienecker-Fenton solution, but the difference remains substantial, especially near the wave troughs. The main reason for the difference is thought to be the vertical grid resolution: in wave troughs almost the same fluid flux as in a wave crest, is represented by significantly less grid cells.

In comparing the horizontal velocity profiles two wave lengths away from the boundary (Fig. 5.11), we find that the profile is quite different from the analytical profile, both at the bottom and near the free surface. The difference is not caused by the inflow, because for all grid resolutions the velocities at the inflow are very near to the theory, as they should be.

At the free surface the convective terms of the momentum equation cannot be resolved entirely. It shows that the extrapolation performed on the velocities to close the

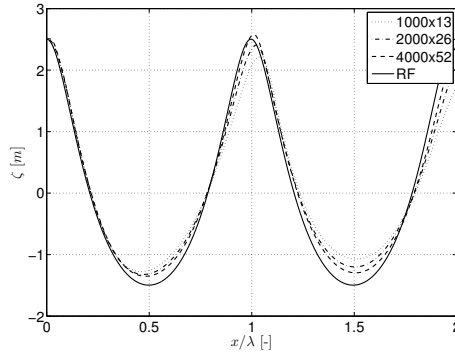


Figure 5.10: Free surface over two wave lengths at $t = 144s$. The free surface in numerical simulations with different grid resolution is compared to the Rienecker-Fenton solution.

system of equations, is not perfect. Alternatives for the extrapolation, however, are not readily available, as has been described in the previous chapter. The extrapolation error becomes smaller when the vertical resolution near the free surface is increased.

The difference between theory and the numerical results near the bottom was unexpected. It was thought that differences in the velocity profile would become apparent near the free surface, because the larger velocity gradients are found especially near the free surface. From Fig. 5.11 it seems that for higher grid resolutions, the velocity profile near the free surface are approximated quite well, but near the bottom the differences are still significant. This requires further research.

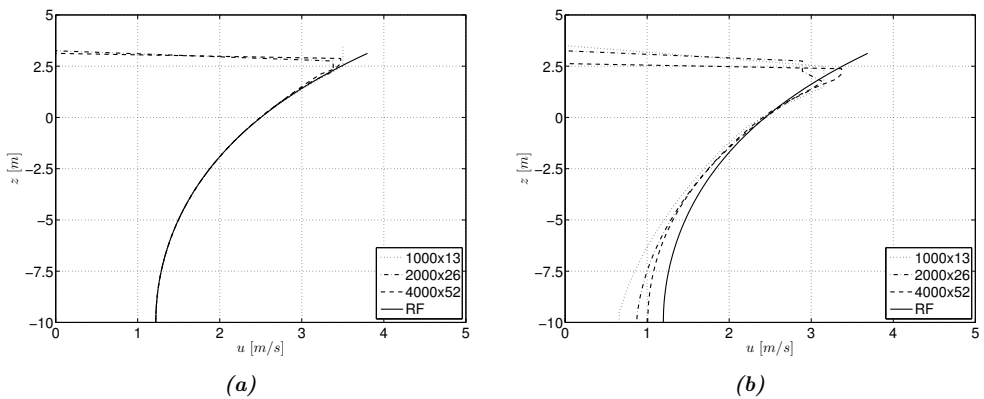


Figure 5.11: Horizontal velocity profile near the inflow in (a). In (b), the velocity profile two wave lengths away from the boundary.

5.2.2 Irregular waves

Analytical theory for steep irregular waves is not available. To generate steep waves, wave kinematics at the boundary are extracted from an external non-linear potential method, which has been specifically designed for the simulation of wave propagation over larger distances. When a specific sea state, of which only the surface elevation at a single position has been recorded, needs to be simulated, we use linear potential theory.

Linear potential theory

A registration of an irregular surface elevation can be decomposed into its Fourier components. The amplitudes and phases are used to determine the potential solution for each individual component and the total potential is obtained by summation of the potential's components:

$$\Phi = \sum_i \phi_i, \quad (5.3)$$

in which vector ϕ is the Fourier transform of Φ .

Linear theory, again, is only formally valid for waves with $ka_i \ll 1$. In steeper waves, the non-linear interaction between components is not accounted for and the kinematics obtained from linear theory will not resemble the actual physics. In the section containing the results of steep irregular wave simulations, waves generated with linear theory are compared with the non-linear solution of an external potential method.

External non-linear potential method

The numerical method described in Westhuis [55] is a non-linear potential flow model, implemented as a field method for a free surface conforming finite element mesh (FEM). The primary unknowns are the potential values defined at the nodes of the mesh and the velocities required in the kinematic free surface boundary condition are resolved by finite difference (FD) of the potential values near the free surface. In this thesis, we will refer to this method as FDFEM.

The FDFEM in [55] is a second order method without significant wave energy dissipation. In addition, the free surface boundary condition is resolved accurately, because the surface elevation is clearly defined by the position of the uppermost grid nodes. For this reason, FDFEM is better suited for wave propagation over large distances than COMFLOW. In very steep waves, FDFEM can become unstable as a result of *saw-tooth instabilities* also found in [34]. Before the instabilities occur, however, it is highly accurate. This has been confirmed by validation with experimental results in [55].

Wave kinematics are obtained from FDFEM by finite difference of the potential values. After interpolation in time and space, the kinematics are used to generate waves in our numerical method.

FDfEM Results

Irregular waves are generated at the boundary with kinematics from the external FDFEM. The FDFEM simulation is performed on a very long domain, in which reflection during the time of the simulation cannot occur. The water depth is $10m$ and waves from a JONSWAP spectrum with $H_s = 4m$ and $T_p = 7s$ are created by a flap-type wave maker that pivots around a point at $z = -9m$. Ten elements in vertical direction are used with a stretch factor of 10%. In horizontal direction the grid distance is equal to $1m$. Wave kinematics are obtained from a position $200m$ away from the wave board and used as input for our numerical method.

After 14 significant peak periods the surface elevation over a length of $200m$ is compared between COMFLOW and FDFEM. It is depicted in Fig. 5.12. At this moment in time, the signal consists of low frequency components and higher frequency components. Three grid resolutions were used and the difference between methods becomes smaller when the grid resolution is increased. The high frequency components are not represented well on the coarsest grid, but the difference between our numerical method and FDFEM becomes smaller when the grid resolution is increased.

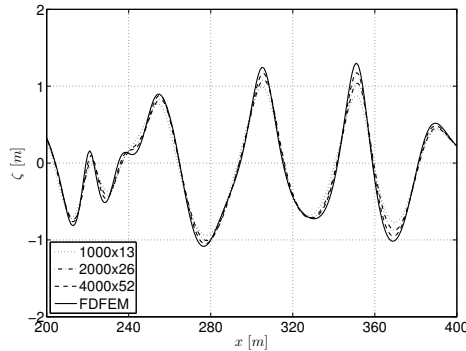


Figure 5.12: Free surface over two wave lengths at $t = 144s$. The free surface in numerical simulations with different grid resolution is compared with the FDFEM solution. Kinematics at the inflow boundary of COMFLOW obtained from the FDFEM solution.

Fig. 5.13 shows the horizontal velocity profiles at $t = 14T_p$ near the inflow and $200m$ away from the inflow. Near the inflow the velocity profiles are the same as the one obtained from FDFEM, although there is a slight difference for the coarsest grid. Further away from the boundary, the differences are larger. The finer grid gives better results. Almost the same conclusion as in the regular wave tests applies here: the difference between COMFLOW and FDFEM near the free surface becomes negligible for the highest resolution. And for this resolution, there still is quite a difference between the velocities near the bottom.

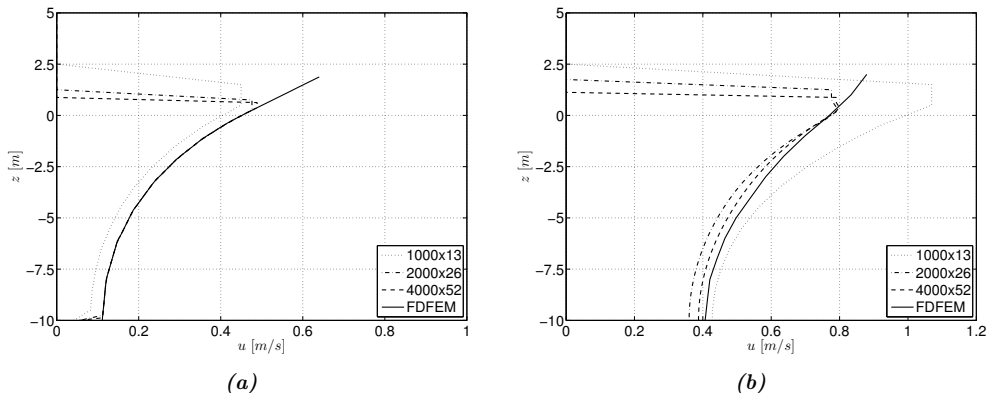


Figure 5.13: Horizontal velocity profile near the inflow in (a). In (b), the velocity profile two wave lengths away from the boundary. Kinematics at the inflow boundary of COMFLOW obtained from the FDFEM solution.

Linear results

A simulation with waves generated by kinematics from linear theory (continuing the exponential profile of the velocities in vertical direction) is performed and compared to a FDFEM simulation. At $x = 200m$, a Fourier decomposition of the surface elevation is used to obtain the amplitudes and phases of the individual wave components. From the components, we determine the velocities at the boundary of a COMFLOW domain.

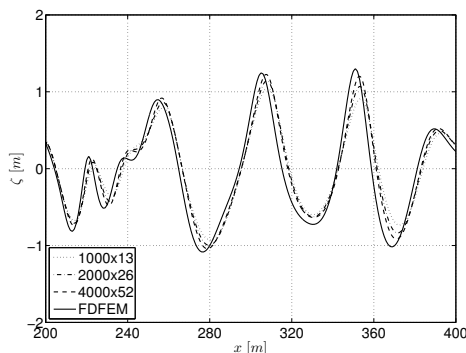


Figure 5.14: Free surface over two wave lengths at $t = 144s$. The free surface in numerical simulations with different grid resolution is compared to the FDFEM solution. Kinematics at the inflow boundary of COMFLOW obtained from linear potential theory.

After $14T_p$, when there are both long and short components in the domain, the surface elevation over a distance $200 \leq x \leq 400$ is compared between generation methods. Fig. 5.14 shows that there is a clear difference between waves generated with linear theory, and those generated by the actual velocities from FDFEM. The difference is mostly caused by the wave kinematics at the boundary, see Fig. 5.15.

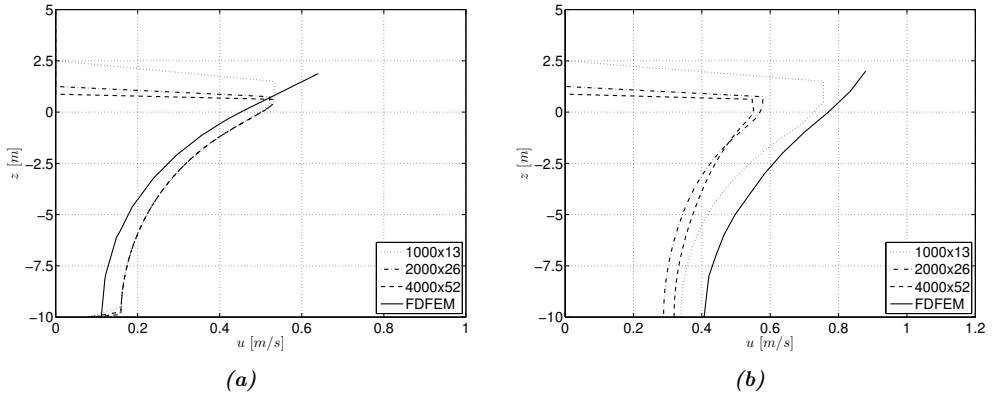


Figure 5.15: Horizontal velocity profile near the inflow in (a). In (b), the velocity profile two wave lengths away from the boundary. Kinematics at the inflow boundary of COMFLOW obtained from linear potential theory.

5.2.3 Discussion

Regular waves have been generated with linear potential theory and non-linear stream function theory. Regular waves should always be generated with a non-linear theory, because it is more accurate and there are no disadvantages to using the Rienecker-Fenton solution.

When the numerical simulation of steep regular waves is compared with analytical theory, we find clear differences. The differences become smaller in higher grid resolutions, but even for the finest grid a slight deviation remains.

We have generated irregular waves with a Fourier decomposition of the surface elevation from FDFEM, in combination with linear potential theory. The surface elevation in this simulation has been compared with the surface elevation from FDFEM. There were differences, which did not improve with higher grid resolutions. These differences are attributed to the incorrect inflow: linear potential theory yields different kinematics than full non-linear simulation.

Linear theory for irregular wave generation can be used when we wish to simulate a sea state to obtain statistics of, for instance, motions or impacts. However, to simulate an actual, deterministic event as it occurred in an experimental wave basin,

we need to generate waves with the kinematics of an external non-linear method to be able to compare results.

5.3 Preventing reflection

In experimental basins, wave reflection is reduced by either beaches, or by Active Reflection Compensation (ARC). Beaches induce wave breaking and dissipation of wave energy, see Fig. 5.16. Dissipation effectively prevents reflection of short wave components, but longer wave components are dissipated to a limited extent. Long wave components run up on the beach and are sent back with almost full reflection.

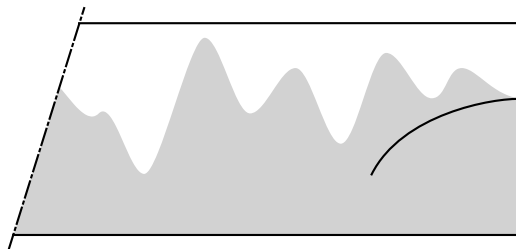


Figure 5.16: *In experimental wave basins, the reflection of waves is prevented by a beach that induces wave breaking and the resulting wave energy dissipation*

ARC is installed on wave boards, see Fig. 5.17. It is a control system to prevent reflection by means of the wave maker motion, in response to surface elevation measurements or measurements of the total force on the wave board. Only limited accuracy can be obtained with active reflection compensation for three main reasons. Firstly, the surface elevation measurements are affected by the motion of wave board. A second, related reason is that also evanescent wave modes near the board disturb the accurate measurement of outgoing waves, although they can be partly compensated for. The third and final reason is that the motion of the wave board is limited: long waves require a very long stroke, which is not available.

Modelled beach geometries and ARC can be used in numerical domains as well, but better performance in terms of reflection can be obtained with other methods, which will be discussed in this section: (1) dissipation zones, (2) kinematics from external methods and (3) non-reflection boundary conditions.

5.3.1 Dissipation zones

Dissipation zones reduce wave energy within the domain before they reach the downstream boundary. They are found under many names, being called numerical beaches, dissipating layers, sponge layers and absorbing layers, among other names. [29] gives

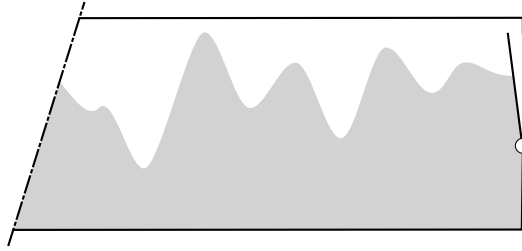


Figure 5.17: Active reflection compensation is installed on the wave boards in an experimental wave basin. The surface elevation or total force on the wave board is measured to identify outgoing waves and reflection is prevented by the subsequent motion of the board.

an account of several dissipation zones. Here, we will specifically mention pressure damping.

In a pressure damping zone, an additional pressure, proportional to the vertical velocity at the free surface, is defined:

$$p_s = \alpha(x) w(x, t)|_{\zeta}, \quad (5.4)$$

in which α represents a coefficient that is gradually increased to reduce reflection from inside the pressure damping zone itself.

Analogously to a physical beach in the basin, a pressure damping zone is more efficient for short wave components than for long wave components, because the dissipation is proportional to the vertical velocity. The vertical velocities in long waves are small and, therefore, long dissipation zones are required to sufficiently prevent reflection.

An efficient dissipation zone is the Perfectly Matched Layer (PML), introduced by Berenger [2]. Whereas pressure damping can easily be incorporated into the pressure boundary condition at the free surface, the PML requires an additional set of equations to be solved. These equations are derived as follows: harmonic solutions are analytically continued to infinity. The analytical solutions are formulated in complex space, where harmonically varying solutions become exponentially decaying solutions. Then a coordinate transformation from complex space to real coordinates is performed. Part of the domain, in real coordinates, will then feature exponentially decaying wave solutions. And, finally, the domain can be truncated at the location where the amplitude of the propagating wave modes has decayed to an acceptable level.

Regardless of the efficiency, a dissipation zone requires a substantial part of the domain to dissipate wave energy. Consequently, the domain is larger than the direct surroundings of the structure, where the main interest lies. And the larger the domain, the more computation time and memory are required.

Finally, we would like to note that it does not seem likely that dissipation zones for outgoing waves can be combined with incoming waves going through the dissipating

region. This is a serious impediment for the use of dissipation zones on all sides of domains for offshore applications.

5.3.2 Matching to external solutions

We have used wave kinematics from external methods (FDFEM) to generate waves on the upstream side of the domain. On the downstream side, it is possible, in theory, to use those kinematics for wave absorption. If the differences between the kinematics in the external method and the internal method are small, then a local boundary condition by means of imposed kinematics has been devised. It will be called a matching procedure to exterior solutions.

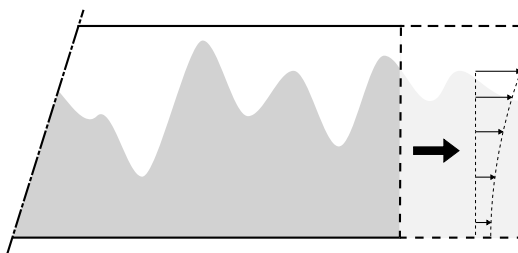


Figure 5.18: *When wave kinematics are prescribed at the downstream end of the domain, a local boundary condition in terms of velocities is obtained. This is called a matching procedure to external solutions.*

However, COMFLOW will not be used to study wave propagation alone, but to obtain results for impacting waves against structures. A structure inside the domain will change the surrounding wave field. According to linear theory, there are three, separate contributions to the total wave field near a structure: undisturbed incoming waves, diffracted waves and radiated waves, originating from the motion of the structure.

In Wellens et al. [53], a procedure was suggested to incorporate the effects of diffraction and radiation into the boundary condition along the extremities of the domain. A linear, frequency domain boundary element method was used to account for both incoming and outgoing waves in the velocities imposed at the boundary during the simulation. And also the initial condition was a developed solution obtained from BEM. As expected, the procedure worked well for mildly steep waves. For steeper waves the procedure is less accurate. This is caused by the difference in resolved phase velocity between linear theory and the actual non-linear simulation of steep waves.

To give an indication of the reflection error, a wave simulation was performed without a geometry present. The period T is 10.0s, the wave height $H = 3.0m$ and the water depth $h = 10.5m$ in a domain of 100.0m long. Fig. 5.19a shows the surface elevation in the middle of the domain when linear potential theory is used to impose inflow and outflow kinematics. As a comparison, the same simulation was performed with Rienecker-Fenton and the results are shown in Fig. 5.19b.

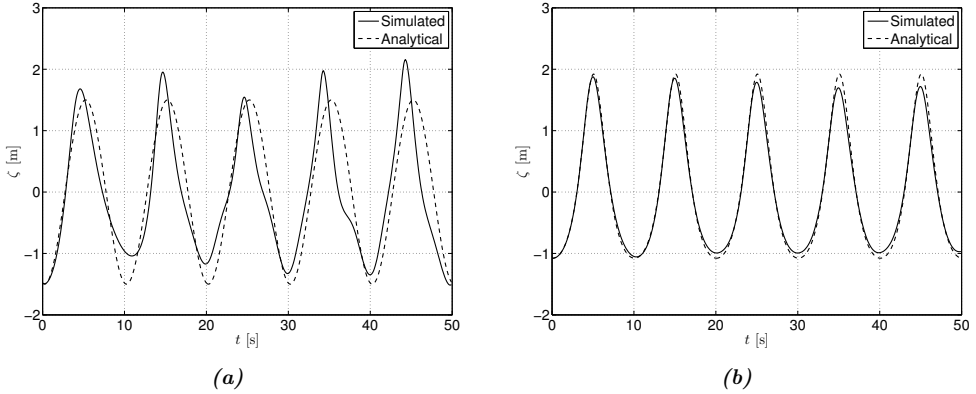


Figure 5.19: Surface elevation in the middle of a 100.0m domain when linear kinematics at inflow and outflow are used in (a). In (b) the surface elevation for the same simulation is shown when Rienecker-Fenton kinematics are used at the boundaries.

The simulated surface elevation in Fig. 5.19a, for which linear kinematics were used at the boundary, suffers greatly from spurious reflection. It looks better when non-linear kinematics are used, although the graph shows some effect of interference from the boundary. These results seem to lead to the conclusion that non-linear kinematics should be used at the boundary of a computational domain. Unfortunately, non-linear analytic theory that accounts for diffraction and radiation as a result of a structure in the domain does not exist. Non-linear numerical time domain methods to account for these effects [43] are just as time intensive as COMFLOW and suffer from the same need to impose boundary conditions. As a result, the investigation of matching procedures to external solutions was discontinued.

5.3.3 Non-reflecting boundary conditions

There is a vast amount of literature on the subject of non-reflecting boundary conditions (NRBCs), but not many have been specifically designed for use in non-linear methods to simulate extreme free surface wave impact events. NRBCs found in literature have been predominantly combined with simple, linear partial differential equations (PDEs) from a wide range of application areas, such as optics, meteorology, oceanography and more.

Tsynkov [47] gives a very thorough account of several complicated NRBCs for simple PDEs. In this discussion, we will only highlight what is considered to be important for the design of an NRBC in COMFLOW.

Non-reflecting boundary conditions have many names. The ones most often encountered are: artificial boundary conditions, radiation conditions and absorbing boundary

conditions. Although ‘non-reflecting boundary condition’ or ‘weakly reflecting boundary condition’ is, in our opinion, a better description of the functionality, the term ‘absorbing boundary condition’ or ABC is found more often and will be adhered to from here on.

The derivation of an exact ABC, at least in linear circumstances, goes along these lines: (1) the system of equations is transformed to the frequency domain, (2) in the frequency domain we solve for the outgoing wave modes, (3) the solution for outgoing wave modes is transformed back to the time domain to obtain an ABC operator. The resulting operator is global in time and global in space.

The global nature of the exact ABC operator is undesirable, since its discrete implementation requires storage of all previous time steps, and requires processing of all spatial grid points at every time. Different authors have therefore approximated the exact ABC in different ways.

For steady problems the Dirichlet-to-Neumann map (DtN) is a well known formulation of an exact ABC [21]. The boundary condition has the following form:

$$\frac{\partial u}{\partial n} = -M u, \quad (5.5)$$

in which u is the solution variable in the wave equation under consideration and M is the DtN map. The name DtN originates from this boundary condition, since it relates a Dirichlet datum to a Neumann datum in normal direction to the boundary.

The exact DtN is often truncated in the number of harmonics to save computation time. Of course, the DtN is then no longer exact. Keller and Givoli [30] have proposed an implementation for a finite element formulation in a circular domain, which requires limited truncation and only marginally adds to the overall computation time. This is an important requirement of an ABC: it should yield accurate absorption of outgoing waves with a reflection coefficient of only a few percent for a range of wave numbers. But, at the same time, it should not lead to a substantial increase of the computational effort.

Givoli and Patlashenko [20] have suggested another approach: they consider a localized ABC, which may be of low order, but which is still highly accurate for a range of harmonics. The accuracy is obtained by an optimization of the coefficients in the local ABC; the optimal coefficients are those, which approximate the exact DtN to the greatest extent.

For time dependent problems, Grote and Keller [22] introduced an exact ABC that is local in time, but global in space. They derive a formulation featuring higher derivatives in normal direction to the boundary. Because higher derivatives may cause difficulties in numerical implementations, it is shown for circular (spherical) shaped domains how to reformulate the boundary condition to an expression that features only first-order derivatives along the boundary.

A general observation with respect to exact, global boundary conditions is that they cannot be implemented without approximating the expression in time, in space and in the number of harmonics that is considered. For certain domain shapes, either

circular, spherical or ellipsoidal, some of the global nature of the exact ABC can be retained. These ABC formulations cannot be generalized to Cartesian coordinates.

Another observation is that the exact ABCs never consider both outgoing and incoming waves; the formulations do not seem to be suited for this extension. Open boundaries for incoming and outgoing waves are a major design requirement for an ABC in offshore applications. And our numerical method has been formulated using Cartesian coordinates by design. Exact absorbing boundary conditions will therefore not be considered for use in COMFLOW.

5.4 Discussion

In this chapter, boundary conditions for wave generation have been discussed, as well as methods for reflection prevention. Adequate methods for wave generation have been found: we will use Rienecker-Fenton theory to simulate regular waves and an external method, FDFEM, in simulations with irregular waves.

Additionally, several methods for preventing reflection have been discussed. Dissipation zones are most probably not suited for offshore applications, because they cannot dissipate outgoing waves and leave incoming waves unaffected at the same time. When only outgoing waves need to be considered, it can be said that they perform well for short waves. However, the dissipation of long waves requires dissipation zones of several (long) wave lengths in size. In 3D, this would yield significant amounts of computer resources.

We prefer to devote these resources to the accuracy of the wave impact event itself. We have therefore discussed a matching procedure with a local velocity boundary condition, in which the velocities at the inflow boundary and at the outflow boundary account for the incoming wave. It was clear that linear potential theory should not be used in case of steep waves, because the phase velocity in linear theory does not match the non-linear solution. Better results were obtained with non-linear potential theory, although some reflection could be observed because the discrete solution in the COMFLOW-domain does not exactly match the analytical solution. This method of prescribing velocities at the boundaries does not account for the structure inside the domain. We can expect that disturbances from the structure will fully reflect at the boundary with this method.

Multiple absorbing boundary conditions have been considered, but none have been found that can readily be incorporated into our numerical method. From this discussion, we have been able to formulate a set of requirements for the design of an ABC for use in COMFLOW:

1. The ABC needs to be accurate and bring back reflection from the boundaries to an acceptable level.
2. The boundaries where the ABC is defined, are to be truly open boundaries, i.e. transparent to incoming and outgoing waves at the same time.
3. The computational resources to prevent reflection should be marginal compared to the computational effort to determine the solution itself. Global ABCs do

not satisfy this requirement and we will only consider ABCs, that are local in time and local in space, from here on.

4. It should be possible to position the boundary close to the structure, not further away than a length comparable to the size of the structure.
5. The ABC needs to be formulated on a rectangular, Cartesian grid domain.
6. The stability of the system of equations inside the domain should not be affected by the ABC.

Chapter 6

Generating absorbing boundary condition

In this chapter we discuss a local absorbing boundary condition for incorporation into our numerical method. The offshore applications demand that the boundaries are open to incoming and outgoing waves. Consequently, the boundary condition requires the combined functionality of wave generation and wave absorption, within the constraint of an efficient algorithm, that does not disproportionately increase the computational effort. *A fortiori*, the use of a well-designed boundary condition should rather reduce than increase the computational effort, because without significant spurious reflection, the boundaries can be positioned closer to the structure inside the domain.

In coastal regions, only shallow water waves need to be considered. The phase velocity of wave components in shallow water is only marginally different from the shallow water limit \sqrt{gh} . Wave absorbing boundary conditions for the numerical simulation of waves in coastal applications, need only consider the direction of waves reaching the boundary. In deep water, however, both the angle with respect to the boundary and the phase velocity of wave components (dispersion) near the boundary are relevant for the design of a boundary condition.

6.1 Literature overview

Literature concerning boundary conditions for the numerical simulation of free surface waves in three dimensions, in which direction and dispersion are both accounted for at the same time, has not been found. A great number of authors consider and devise boundary conditions for the multi-dimensional wave equation, often only in two dimensions and in the xy -plane. Far fewer ever mention dispersion and hardly any have discussed dispersion in boundary conditions for the numerical simulation of free surface waves in the xz -plane.

For a detailed report of (mostly) local absorbing boundary conditions, refer to the review article of Givoli [17]. Here we will give a brief review of the relevant literature about local absorbing boundary conditions and discuss three aspects in particular: (1) directionality, (2) dispersion and (3) incoming and outgoing waves. The direction of waves is important in short-crested wave simulations. We will discuss dispersion for long-crested waves in deep water. And, finally, incoming and outgoing waves are considered, accounts of which have been mostly encountered when ABCs were devised by means of characteristic variables.

6.1.1 Short-crested waves

The starting point for the derivation of local absorbing boundary conditions is often the planar wave equation given by:

$$\left(\frac{\partial^2}{\partial t^2} - c^2 \nabla^2 \right) \Phi = 0. \quad (6.1)$$

Fourier transform of the wave equation, yields the dispersion relation, which relates frequency to wave number:

$$\omega^2 - c^2 (k_x^2 + k_y^2) = 0. \quad (6.2)$$

If the dispersion relation is solved for k_x , the following is obtained:

$$k_x = \pm \frac{\omega}{c} \sqrt{1 - s}, \quad (6.3)$$

in which s equals $k_y^2 c^2 / \omega^2$.

Inverse Fourier transform of this expression gives the exact boundary condition operator, which is nonlocal in time and in space, due to the $\sqrt{1 - s}$ in Eq. (6.3). Non-local absorbing boundary conditions are considered impractical in numerical implementations. Therefore, Engquist and Majda [13] suggested a series approximation of the term $\sqrt{1 - s}$ to obtain increasingly better performing local absorbing boundary conditions.

The zeroth order approximation of $\sqrt{1 - s}$ is $1 + \mathcal{O}(s)$. The inverse Fourier transform of $k_x \phi$, in which ϕ is the Fourier transform of Φ , results in the following operator:

$$\left(\frac{\partial}{\partial t} + c \frac{\partial}{\partial x} \right) \Phi = 0. \quad (6.4)$$

Eq. (6.4) is a boundary condition, which is exactly absorbing for outgoing waves with velocity c , propagating in the positive direction perpendicular to the boundary at $y = y_{max}$. In engineering it is known as the Sommerfeld condition [46]. It performs less well for waves under an angle with the boundary.

A better boundary condition for waves under an angle with the boundary, is the operator that results from a first-order approximation of the square root in the dispersion relation. The first-order approximation is expanded below:

$$\sqrt{1-s} \simeq 1 - \frac{s}{2} + \mathcal{O}(s^2). \quad (6.5)$$

When the approximation is substituted into the dispersion relation, then inverse Fourier transform of the dispersion relation yields the following operator:

$$\left(c \frac{\partial^2}{\partial t \partial x} - \frac{\partial^2}{\partial t^2} + \frac{c^2}{2} \frac{\partial^2}{\partial y^2} \right) \Phi = 0. \quad (6.6)$$

From Eq. (6.6) we find that higher order approximations of the dispersion relation give higher derivatives in the absorbing boundary condition operator. By means of higher derivatives in the ABC, waves with larger incoming angles to the boundary are accurately absorbed.

Higdon [26] generalized this theory. He shows that the Engquist and Majda boundary condition is a less efficient subset of the following product of operators:

$$\prod_{j=1}^J \left(\frac{\partial}{\partial t} + c_j \frac{\partial}{\partial x} \right) \Phi = 0. \quad (6.7)$$

In fact, in his article he proves the theorem that absorbing boundary conditions are either 1) of this form, 2) unstable or 3) suboptimal. The reflection coefficient associated with the Higdon boundary condition, shares a similar form:

$$R = \prod_{j=1}^J \left(\frac{c_j - c_e}{c_j + c_e} \right). \quad (6.8)$$

Because the term in between parentheses in Eq. (6.8) is always smaller than one, it is clear that the reflection coefficient R becomes smaller as the order of the ABC increases. The order of the boundary condition, in this sense, reflects the number of products J used to construct the operator. Increasing the order of the boundary condition reduces reflection considerably. For instance, when the boundary condition with $J = 1$ gives 10% reflection for a certain wave mode, it will give 1% reflection with $J = 2$.

Higher order ABCs feature higher derivatives. As the order of the ABC increases, it becomes increasingly difficult to implement the numerical equivalent of the higher derivatives at the boundary. Givoli [18] reports that Higdon operators beyond order three are rarely found in the literature.

However, ABCs of even infinite order can theoretically be constructed, since Collino and Joly [9] introduced auxiliary variables to avoid the use of higher derivatives. Instead of N^{th} derivatives, then a system of $N + 1$ additional equations is solved at the boundary.

Collino's idea has found widespread interest, see the review article concerning high order local boundary conditions by Givoli [18]. Auxiliary variables have been used in N^{th} order ABCs derived by Grote and Keller [23], Givoli and Neta [19] and Hagstrom and Warburton [24], among others. The Hagstrom-Warburton formulation of the auxiliary system of recursive equations is:

$$\left(a_0 \frac{\partial}{\partial t} + c \frac{\partial}{\partial x}\right) \Phi = a_0 \frac{\partial}{\partial t} \xi_1 \quad (6.9)$$

$$\left(a_j \frac{\partial}{\partial t} + c \frac{\partial}{\partial x}\right) \xi_j = \left(a_j \frac{\partial}{\partial t} + c \frac{\partial}{\partial x}\right) \xi_{j+1} \quad \text{for } j = 1, 2, \dots, N \quad (6.10)$$

$$\xi_{N+1} = 0 \quad (6.11)$$

The set of equations features none higher than first derivatives. Still, the implementation of first derivatives becomes a problem in the corners of rectangular domains. There, special corner conditions have to be formulated. The state of the art with respect to ABCs is described in a recent article by Hagstrom et al. [25].

6.1.2 Dispersive waves

There are two ways to account for dispersion at the boundary: one is to use a low order boundary condition and combine it with with an estimator for the *actual* phase velocity at the boundary; the second is to use higher order boundary conditions. As an example of the former, we mention Orlanski [39]. He suggests the use of the Sommerfeld condition, with a dynamic approximation of the phase velocity, obtained from the solution itself:

$$c = - \frac{\partial \Phi / \partial t}{\partial \Phi / \partial x}. \quad (6.12)$$

Fig. 6.1 shows a representation of the phase velocity, when the Orlanski boundary condition is applied to an irregular wave signal conforming to a JONSWAP spectrum with $T_p = 15\text{s}$. It shows rather large discontinuities in the resolved value for c , coinciding with the times where the denominator in (6.12) becomes zero, which can and will lead to an unstable simulation. The only way this ABC can be applied, is when a low-pass filter is applied in the dynamic estimator. Of course, filtering will lead to a reduced accuracy of the ABC and more spurious reflection.

Dispersion of free surface waves in the xz -plane has not been an explicit subject in much of the literature regarding high order absorbing boundary conditions. Most authors [19, 25, 26] show that their approach to ABCs transcends to dispersive media by means of the Klein-Gordon equation in the xy -plane:

$$\left(\frac{\partial^2}{\partial t^2} - c^2 \nabla^2 + f^2\right) \Phi = 0, \quad (6.13)$$

in which f is a dispersion parameter used to model the earth's rotation for application in meteorology or oceanography. With the dispersion parameter, the ABC changes only slightly.

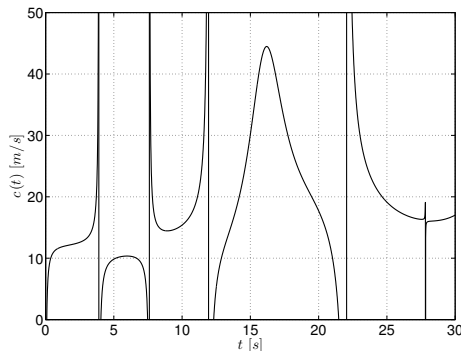


Figure 6.1: The resolved phase velocity c as a function of time, when the Orlanski boundary condition is used. The discontinuities result from the zero crossings of the denominator in the equation for c . The irregular wave signal was generated with a JONSWAP spectrum with $T_p = 15s$.

Dispersion is not a material property of water, but results primarily from the presence of the free surface. We know of only one article by Dgaygui and Joly [10], that discusses absorbing boundary conditions for the simulation of free surface waves in the xz -plane. Herein, an exact, non-local ABC-operator is derived. Subsequently, the exact operator is simplified by means of rational approximations to yield an ABC, which is local in space and local in time. Finally, numerical results are presented for simulations of long waves with a zeroth order and a first order boundary condition. With the latter ABC, the reflection was generally small; exact figures have not been mentioned.

6.1.3 Incoming and outgoing waves

In section 6.1.1, local boundary conditions for the planar wave equation were derived from an exact non-local boundary condition derived by Engquist and Majda [13]. A different way to derive boundary conditions is by means of the method of characteristics discussed by Blayo and Debreu [3]. Here, the method of characteristics is applied to the wave equation.

Consider again wave equation (6.1), but now in one dimension in the direction normal to the boundary:

$$\left(\frac{\partial^2}{\partial t^2} - c^2 \frac{\partial^2}{\partial n^2} \right) \Phi = 0, \quad (6.14)$$

in which n is the outward normal direction.

Eq. (6.14) can be factorized as follows:

$$\left(\frac{\partial}{\partial t} - c \frac{\partial}{\partial n} \right) \left[\left(\frac{\partial}{\partial t} + c \frac{\partial}{\partial n} \right) \Phi \right] = 0. \quad (6.15)$$

The term $\left(\frac{\partial}{\partial t} + c\frac{\partial}{\partial n}\right)\Phi$ in Eq. (6.15) is constant along lines $dn/dt = -c$. We call this term the incoming characteristic variable.

A boundary condition for wave equation (6.14) is obtained by assigning a value to the incoming characteristic variable. When no waves enter the computational domain through the boundary, the boundary condition becomes:

$$\left(\frac{\partial}{\partial t} + c\frac{\partial}{\partial n}\right)\Phi = 0.$$

It is no coincidence that the boundary condition obtained in this way is equal to the Sommerfeld equation (6.4) in section 6.1.1.

It is customary in the literature concerning ABCs to set the right-hand side in (6.4) equal to zero, but it is not required. When the incoming characteristic receives a non-zero time-dependent right-hand side value, we are sending in waves over the boundary, while outgoing waves may leave the computational domain unaffected. In this way, a - what we will call - Generating Absorbing Boundary Condition (GABC) is obtained.

According to Carpenter [7] and Perkins et al. [40], the Sommerfeld equation with non-zero right-hand side value should be formulated as follows:

$$\left(\frac{\partial}{\partial t} + c\frac{\partial}{\partial n}\right)\Phi = \left(\frac{\partial}{\partial t} + c\frac{\partial}{\partial n}\right)\Phi^{in}. \quad (6.16)$$

In Eq. (6.16), the right-hand side value consists of the same characteristic combination of operators as on the left-hand side, but now they are applied to the known function Φ^{in} .

The method of characteristics is also employed by Verboom and Slob [50] and Van Dongeren and Svendsen [48]. These authors derive boundary conditions for the Non-linear Shallow Water equations (NSW). The NSW are composed of a system of equations that cannot be combined into a single equation such as wave equation (6.1). Characteristic equations are then obtained by diagonalizing the system with the matrix of eigenvectors. The boundary condition for the NSW by Van Dongeren and Svendsen [48] is demonstrated to give less than two percent reflection for long-crested waves, irrespective of the wave direction in the computational domain.

6.2 Motivation

The discussion in the previous chapter resulted in a set of requirements for a boundary procedure to be used in combination with our numerical method. Global boundary procedures have been considered, zonal procedures seemed promising, but the conclusion was that for reasons of efficiency, local methods would be more suitable.

Literature regarding local absorbing boundary conditions has been studied. It turns out that absorbing boundary conditions of arbitrarily high order can be constructed and implemented at the boundary. Results obtained with this method are promising.

Yet, in formulating a decision which absorbing boundary condition will suffice for our method – and to which order – some concerns regarding these methods have to be expressed.

The high order ABCs have so far only been combined with very simple differential equations, such as the planar wave equation and the Klein-Gordon equation. The results obtained are for highly schematic wave scattering simulations, which have little practical relevance. With regard to practicality, we cite from the concluding remarks of Hagstrom et al. [25]:

“However, the way to achieving such a level of practicality [for application in engineering, PW] is still very long.”,

and

“[...] for applications in weather prediction and oceanography, the ABC must be turned into an ‘open boundary condition’ which allows not only free passage of waves from the computational domain Ω outside, but also passage into Ω of waves incoming from the exterior.”

and finally

”Extension to three dimensional geometry is also very important.”

With high esteem for the theoretical work performed in developing ABCs of arbitrary high order, we feel this is not the way to obtain practical and stable boundary conditions for the numerical method in this thesis. It is unclear if an N^{th} order boundary condition is really required. In practical simulations, five percent reflection for wave components within the frequency band where most of the wave energy resides in the spectrum, is an acceptable level of accuracy. We will consider low order ABCs first and improve from there.

Another important design requirement for an ABC in offshore applications is the two-way transparency to waves. The auxiliary variables required for high order boundary conditions, complicate matters with respect to incoming waves. Additionally, the extension to three dimensions is not only ‘important’, in Hagstrom’s words, but also necessary for application in COMFLOW. Apart from the feasibility of a 3D implementation of high order ABCs, also the computation time will become restrictive. In high order ABCs, an extra system of equations needs to be solved along the entire boundary and in 3D this additional system cannot be considered small compared to the total number of equations within the domain.

At present we do not see how to combine the high order boundary condition approach with a substantial number of our design requirements. In this research, therefore, we set out to develop a practical ABC for the benefit of physically relevant simulations of extreme wave-structure hydrodynamics. The ABC combines the work of Higdon, Dgaygui&Joli and Blayo&Debreu, with physical properties of waves that can be obtained from potential theory. The focus, at first, will be on dispersion in irregular long crested waves.

6.3 Derivation

In this section, we derive an absorbing boundary condition for long-crested, irregular, dispersive waves in any water depth with normal incidence to the boundary.

In shallow water, or - more correct - in the shallow water limit for $kh \rightarrow 0$, there is no dispersion. If the Sommerfeld boundary condition is used for shallow water wave simulations, it reads as follows

$$\left(\frac{\partial}{\partial t} + c \frac{\partial}{\partial n} \right) \Phi = 0,$$

in which tuning coefficient c should be chosen equal to \sqrt{gh} .

In shallow water, the phase velocity \sqrt{gh} is constant. One model for describing irregular waves is to think them composed of infinitely many regular wave components. If we, for reasons of notation, consider an irregular wave to be composed of a discrete number of wave components with frequencies ω_j and wave numbers k_j for $j = 1, 2, \dots, N$, then in the shallow water limit the phase velocities c_j for these wave components are all equal to \sqrt{gh} . The Sommerfeld boundary condition is equally accurate for all N wave components.

It is different in deeper water, for $kh > 0$. Here, the phase velocity is a function of the dimensionless wave number kh

$$c_j = \sqrt{gh} \sqrt{\frac{\tanh(k_j h)}{k_j h}} \text{ for } j = 1, 2, \dots, N. \quad (6.17)$$

When the Sommerfeld boundary condition is used in deep water wave simulations, it will not be equally accurate for all wave components. To demonstrate the accuracy of the Sommerfeld boundary condition, we consider the reflection coefficient

$$R_j = \frac{c - c_j}{c + c_j} \text{ for } j = 1, 2, \dots, N. \quad (6.18)$$

The reflection coefficient for the Sommerfeld condition is derived in Appendix B.

In the Sommerfeld boundary condition, c is a tuning coefficient, which can be chosen freely. But what is an appropriate choice for c in irregular waves where each wave component j has a different phase velocity c_j ? From Eq. (6.18), we see that there is one value for c that gives zero reflection; the reflection coefficient is zero for the wave component j that has a phase velocity c_j equal to c . Wave components with c_j close to c will have very little reflection, but as c_j deviates more from c , the reflection coefficient for those wave components becomes larger and larger.

At sea, wave energy comes in so-called wave energy spectra. Depending on the weather conditions, the distribution of the wave energy over the frequency range can be described by a JONSWAP spectrum, a Pierson-Moskovic spectrum or some other spectral shape [28]. These theoretical spectral shapes show that there is little wave energy at the (very) low frequencies, more wave energy at higher frequencies until the wave

energy reaches a maximum at the peak frequency f_p of the spectrum, after which there is again increasingly less wave energy at higher frequencies in the 'tail' of the spectrum. We will call the phase velocity associated with the peak frequency of the spectrum c_p and the wave number associated with the peak frequency of the spectrum k_p .

An absorbing boundary condition is applied to let wave energy leave the numerical domain. The optimal choice for c in the Sommerfeld boundary condition with irregular wave simulations, then, is that c , which corresponds to the c_j at the peak frequency of the spectrum, i.e. c_p , because that is the wave component with the most energy.

Figure 6.2 shows a JONSWAP spectrum with $\omega_p = 1.5s^{-1}$ and $H_{m0} = 1m$ in the left panel. The right panel of Figure 6.2 shows the theoretical reflected wave spectrum as a function of frequency for three different choices for c : $c = c(\frac{2}{3}k_ph)$, $c = c_p = c(k_ph)$ and $c = c(\frac{3}{2}k_ph)$. The amount of reflected wave energy corresponds to the surface below the lines in Figure 6.2. The figure clearly demonstrates that $c = c(k_ph)$ gives the lowest amount of reflected wave energy and, therefore, is the optimal choice when the Sommerfeld condition is used to absorb irregular waves.

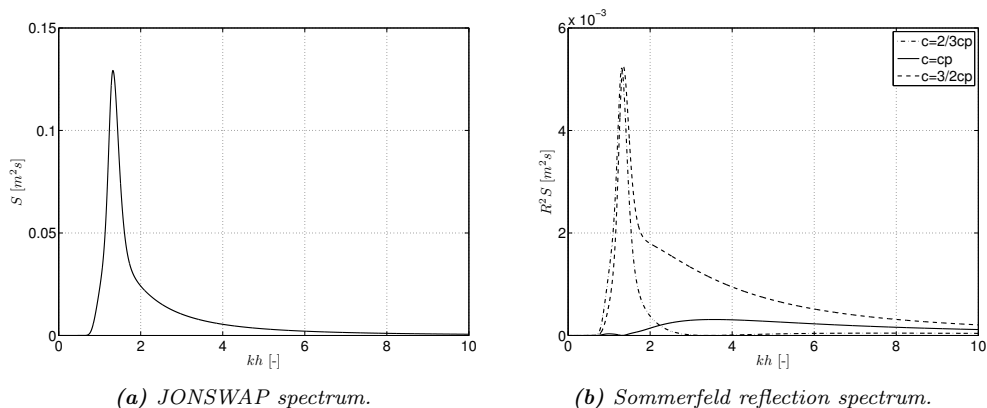


Figure 6.2: JONSWAP spectrum and the Sommerfeld reflection spectrum for three choices of the tuning coefficient c .

The theoretical amount of reflected wave energy for the JONSWAP spectrum in Figure 6.2b is considerable, even for the optimal choice for c . We would like to improve upon the performance of the Sommerfeld condition in irregular wave simulations. To start the derivation of an improved absorbing boundary condition for irregular free surface waves, we transform the Sommerfeld condition to Fourier space

$$(-\omega_j + ck_j) \phi_j = 0 \text{ for } j = 1, 2, \dots, N. \quad (6.19)$$

Here, ϕ_j is the Fourier transform of Φ . The optimal boundary condition for irregular

waves in the frequency domain would be as follows

$$(-\omega_j + c_j k_j) \phi_j = 0 \text{ for } j = 1, 2, \dots, N. \quad (6.20)$$

where c_j follows from Eq. (6.17). In this relation, every wave component is absorbed with a coefficient c_j that corresponds to the actual phase velocity for wave component j . Unfortunately, Eq. (6.20) cannot be transformed back to normal space.

Eq. (6.20) does provide us with the inspiration to derive an improved absorbing boundary condition with respect to the Sommerfeld condition. Apparently, when the coefficients c_j are chosen in accordance with the actual phase velocity obtained from the dispersion relation, there is zero reflection for every wave component. On the other hand, when coefficient c in the Sommerfeld equation is chosen such that it corresponds to only one value in the dispersion relation, there is considerable reflection. Clearly, the better we approximate the dispersion relation in our absorbing boundary condition, the less reflection we obtain.

The concept of approximating the dispersion relation is illustrated in Fig. 6.3. In Fig. 6.3, the normalized dispersion relation is shown in combination with a function

$$f : kh \rightarrow c \quad (6.21)$$

that approximates the dispersion relation in the range $kh \in [0, 10]$. This is how the Sommerfeld condition deals with irregular waves: the difference between the dispersion relation and the approximating function f is an indication of how much reflection there will be for a wave component. Wave components with phase velocities c_j that are close to c will have little reflection, whereas wave components with c_j different from c will reflect more. The reflection coefficient as a function of kh for this choice for c is shown in Fig. 6.3b.

Now, we will introduce a rational polynomial in kh that is a better approximation to the dispersion relation than the constant function f

$$g : kh \rightarrow \sqrt{gh} \frac{a_0 + a_1 (kh)^2}{1 + b_1 (kh)^2}. \quad (6.22)$$

The coefficients a_0 , a_1 and b_1 can be chosen such that different kh -ranges of the dispersion relation are approximated well. With $a_0 = 1$, $a_1 = \frac{3}{20}$ and $b_1 = \frac{19}{20}$, the dispersion relation is approximated near $kh = 0$ with fourth-order accuracy, as can be shown by means of a series expansion. This is illustrated in Fig. 6.4. It gives the dispersion relation and the approximation with function g . In Fig. 6.4, the theoretical reflection coefficient for this choice of the coefficients is shown. Here, one can see that the reflection coefficient with a rational approximation is smaller than with a constant approximation of the dispersion relation for a large range of values for kh .

Next, we substitute $c = g$ into boundary condition (6.19)

$$\begin{aligned} & \left(- \left(1 + b_1 (k_j h)^2 \right) \omega_j + \right. \\ & \left. \sqrt{gh} \left(a_0 + a_1 (k_j h)^2 \right) k_j \right) \phi_j = 0 \text{ for } j = 1, 2, \dots, N. \end{aligned} \quad (6.23)$$

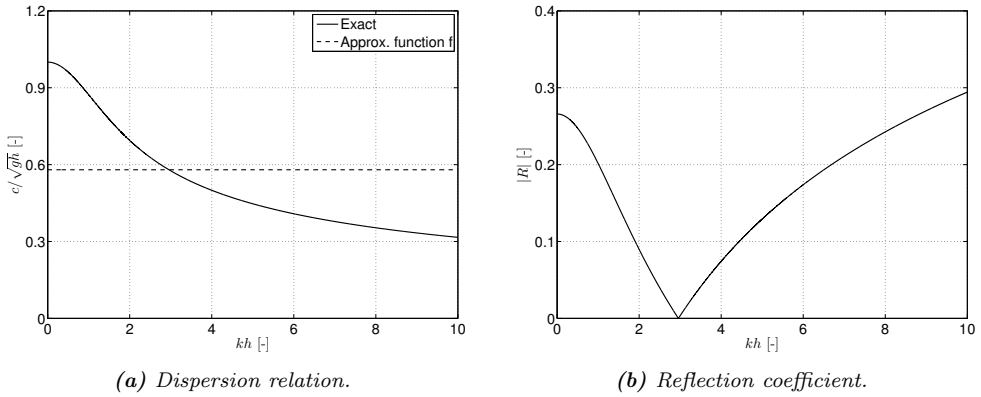


Figure 6.3: Approximation of the dispersion relation with a constant function f , which is characteristic of the Sommerfeld condition, in Fig. (a). In Fig. (b), the reflection coefficient associated with a constant function f .

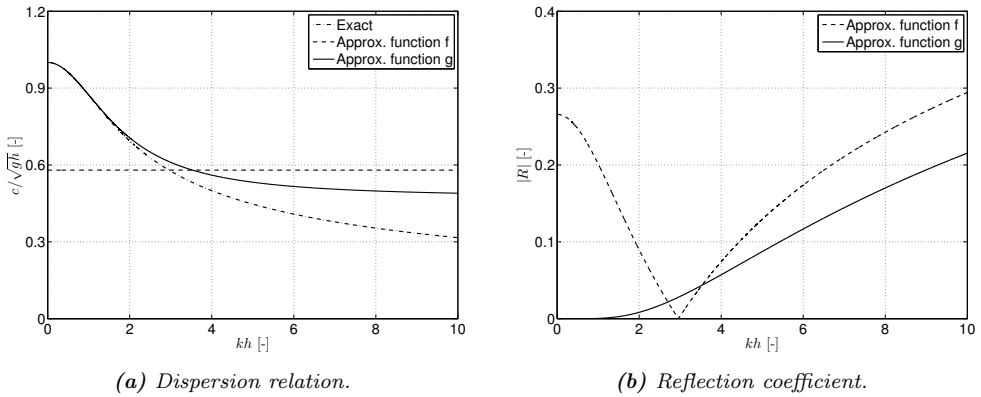


Figure 6.4: Approximation of the dispersion relation with a rational function g , which is part of the improved boundary condition for irregular waves, in (a). In (b), the reflection coefficient associated with the rational function g .

Note that Eq. (6.23) is multiplied by $\left(1 + b_1 (k_j h)^2\right)$.

Still, boundary condition (6.23) cannot be transformed back to normal space, because it is non-linear in k_j . We will try to eliminate the k_j^2 from the boundary condition.

The wave number k_j can be found by taking derivatives of the solution in space. In linear theory, the solution to the system of equations is given by the potential.

Propagating wave components in the time domain satisfy the following relation for the potential

$$\phi_j = \frac{\zeta_a}{k_j g} \frac{\cosh(k_j(z+h))}{\cosh(k_j h)} e^{i(k_j x - \omega_j t)}. \quad (6.24)$$

By taking the second-order derivative in x -direction, we obtain an expression, which is $-k_j^2$ times the potential

$$\frac{\partial^2}{\partial n^2} \phi_j = -k_j^2 \phi_j. \quad (6.25)$$

Eq. (6.25) could be used to eliminate the k_j^2 from the boundary condition. A disadvantage of using horizontal derivatives in the boundary condition is that, in the numerical implementation, these derivatives would have to be evaluated with one-sided discretizations, because there are no grid points beyond the boundary. One-sided approximations are known to be rather inaccurate.

Derivatives along the boundary may be evaluated with central discretizations. For this reason, we prefer to use derivatives in vertical direction to eliminate the k_j^2 from the boundary condition. The second-order derivative of potential function (6.24) in vertical direction is equal to k_j^2 times the potential itself

$$\frac{\partial^2 \phi_j}{\partial z^2} = k_j^2 \phi_j. \quad (6.26)$$

Eq. (6.26) is substituted in boundary condition (6.23) to yield

$$\begin{aligned} & \left(- \left(1 + b_1 h^2 \frac{\partial^2}{\partial z^2} \right) \omega_j + \right. \\ & \left. \sqrt{gh} \left(a_0 + a_1 h^2 \frac{\partial^2}{\partial z^2} \right) k_j \right) \phi_j = 0 \text{ for } j = 1, 2, \dots, N. \end{aligned} \quad (6.27)$$

The absorbing boundary condition in Eq. (6.27) is linear in k_j and can be transformed back from Fourier space. In normal space, the absorbing boundary condition becomes

$$\left(\left(1 + b_1 h^2 \frac{\partial^2}{\partial z^2} \right) \frac{\partial}{\partial t} + \sqrt{gh} \left(a_0 + a_1 h^2 \frac{\partial^2}{\partial z^2} \right) \frac{\partial}{\partial n} \right) \Phi = 0. \quad (6.28)$$

With Eq. (6.28), we have derived an absorbing boundary condition that gives little reflection for wave components within a range of kh -values for which the rational approximation of the dispersion relation in Eq. (6.22) is accurate.

6.4 Stability

The boundary condition derived in the previous section accurately absorbs waves in a range of kh -values where the dispersion relation is well approximated. The range can be chosen by adjusting the parameters a_0 , a_1 and b_1 . Not every set of parameters

leads to a stable solution. This is best explained by elaborating on the different types of wave phenomenon.

Propagating waves are not the only type that satisfies the linearized system of equations in Appendix A. Propagating waves are a specific solution that is characterized by periodic behaviour in time and horizontal space, and exponential behaviour in vertical direction.

Evanescent waves are another solution type. These show periodic behaviour in time and vertical direction, but now the exponential behaviour is in horizontal space. Evanescent waves are mainly observed near wave boards in experimental facilities and their existence is due to wave boards not being of exactly the same shape as the vertical, exponential profile of the propagating waves they mean to create.

The final type that satisfies the linearized system, does not exist in reality; it is a numerical artifact that becomes relevant when the ABC is combined with the system of equations. It features periodic behaviour in vertical space and exponential behaviour in horizontal space and in time. If such a mode exponentially grows, instead of decays in time, it will lead to an unstable simulation. This wave type is an unphysical artefact of the numerical solution process and will from here on be termed 'spurious' wave mode.

It is possible to derive a dispersion relation, an expression that relates frequency to wave number or phase velocity to wave number, for all the wave modes above. The analytical phase velocity $c(kh)$ can then be combined with the approximate phase velocity of the ABC, $c_a(kh)$, into a reflection coefficient:

$$R_{abc} = \frac{c_a(kh) - c(kh)}{c_a(kh) + c(kh)}. \quad (6.29)$$

For propagating wave modes the reflection coefficient is used to determine the performance of the ABC. The ABC performs well if the reflection coefficient is below a certain value. It gives full reflection if R_{abc} is equal to one. Note that when the reflection coefficient is larger than one, energy is added to the system. This is undesirable for an absorbing boundary condition for propagating waves, since it leads to an unstable solution. For propagating wave modes this does not occur.

Spurious wave modes, however, can lead to an unstable solution. For certain choices of the tuning parameters a_0 , a_1 and b_1 , exponentially growing wave modes in time will be part of the solution. Now the reflection coefficient can be used to derive stable sets of parameters. If the reflection coefficient for spurious wave modes stays below one, no unphysical increase of energy will be observed near the boundary and the solution process remains stable.

The dispersion relation for spurious modes is:

$$c_{sp} = \sqrt{gh} \sqrt{\frac{\tan(kh)}{kh}}. \quad (6.30)$$

The absorbing boundary condition with the second derivatives in the vertical applied to the spurious wave potential Φ_{sp} leads to the following approximation of the

dispersion relation:

$$c_a = \sqrt{gh} \frac{a_0 - a_1(kh)^2}{1 - b_1(kh)^2}. \quad (6.31)$$

Note in (6.31) that the second derivatives, combined with the cosine-behaviour of the spurious modes in vertical direction (see Appendix A) leads to minus-signs in the approximation of the phase velocity.

The dispersion relation for spurious waves and the approximation of the boundary condition are substituted into the expression for the reflection coefficient. The absolute value of the reflection coefficient needs to remain smaller than one:

$$|R_{sp}| = \left| \frac{c_a(kh) - c_{sp}(kh)}{c_a(kh) + c_{sp}(kh)} \right| < 1. \quad (6.32)$$

The expression for the dispersion relation of the spurious wave mode is substituted into the reflection coefficient, along with the expression for the approximation of the dispersion relation by the boundary condition. The stability criterion then becomes

$$\frac{\frac{a_0 - a_1(kh)^2}{1 - b_1(kh)^2} - \sqrt{\frac{\tan(kh)}{kh}}}{\frac{a_0 - a_1(kh)^2}{1 - b_1(kh)^2} + \sqrt{\frac{\tan(kh)}{kh}}} < 1 \quad (6.33)$$

Eq. (6.33) has singularities, where the denominator has roots. Consider the following functions

$$\begin{aligned} f_1 : kh &\rightarrow \sqrt{\frac{\tan(kh)}{kh}} \\ f_2 : kh &\rightarrow a_0 - a_1(kh)^2 \\ f_3 : kh &\rightarrow 1 - b_1(kh)^2 \end{aligned} \quad (6.34)$$

Functions f_1 and f_2 in (6.34) are plotted in Fig. 6.5. The figure shows only the real values of f_1 . It has imaginary values in the range $kh \in [\pi/2, \pi]$. The range of imaginary values gives us the opportunity to ensure stability. If the roots of the functions f_2 and f_3 in Eq. (6.34) are chosen in the range where f_1 has imaginary values, then instability cannot occur. This puts restrictions on the values for the coefficients a_1 and b_1 . In Fig. 6.5, the function f_2 is plotted with $a_0 = 1$ and two different values for a_1 , $a_1 = a_0/\pi^2$ and $a_1 = a_0/4\pi^2$. With these values for a_1 , the roots of f_2 are precisely on the outer limits of the range $kh \in [\pi/2, \pi]$. Therefore, the first requirement for stability is that a_1 has a value between a_0/π^2 and $4a_0/\pi^2$.

The same line of reasoning applies to the function f_3 in Eq. (6.34) and the value for b_1 . The second requirement for stability, then, is that the value for b_1 is chosen between $1/\pi^2$ and $4/\pi^2$.

The third and final requirement for stability comes from the limit behaviour of the reflection coefficient in Eq. (6.33). If we consider the limit $kh \rightarrow \infty$ of the reflection

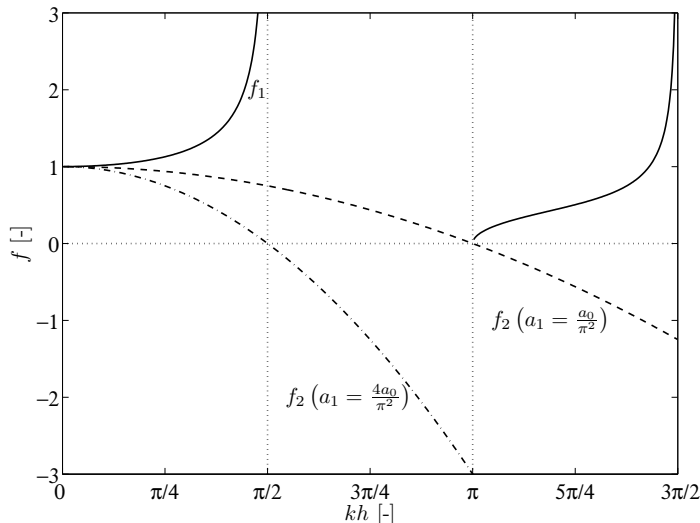


Figure 6.5: Roots of the reflection coefficient's denominator.

coefficient, it is found that b_1 should be larger than a_1 to ensure that $R \leq 1$ and, hence, stability. This is a stronger requirement for stability than that b_1 should be larger than $1/\pi^2$: the value for b_1 should in fact be between a_1 and $4/\pi^2$.

Summarizing the inequalities for the coefficients

$$\begin{aligned} \frac{a_0}{\pi^2} < a_1 < \frac{4a_0}{\pi^2} \quad \text{and} \\ a_1 < b_1 < \frac{4}{\pi^2}. \end{aligned} \tag{6.35}$$

The behaviour of Eq. (6.33) is the same for every interval $kh \in \langle n\pi/2, n\pi \rangle$ for $n = 1, 3, 5, \dots$. If the coefficients a_1 and b_1 are chosen in such a way that the roots of the functions f_2 and f_3 are in these intervals, stability is ensured. Within these constraints, one is free to approximate the dispersion relation for propagating wave modes as best he can. Fig. 6.6 gives an example of what the reflection coefficient for a spurious wave mode looks like when either a stable set of coefficients - $a_0 = 1.05$, $a_1 = 0.12$ and $b_1 = 0.31$ - or an unstable set of coefficients - $a_0 = 1.05$, $a_1 = 0.10$ and $b_1 = 0.31$ - is chosen. Here, the stability criterion that a_1 has to be larger than a_0/π^2 is violated.

The following, stable choice for the parameters - $a_0 = 1.040$, $a_1 = 0.106$, $b_1 = 0.289$ - approximates the dispersion relation in the range $kh \in \langle 0, 6 \rangle$ with a reflection coefficient R of at most 0.02, see Fig. 6.7.

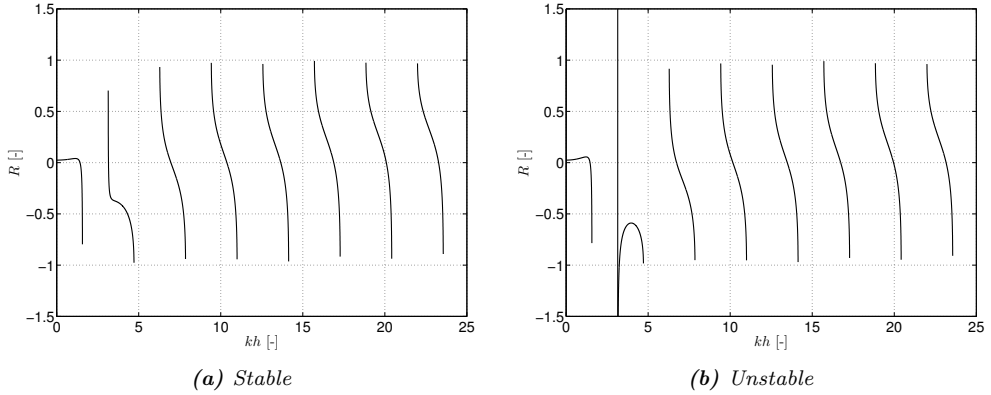


Figure 6.6: Reflection coefficient of a spurious wave mode for a stable set of coefficients – $a_0 = 1.05$, $a_1 = 0.10$ and $b_1 = 0.31$ – and the reflection coefficient for an unstable set – $a_0 = 1.05$, $a_1 = 0.12$ and $b_1 = 0.31$. Solution modes become unstable when the reflection coefficient is larger than one.

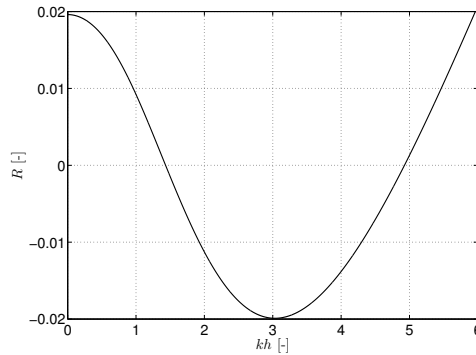


Figure 6.7: Reflection coefficient for a stable set of parameters. The reflection coefficient is smaller than 2% over a range of $kh \in \langle 0, 6 \rangle$.

6.5 Incoming and outgoing waves

At the boundary, incoming waves need to be specified while preventing re-reflection of outgoing waves at the same time. In the ABC, we follow Carpenter [7] and Perkins et al. [40] and prescribe the incoming characteristic with a non-zero right-hand side consisting of the same combination of operators applied to the incoming wave potential, see Section 6.1.3.

With a non-zero right-hand side, absorbing boundary condition (6.28) becomes:

$$\left[\left(1 + b_1 h^2 \frac{\partial^2}{\partial z^2} \right) \frac{\partial}{\partial t} + \sqrt{gh} \left(a_0 + a_1 h^2 \frac{\partial^2}{\partial z^2} \right) \frac{\partial}{\partial x} \right] \Phi = \mathcal{R}^{in}, \quad (6.36)$$

in which:

$$\mathcal{R}^{in} = \left[\left(1 + b_1 h^2 \frac{\partial^2}{\partial z^2} \right) \frac{\partial}{\partial t} + \sqrt{gh} \left(a_0 + a_1 h^2 \frac{\partial^2}{\partial z^2} \right) \frac{\partial}{\partial x} \right] \Phi^{in}.$$

Here, Φ^{in} is the incoming wave potential. The incoming wave potential at the boundary varies as a function of time. Now that the incoming wave has become part of the boundary condition, a Generating/Absorbing Boundary Condition for long-crested dispersive waves has been obtained that we will abbreviate to GABC. This is a truly open boundary condition, through which waves can enter and leave the domain over the same boundary at the same time with little spurious re-reflection of waves within the rational approximation's range of accuracy.

6.6 Numerical implementation

6.6.1 Discrete equations

The ABC in (6.28) is used as a boundary condition for outgoing waves in COMFLOW. Our numerical method solves for velocities and pressures and, therefore, the ABC needs to be expressed in terms of the same variables.

In potential theory the velocity in n -direction is related to the derivative of the potential Φ in that direction:

$$\frac{\partial \Phi}{\partial n} = u_b. \quad (6.37)$$

The subscript b now indicates that the velocity is defined exactly on the domain boundary. To derive an expression for the pressure, the Bernoulli equation is linearized. Then:

$$\frac{\partial \Phi}{\partial t} = -\frac{p_b}{\rho} - gz. \quad (6.38)$$

For notation purposes the density in the remainder of this section is assumed to be equal to one. Again, in (6.38), the subscript b indicates that the pressure is defined at the domain boundary. After substitution of (6.37) and (6.38) into the ABC, an expression in terms of pressure and velocity at the domain boundary is obtained:

$$-\sqrt{gh} \left(a_0 + a_1 h^2 \frac{\partial^2}{\partial z^2} \right) u_b + \left(1 + b_1 h^2 \frac{\partial^2}{\partial z^2} \right) p_b = gz + \mathcal{R}^{in}. \quad (6.39)$$

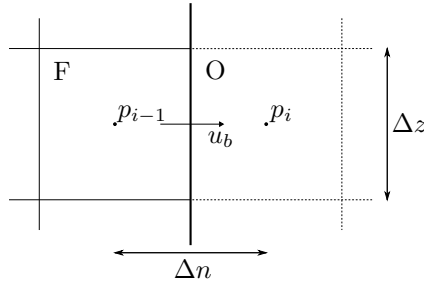


Figure 6.8: Definition of the solution variables at the boundary. The boundary condition is applied to solve for p_i . It is positioned in the center of the mirror cell outside the domain.

The solution variables are staggered within a cell. The domain boundary is chosen such that it coincides with the position of the horizontal velocity u_b .

It is essential that the velocity and pressure in the ABC are defined at the same position. Any other configuration would lead to phase differences between solution variables at the boundary and additional spurious reflection. The pressure at the boundary is obtained from linear interpolation between the pressures on either side of the boundary:

$$p_b = \frac{1}{2}(p_{i-1} + p_i). \quad (6.40)$$

It is equally essential that the pressure and the velocity at the boundary are defined at the same point in time. For a boundary condition in terms of pressures, the pressure at the boundary is determined at time t^{n+1} . The horizontal velocity at the new time level u_b^{n+1} can be eliminated by means of the momentum equation at the boundary:

$$u_b^{n+1} = u_{i-1}^{n+1} = \tilde{u}_{i-1} - \frac{\Delta t}{\Delta x}(p_i - p_{i-1})^{n+1}. \quad (6.41)$$

Note that \tilde{u} includes convective and diffusive terms, see Eq. (3.15).

The second derivatives in the ABC are approximated by the operator in (6.42). The operator has been derived for a stretched grid in the vertical direction and is second order accurate, see Fig. 6.9. It reads

$$\mathcal{V} = \begin{pmatrix} \mathcal{V}_1 \\ \mathcal{V}_2 \\ \mathcal{V}_3 \end{pmatrix} = \frac{1}{\frac{1}{2}\Delta z_z \Delta z_n (\Delta z_z + \Delta z_n)} \begin{pmatrix} \Delta z_n \\ -\Delta z_z - \Delta z_n \\ \Delta z_z \end{pmatrix}. \quad (6.42)$$

Now the following vectors for the horizontal velocity and the pressure are introduced:

$$\tilde{\mathbf{u}} = \begin{pmatrix} \tilde{u}_{k-1} \\ \tilde{u}_k \\ \tilde{u}_{k+1} \end{pmatrix}, \quad \mathbf{p} = \begin{pmatrix} p_{k-1} \\ p_k \\ p_{k+1} \end{pmatrix}. \quad (6.43)$$

By combining (6.39) through (6.43) a discrete equation for the absorbing boundary condition is obtained:

$$\begin{pmatrix} \mathcal{C}_{lz} & \mathcal{C}_{xl} & \mathcal{C}_{ln} \end{pmatrix} \mathbf{p}_{i-1} + \begin{pmatrix} \mathcal{C}_{zl} & \mathcal{C}_c & \mathcal{C}_{zr} \end{pmatrix} \mathbf{p}_i = gz_k + \begin{pmatrix} \mathcal{N}_{zl} & \mathcal{N}_c & \mathcal{N}_{zr} \end{pmatrix} \tilde{\mathbf{u}}_{i-1} + \mathcal{R}^{in}. \quad (6.44)$$

The matrix coefficients in \mathcal{C} are equal to (see Fig. 6.9 for the position of these coefficients):

$$\begin{aligned} \mathcal{C}_{lz} &= \left(-\chi\tau + \frac{1}{2}\psi \right) \mathcal{V}_1 \\ \mathcal{C}_{xl} &= -\varphi\tau + \frac{1}{2} - \left(\chi\tau - \frac{1}{2}\psi \right) \mathcal{V}_2 \\ \mathcal{C}_{ln} &= \left(-\chi\tau + \frac{1}{2}\psi \right) \mathcal{V}_3 \\ \mathcal{C}_{zl} &= \left(\chi\tau + \frac{1}{2}\psi \right) \mathcal{V}_1 \\ \mathcal{C}_c &= \varphi\tau + \frac{1}{2} + \left(\chi\tau + \frac{1}{2}\psi \right) \mathcal{V}_2 \\ \mathcal{C}_{zr} &= \left(\chi\tau + \frac{1}{2}\psi \right) \mathcal{V}_3. \end{aligned}$$

The coefficients in \mathcal{N} are as follows:

$$\begin{aligned} \mathcal{N}_{zl} &= \chi\mathcal{V}_1 \\ \mathcal{N}_c &= \varphi - \chi\mathcal{V}_2 \\ \mathcal{N}_{zr} &= \chi\mathcal{V}_3. \end{aligned}$$

In the relations above, these coefficients were used:

$$\varphi = \sqrt{gha_0}, \quad \chi = \sqrt{gha_1}h^2, \quad \psi = b_1h^2 \quad \text{and} \quad \tau = \frac{\Delta t}{\Delta n}.$$

Equation (6.44) has been set up as an equation for p_i in a mirror cell outside the domain. It features only pressures at the new time level t^{n+1} on the left hand side, and horizontal velocities that include convective and diffusive terms on the old time level t^n on the right hand side. The structure of the discrete ABC bears great resemblance to the pressure Poisson equation derived in section 3.3.4 and can therefore easily be combined with the field equations for the inside of the domain.

Setting up the extended pressure Poisson equation is one matter, solving it is another. The left-hand side matrix includes coefficients that are not common in a regular Poisson solver stencil. The stencil at the boundary in 2D is shown in Fig. 6.9.

The matrix, including the additional coefficients of the absorbing boundary condition, is not symmetric, nor diagonally dominant. The SOR routine in [4] fails to converge.

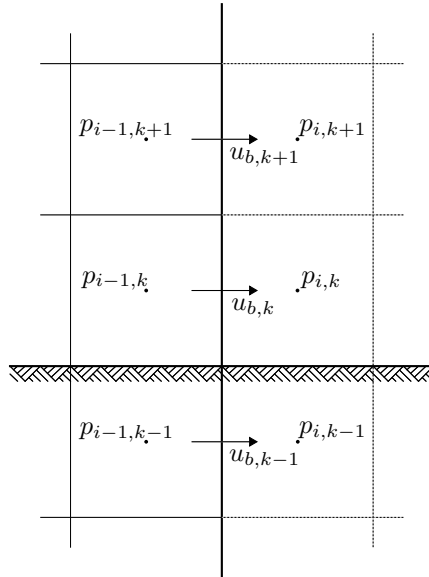


Figure 6.10: Implementation of the absorbing boundary condition at the bottom. The solution variables below the bottom are expressed in the solution variables above the bottom.

Instead, a compromise was implemented. In the cell containing the free surface, no second derivative is calculated. In the O-cell nearest to the S-cell inside the domain, an ordinary Sommerfeld equation, such as (6.4), is solved with a well chosen value for $c^{(o)}$. This equation is implemented at the cost of accuracy, but at the moment an alternative is not available.

6.7 Waves under an angle with the boundary

Until now, we have only considered long-crested waves with normal incidence to the boundary; long-crested waves were assumed in the derivation of the absorbing boundary condition and in the implementation. The assumption is justified, because we often perform long-crested wave simulations, even in three dimensions. But when a structure is included in the domain, it generates wave diffraction (and radiation) in all directions around the structure. Diffracted waves can impinge on the boundary at any angle.

To study the reflection coefficient of the absorbing boundary condition for waves under an angle with respect to the boundary, the axis system in Fig. 6.12 is introduced. The vector normal to the boundary will be called \mathbf{n} and the angle with this vector is defined as θ .

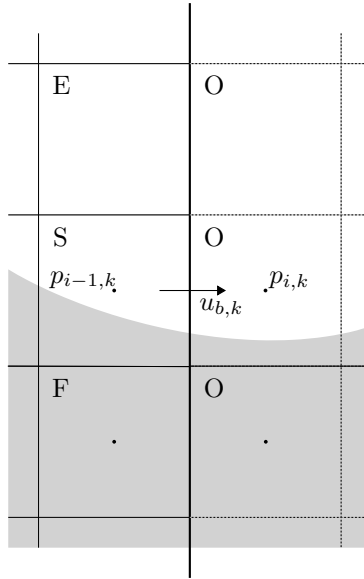


Figure 6.11: At the free surface near the boundary no second derivative is calculated. Instead, a Sommerfeld equation is solved at the SO-cell boundary.

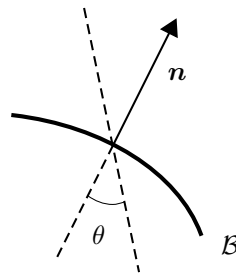


Figure 6.12: Axis system at the boundary. Waves can impinge on the boundary at an angle. The angle θ is defined with respect to the boundary's normal vector \mathbf{n} .

Waves propagating with a certain phase velocity c , under an angle with the boundary, appear to approach the boundary at a higher velocity. The apparent velocity needs to be accounted for in the absorbing boundary condition:

$$\left(\frac{\partial}{\partial t} + \frac{c}{\cos \theta} \frac{\partial}{\partial n} \right) \Phi = 0. \tag{6.46}$$

Analogous to the discussion regarding dispersive waves, boundary condition (6.46)

can never be imposed, because the directions θ_i of the individual wave components ϕ_i cannot be resolved at the boundary. The term $c/\cos\theta$ is therefore approximated by either a fixed value (Sommerfeld) or the rational approximation of the dispersion relation that has been introduced earlier in this chapter.

In Fig. 6.13, the reflection coefficient in percentages of the Sommerfeld condition, with $c/\cos\theta = 2/3\sqrt{gh}$, is compared to that of the rational approximation, with $a_0 = 1.040, a_1 = 0.106, b_1 = 0.289$. It has been determined for a range of kh -values and angles of incidence between zero and ninety degrees. In these figures, the area where the reflection coefficient is below five percent has been enclosed by a bold line; five percent reflection is considered tolerable in practical simulations for wave impacts.

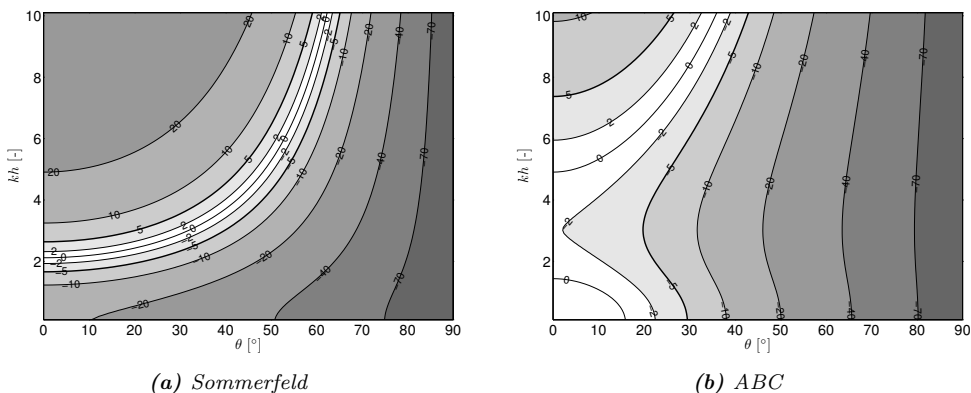


Figure 6.13: Reflection coefficient in percentages as a function of the incidence angle θ and the dimensionless wave number kh . The Sommerfeld condition is compared to the ABC with a rational approximation. In the boundary condition we have used $c/\cos\theta = 2/3\sqrt{gh}$ and $a_0 = 1.040, a_1 = 0.106, b_1 = 0.289$, respectively.

From Fig. 6.13, we find that the performance of the ABC is not much better than the Sommerfeld condition in terms of the range of angles. If less reflection of waves at larger incident angles with the boundary is desired, we need to account for this angle in the boundary condition. There is literature available, see section 6.1.1, but ABCs for waves under an angle are not addressed in this thesis. This is part of future research concerning ABCs in the COMFLOW-3 project.

6.8 Results

In this section, the performance of the absorbing boundary condition will be tested. The performance is better when there is less reflection. The reflection coefficient will

be obtained from irregular wave simulations with an ABC at the downstream end of the domain and compared to the theoretical reflection coefficient.

There are ways to determine the propagation direction and the frequency content from a set of wave signals, measured at multiple carefully chosen locations [52]. These methods, however, perform worse as waves become steeper and they will wrongly attribute numerical effects, such as phase lagging or wave energy dissipation to propagating waves.

In this research, therefore, another method to assess the performance of the ABC in practical circumstances is proposed. First a wave simulation is performed in an infinitely long domain. 'Infinite', in this sense, means that the domain length is chosen such, that during the entire measurement time, reflected waves cannot reach the measurement location. The required domain length can be obtained from the phase velocity of the fastest propagating wave components and the duration of the simulation, $L_d = \sqrt{gh} t_{max}$.

Then another simulation is performed. This simulation is the same as the previous simulation in every respect, except for the domain length and the boundary procedure at the outflow end of the domain. Measurements of the surface elevation, taken at exactly the same positions, are compared to measurements on the 'infinite' domain. Everything being the same, the difference can only be attributed to the boundary procedure. The infinite domain and the shorter domain with the boundary condition are shown in Fig. 6.14; the figure also indicates the measurement position in the middle of the short domain.

In this way, different boundary procedures may be compared. Three comparisons are made:

- Sommerfeld vs. ABC
- Dissipation zone vs. ABC
- ABC vs. combined short dissipation zone and ABC

The setup of the simulations is outlined in Tables 6.1 through 6.3. The domain is 2D, which means that only long crested waves are considered. The domain sizes and the grid distances are stated in Table 6.1. The cells have a uniform size in the horizontal direction and are stretched in the vertical direction. In a study by Meskers [36] it was found that the quality of simulated waves increases with decreasing time step. And in order to be sure that not only the measurement position in space, but also the measurement positions in time are the same throughout all simulations, the time increment Δt is kept fixed and small.

The simulations are started from rest: at t_0 there are no waves in the domain and the velocities \vec{u} are zero. Waves are imposed on the left of the domain by means of linear potential theory. With a linear ramp function the signals of surface elevation and velocities at the inflow boundary are gradually built up over a period of 20s. The irregular wave signal consists of a superposition of regular wave components that accord with a realistic JONSWAP spectrum, see Table 6.2. For more information on

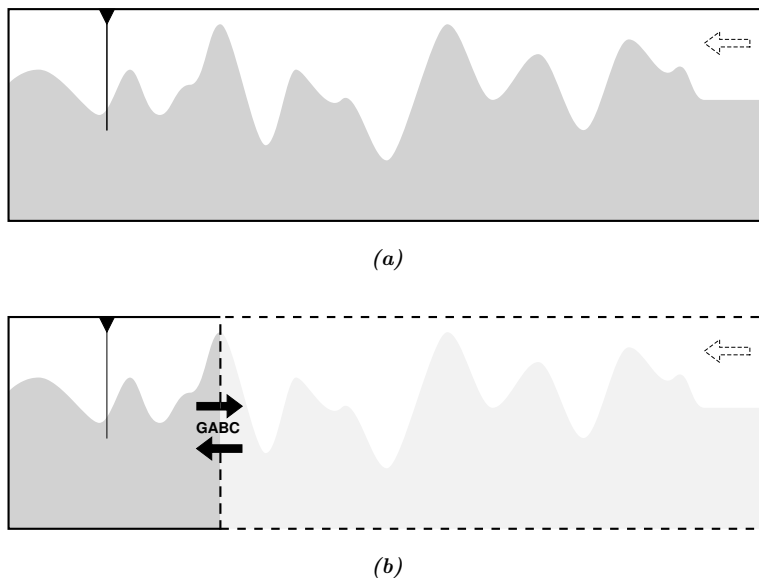


Figure 6.14: *Simulation in a long domain and simulation in a short domain with the GABC at the end. Surface elevation measurements are taken in the middle of the short domain and compared to the surface elevation in the long domain to determine the reflection.*

default wave spectra and how a spectrum is obtained from a time series, the reader is referred to Holthuijsen [28].

The coefficients of the outflow boundary conditions are in Table 6.3. The coefficients for the ABC are tuned in such a way that the reflection coefficient over the range $kh \in \langle 0, 6 \rangle$ is never larger than 0.02. The Sommerfeld boundary condition at the free surface has only one coefficient to tune, the outgoing phase velocity $c^{(o)}$. The best choice for the outgoing phase velocity is the one associated with the peak period of the spectrum.

[36] gives the optimal configuration of a beach when linear theory is assumed. The length of the beach, expressed in number of wave lengths, will be determined based on the wave length associated with the peak period of the spectrum. The optimal number of wave lengths for this simulation, when a theoretical reflection coefficient of 0.02 is desired, is two. The slope of the damping function is based on the peak frequency. Then, finally, in the case of the combined ABC and beach, the beach length is chosen much shorter; the slope however remains the same.

The wave signal at the measurement location in the infinite domain ζ_{ref} is subtracted from the wave signals in the domains where boundary procedures were applied, so that a reflection signal is obtained. The wave and reflection signals are decomposed into their Fourier components. The Fourier components are then converted to both

Table 6.1: Domain and grid

Parameter	Symbol	Value
Water depth	h	100m
Domain length	l_∞	10000m
Domain length	l	400m
Measurement position	x_m	200m
Horizontal grid distance	Δx	1m
Vertical grid distance	Δz_{min}	0.2m
Vertical grid distance	Δz_{max}	4.95m
Vertical stretch factor	ξ	1.05 [-]
Time step	Δt	0.01s
Simulated time	T	600s

Table 6.2: JONSWAP spectrum

Parameter	Symbol	Value
Peak period	T_p	15s
Significant wave height	H_s	4m

spectra and reflection coefficients. Finally, the parameters are compared to the values they should theoretically have and to each other. This is displayed in Figures 6.15 through 6.17.

The Sommerfeld condition performs best for one kh -value, the one it has been tuned for. Both the theoretical reflection coefficient and the reflection coefficient obtained from the results are zero. Away from this kh -value the performance quickly becomes worse. Results from the Sommerfeld simulation agree well with theory.

The ABC, which has the distinguishing feature to be accurate over a range of kh -values, performs better than the Sommerfeld condition. The amount of wave energy that is reflected is marginal compared to the input spectrum. However, the reflection coefficient for the shorter waves is worse than theory. There are three possible reasons for the difference between theory and practise: first, it may be attributed to the procedure to determine the spectra. The simulation period was rather short compared to the peak period of the spectrum and there may not have been enough zero crossings to properly determine the reflection spectrum. The second reason may be the Sommerfeld condition in the S-cell at the boundary. This relation was tuned to the peak period of the spectrum and will especially cause reflection of shorter components, in which the velocity gradients are largest at the free surface. And finally, non-linear effects near the boundary are not accounted for. This may also result in more reflection than anticipated.

Although the dissipation zone was specifically tuned for the peak frequency of the spectrum, see [36], its performance at this frequency does not agree well with what was expected. With a size of two times the tuning wave length and the chosen slope of the damping function, the expected value of the reflection coefficient was $|R| = 0.02$. The obtained value was one. All of the wave energy at this kh -value was reflected. We

Table 6.3: *Coefficients of the boundary procedures*

Parameter	Symbol	Value
ABC coefficient	a_0	1.05 [-]
ABC coefficient	a_1	0.12 [-]
ABC coefficient	b_1	0.31 [-]
Outgoing phase velocity	$c^{(o)}/\sqrt{gh}$	0.58 [-]
Beach length	ℓ_{beach}	200m
Beach length	ℓ_{abc}	50m
Slope damping function	β	0.05 [-]

believe this is due to non-linear effects in the dissipation zone. Because the derivation in [36] is based on linear theory, it could not have predicted this behaviour.

In addition, the behaviour of the dissipation zone for very long waves was alarming. Although almost no energy for the very long waves was present in the input spectrum, it seems to have been generated as a result of non-linear interaction within the dissipation zone. The dissipation zone does seem to perform well for the short waves with kh -values larger than π .

The final simulation was performed with a dissipation zone combined with the absorbing boundary condition. The results in Fig. 6.17 show that they supplement each other's strong points. The ABC did not perform very well for the shorter waves. And now a short beach with a small slope of the damping function takes care of those, while the ABC prevents the reflection of the longer waves. The ABC with a dissipation zone is a meaningful combination at the outflow end of the domain. At the inflow end of the domain, we must note, a dissipation zone would extract wave energy from the incoming waves, which is undesirable naturally. For this reason, we do not recommend combining the ABC with a dissipation zone at the inflow end of the domain.

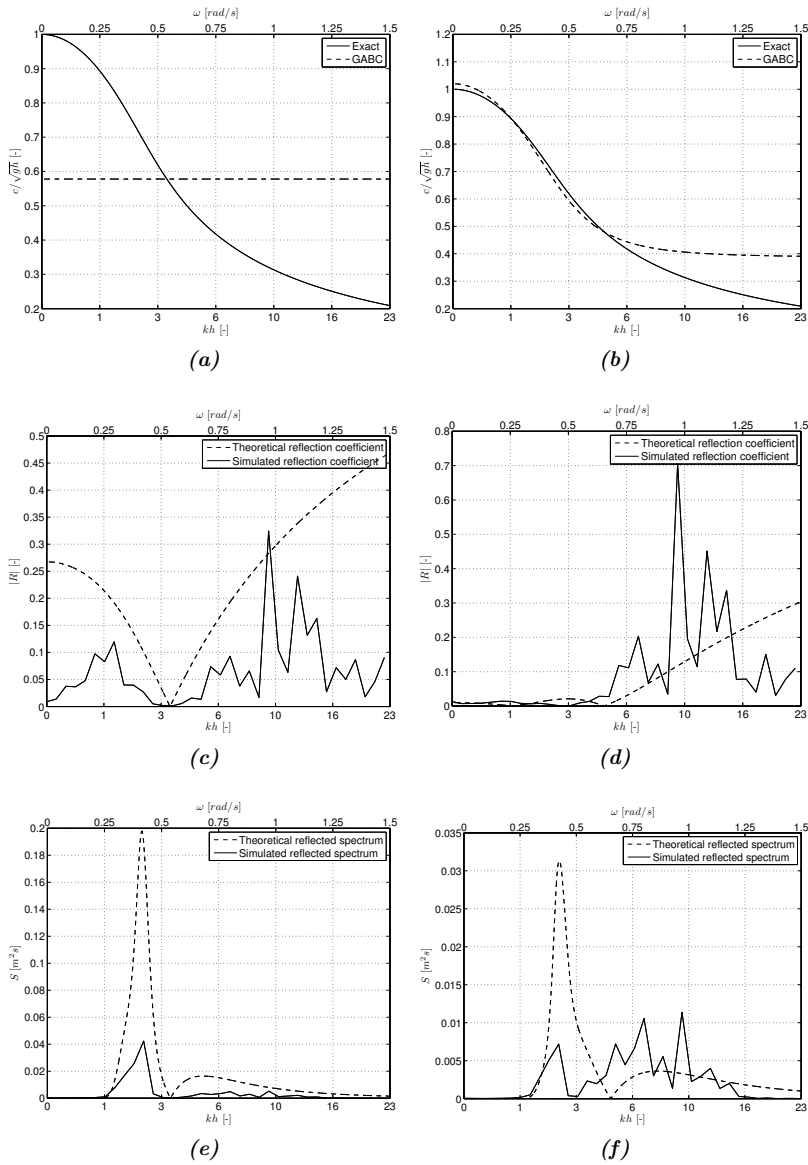


Figure 6.15: Reflection – Sommerfeld in the left column vs. ABC in the right column. The top row, in (a) and (b), shows the exact linear dispersion relation and the approximations made by the applied boundary conditions. The second row, in (c) and (d), shows the theoretical reflection coefficient compared with the reflection coefficient that was obtained numerically. The bottom row shows the theoretical reflection spectrum, compared with the numerically obtained reflection spectrum.

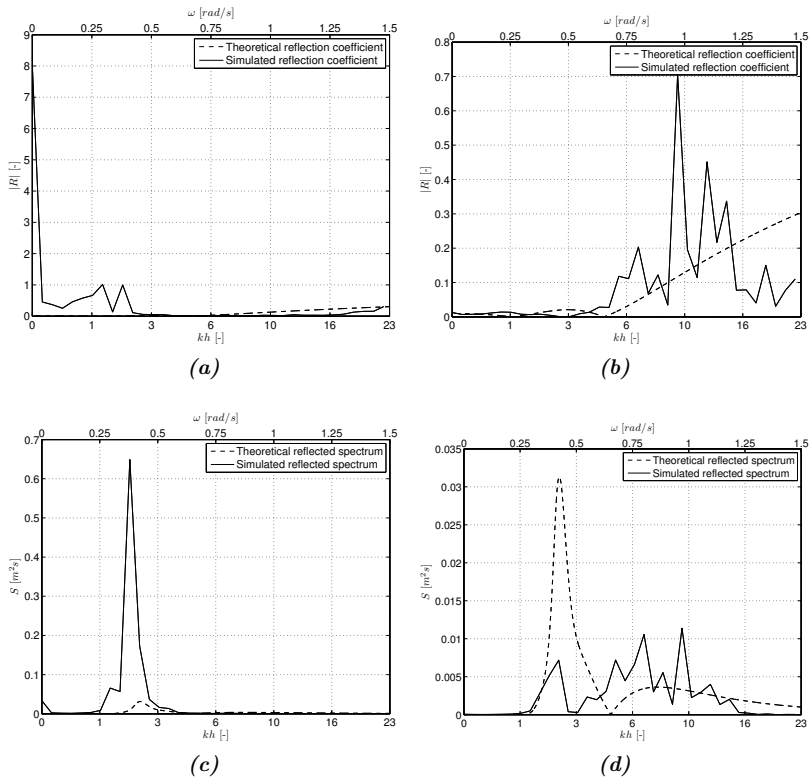


Figure 6.16: Reflection – Dissipation zone in the left column vs. ABC in the right column. The top row, in (a) and (b), shows the reflection coefficients that were obtained numerically. The bottom row, in (c) and (d) shows the reflection spectra.

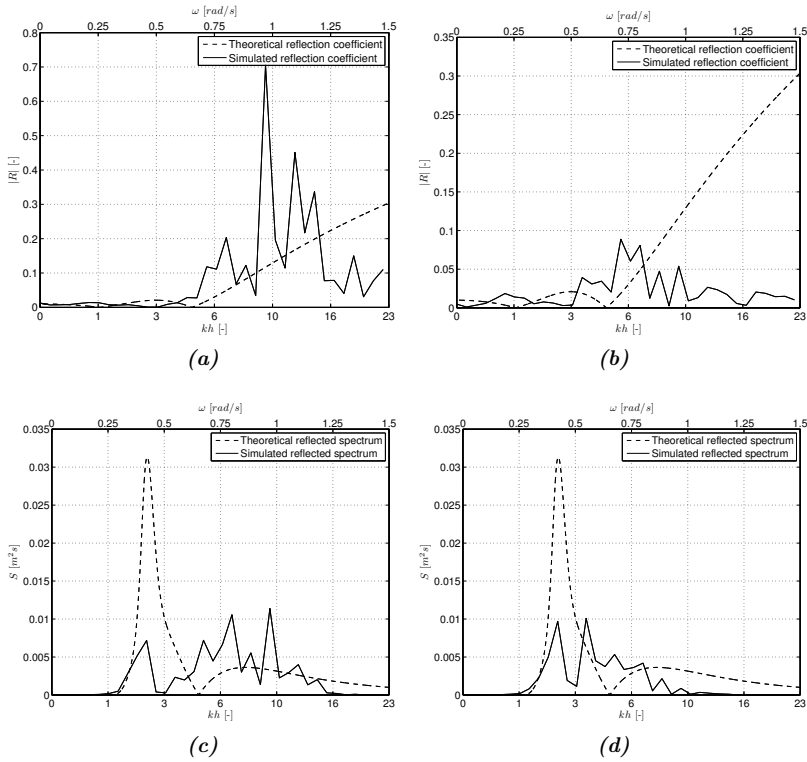


Figure 6.17: Reflection – ABC in the left column vs. combined dissipation zone and ABC in the right column. The top row, in (a) and (b), shows the reflection coefficients that were obtained numerically. The bottom row, in (c) and (d) shows the reflection spectra.

Chapter 7

Validation study

In this chapter, 3D COMFLOW wave simulation results are compared with experimental results. The simulations are performed with the GABC specified at the boundaries to prevent re-reflection of waves back into the domain. We will describe the experimental setup and provide an overview of the relevant parameters in the numerical simulations.

7.1 Introduction

A semi-submersible is a floating structure used for offshore drilling and/or offshore oil production. The structure is characterized by a deck on multiple free surface piercing columns and a large submerged pontoon. This configuration has been designed for its favourable motion behaviour: it has a relatively large underwater volume and relatively small surface level area. The mass-stiffness ratio yields a high natural period, which is outside the range of excitation for the location where the semi-submersible is installed.

A semi-submersible is not very mobile and can be caught in heavy storms at sea. A pivotal aspect in the design of a semi-submersible is that the deck is kept free of impact, even in heavy storm. The distance between the free surface and the deck is called air gap. The design team will try to keep the air gap as small as possible for economic reasons, but large enough to prevent the deck from being hit by a wave.

The minimum air gap cannot be determined from the meteocean data alone. The interaction between the water and the structure – and especially the underwater pontoon – locally generates extra high waves relative to the motion of the structure. 3D boundary element methods are often used to derive statistics on what the relative wave height will be and to determine the chance of deck impact. BEM methods, however, are not suitable to determine the forces associated with a deck impact if it were to occur.

In addition to the BEM simulations, a series of experiments is often performed to proof the design. Numerical simulation (other, more detailed than BEM) can be of great value to support the experiments. Simulations beforehand might indicate the areas that deserve special interest. Simulations afterwards can be performed to examine if small variations may lead to a better design.

Before any conclusions can be drawn from the numerical results, it is imperative to determine if the numerical method is adequate to simulate a semi-submersible in ocean environments. During the development of COMFLOW specifically designed experiments have been performed at the Maritime Research Institute Netherlands (MARIN) to validate the results. One of these experiments has been for a semi-submersible.

7.2 Experiment

The model of the semi-submersible consists of two columns and a pontoon under water, see Fig. 7.1. The experiments were performed at scale 1:50. The model was kept restrained during the experiments, because a restrained model gives the largest amount of diffraction and run-up of water on the columns. Deck impacts are almost guaranteed. This is highly undesirable for an actual design, but gives the best circumstances to validate the numerical model.

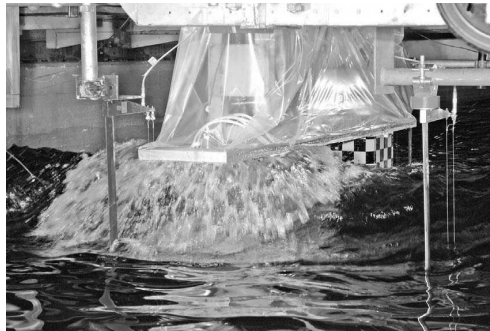


Figure 7.1: Wave impact on the semi-submersible model during a regular wave test.

The experiments were performed in a very long, but quite narrow wave basin. Waves were generated with a pivoting wave board at one of the narrow ends of the tank. At the opposing end a beach was present to induce wave breaking and reduce reflection. The model was placed a considerable distance away from the wave board.

During the experiment surface elevations were measured around and in between columns. Surface elevations were also measured some distance away from the structure, both in front of and behind the structure. The columns and the deck were equipped with pressure transducers to be able to monitor the build-up of pressure

during a wave impact. Figure 7.2 shows the positions of the wave probes and pressure transducers that will be used to compare numerical simulation results to the experimental results.

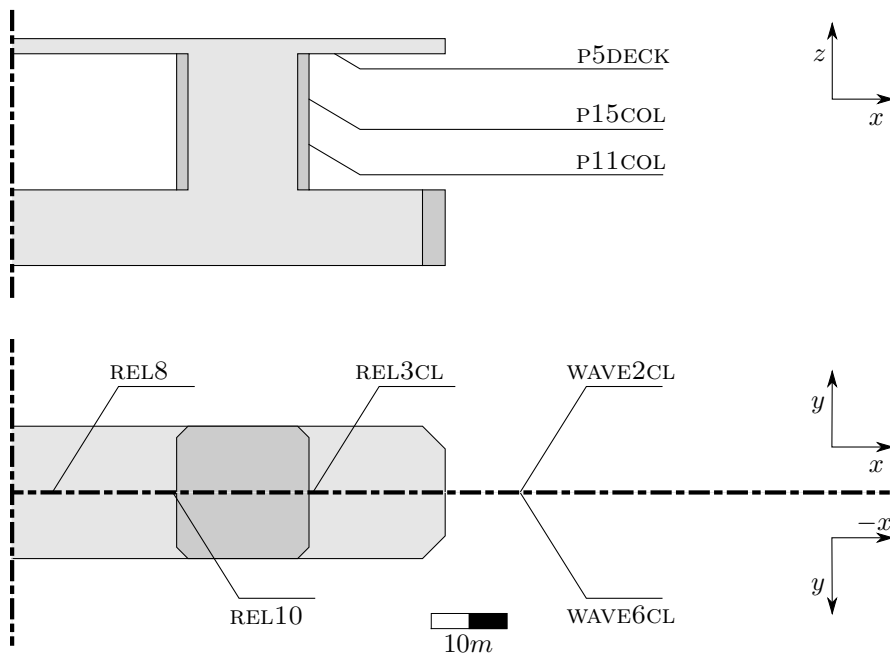


Figure 7.2: *Transducer locations*

Several sea states were created: regular long crested waves of different periods and wave heights, and a number of irregular long crested sea states. In Table 7.1 the test identification numbers of the experiments used in this chapter are given, along with the wave heights and periods associated with these tests.

Table 7.1: *Wave height and period of regular wave experiments*

Test ID	H [m]	T [s]
202002	8.0	9.0
202003	15.0	11.0
202006	10.25	11.0

7.3 Simulation

Several simulations have been performed. The effect of a grid improvement was studied and is reported without much attention to the specific wave absorbing boundary conditions used for these simulations. Then, a sensitivity study is performed: we investigate how the results change when the boundary, with different ABCs, is placed closer to the structure. And, finally, to show the type of simulation the GABC was designed for, results of an irregular wave simulation over a significant time span are presented.

7.3.1 Grid study

Two simulations are compared to each other and to the experiment. The experimental data comes from test 202003. One simulation was performed with a mesh size of $\Delta x = 0.8m$ on a uniform grid. For the other, the mesh was refined to a size of $\Delta x = 0.5m$. It was not possible to compute with even finer grids on the PCs that were at our disposal.

The domain size in x -direction was chosen to correspond to two wave lengths, one in front of the structure and one wave length on the trailing side of the structure. The wave length equals around $L = 200m$. In the y -direction the full width of the experimental basin was modelled, which results in a total size in this direction of $200m$, with the structure in the middle. In the vertical direction, too, the total depth of the basin was modelled, which is $175m$ at prototype scale.

The simulation is started with the wave kinematics prescribed throughout the domain. Note that analytical wave theory is used to obtain the kinematics and that they do not include the effect of diffraction. In other words: the initial wave field is wrong. But it is thought that results resembling the experiments, are obtained in less time than when the simulation is started from rest.

At the inflow, analytical wave theory is used during the course of the simulation. We have used 5th-order Stokes theory [15] to determine the surface elevation and the kinematics at the boundary. At the outflow, a Sommerfeld equation with $c = 18.16m/s$, was used to absorb outgoing waves.

The numerical results are compared to the experimental time traces starting at $t = 1104s$. During the following 35 seconds the signal is fairly regular. The comparison is shown in Figs. 7.3 and 7.4: Fig. 7.3 shows the surface elevation at the locations indicated in Fig. 7.2 and Fig. 7.4 shows the pressure over time as a result of consecutive wave impacts.

The numerical results are in reasonable agreement with the experiment. The agreement of the impact pressures with the experiments and the signal of the wave probe in between columns, is better than the agreement of the surface elevation in front of and behind the structure. A reason for this may be the initial wave field that was not similar to the wave field in the experiments at $t = 1104s$.

Although the results resemble the experiment fairly well, a converged solution was not yet obtained. Unfortunately, it will be some time before desktop PCs can deal

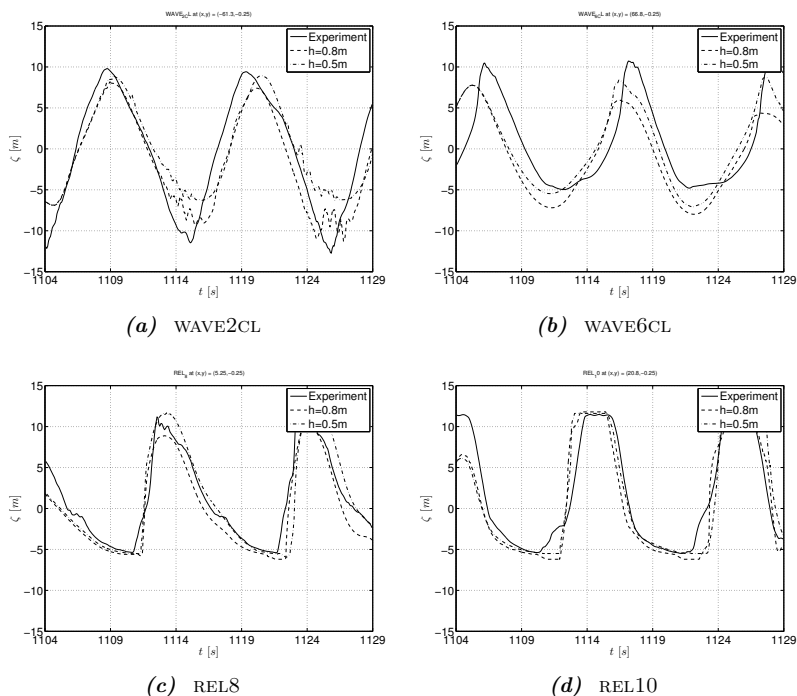


Figure 7.3: Numerical results of the surface elevation for two grid resolutions. Numerical results are compared to the experimental results of test 202003.

with an even larger number of cells. A smaller mesh size may be possible when the domain size is decreased and the boundaries of the domain are positioned closer to the structure.

7.3.2 Sensitivity study

The aim of the sensitivity study is to observe how the results change when different wave absorbing boundary conditions are used and when the domain boundary is located closer to the structure.

The test that was used in this section, is 202002. The setup of the simulation is similar to the setup in the previous section. Here, however, the mesh was kept constant at $\Delta x = 1.6m$ and the size of the domain in x -direction now equals two times $L = 131m$.

We compare the results of the following variations:

- GABC at the inflow and at the outflow, when the boundaries are at $x = \pm L$
- Sommerfeld at the outflow with the boundaries at $x = \pm L$

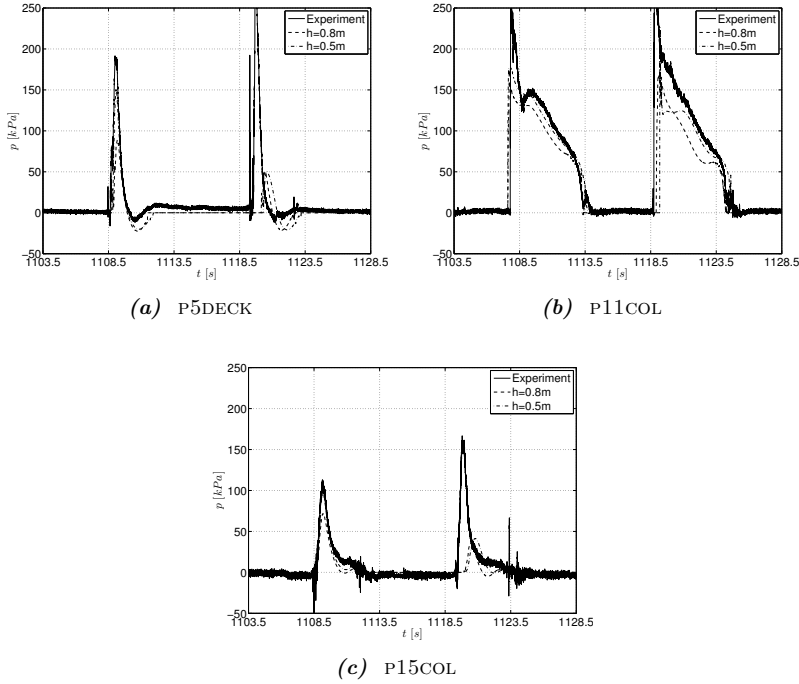


Figure 7.4: Numerical results of the pressure for two grid resolutions. Numerical results are compared to the experimental results of test 202003.

- GABC at the inflow and at the outflow, when the boundaries are at $x = \pm 0.5L$
- Sommerfeld at the outflow with the boundaries at $x = \pm 0.5L$

The starting time of the simulations was $t = 1104s$ and the comparisons are made over a time of 35 seconds. In the Sommerfeld condition, the phase velocity was set to $c = 14.58m/s$. The results are shown in Fig. 7.5.

These numerical experiments were intended to show that the GABC gives stable results for 3D simulations. And they were meant to show that the GABC gives similar results to the implementation of the Sommerfeld relation. For regular waves it cannot be expected that the GABC performs better than the Sommerfeld relation: for the frequency the latter has been tuned to, the GABC might even give results worse than the Sommerfeld condition, but only at this frequency and no more than 2%.

The results, however, were similar at the outflow end of the domain. Compared to a simulation with a Sommerfeld relation at just the outflow end of the domain, the simulations with the GABC differed in one important respect: the inflow end of the domain was generating waves and preventing re-reflection at the same time. The absorbing nature of the inflow boundary is important for this type of simulation.

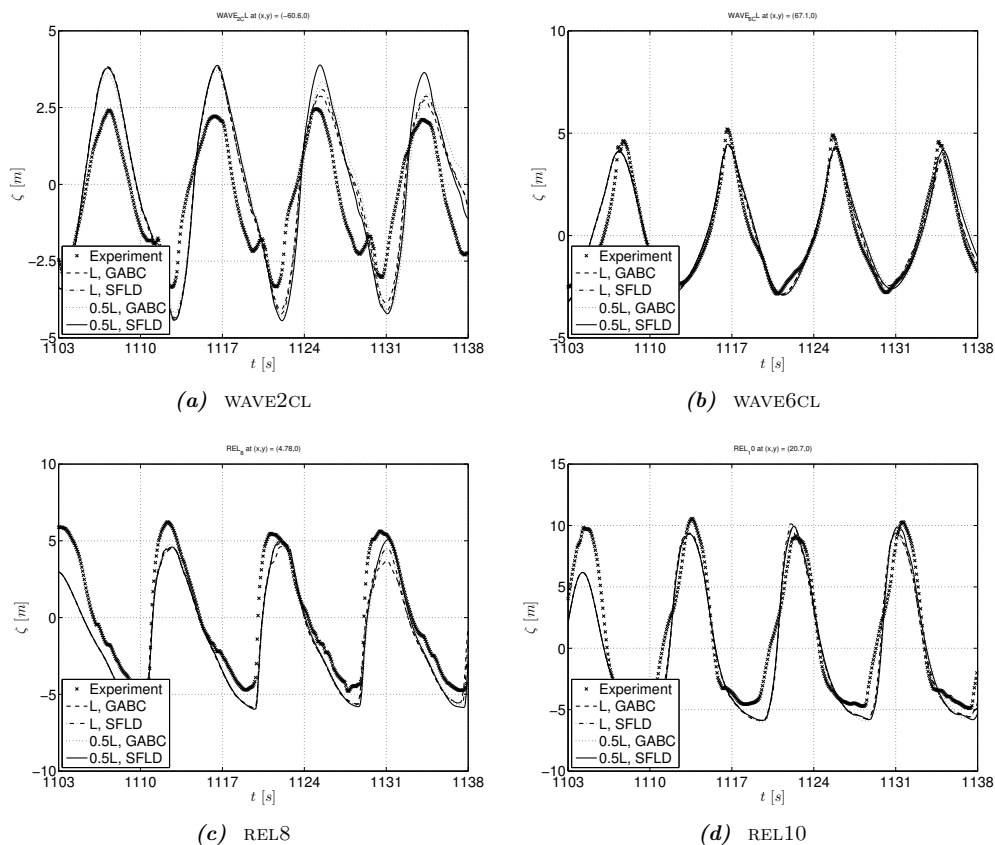


Figure 7.5: Numerical results of the surface elevation versus experimental results of test 202002. GABC and Sommerfeld boundary conditions are compared. And the distance of the boundary to the structure has been varied from one wave length to half a wave length.

One can tell from Fig. 7.5a that in the latter stages of the simulation there is a clear difference between the Sommerfeld-results with the boundary at $0.5L$ and the GABC-results with the boundary at $0.5L$. The difference is due to re-reflections and they are starting to influence the results at REL_10, see Fig. 7.2. The differences due to re-reflection will only become larger as the simulation time increases.

7.3.3 Irregular wave simulation

In the previous sections, simulations were performed that started from a developed wave field (of which it was mentioned that it was wrong). The simulations were compared to experimental results starting at an arbitrary moment in time. At this time,

multiple waves will have passed the structure causing wave diffraction and reflection of the diffracted waves at the tank walls. With this approach, the comparison between numerical results and the experiments can never entirely be without differences.

In this section, we try to start the simulation from a situation at rest and an initially undisturbed free surface. The nonlinear potential flow model, described in section 5.2.2, is used to propagate waves from the wave board to the structure. The free surface and kinematics at a certain location in the the potential flow model are used to drive the waves at the boundary of the ComFLOW domain. In this approach, initialization errors are reduced to null.

For the experiment, test 202006/401009 was used. In itself this test is not an irregular wave test, but the first couple of waves, before the wave signal starts to become regular, satisfy an irregular and somewhat steep pattern; the loading on the structure as a result of these waves will be substantial.

Nonlinear potential flow simulation

The nonlinear potential flow model, coined FDFEM in this document, is run with a grid distance of $5m$ in horizontal direction. The total size of the domain in horizontal direction equals $10,000m$ with a pressure damping beach at the downstream side and a pivoting wave board at the upstream side of the domain.

In vertical direction the domain is $150.0m$ deep and 14 cells with significant grid stretching were used; at the free surface the vertical cell size was $1.65m$ and the bottom the cell size was $21.4m$. Note that the depth of the domain is not the same as in the experiment. This is due to stability issues with the FDFEM model, see also [34]. By chance, the described setup of the simulation could compute until the end. Grid improvements and an increased depth, however, all lead to instabilities.

The results of the FDFEM simulation at location $x = 5315m$ are shown in Fig. 7.6. The results are compared to the experimental results of an undisturbed wave test over 120 second starting at $t = 580s$. Unfortunately, the exact position of the wave probe with respect to the wave board is unknown. The current location is our best estimate found after several simulations.

The larger waves in the FDFEM simulation are slightly steeper, but otherwise the signals are almost identical. There can be three reasons for the differences between the FDFEM simulation and the experiment. Firstly, the depth in the simulation is smaller than in the experiment. Secondly, there may have been some dissipation in the experiment as a result of wave breaking or interaction with the side walls of the basin. And finally, the resolved surface elevation may not have been a converged solution. These statements cannot be verified because of reasons stated above.

2D Simulation of the undisturbed wave

To check how well the representation of the free surface in ComFLOW compares to the free surface in FDFEM, a 2D simulation in ComFLOW, with the kinematics from FDFEM, is compared to the original free surface in the potential flow simulation.

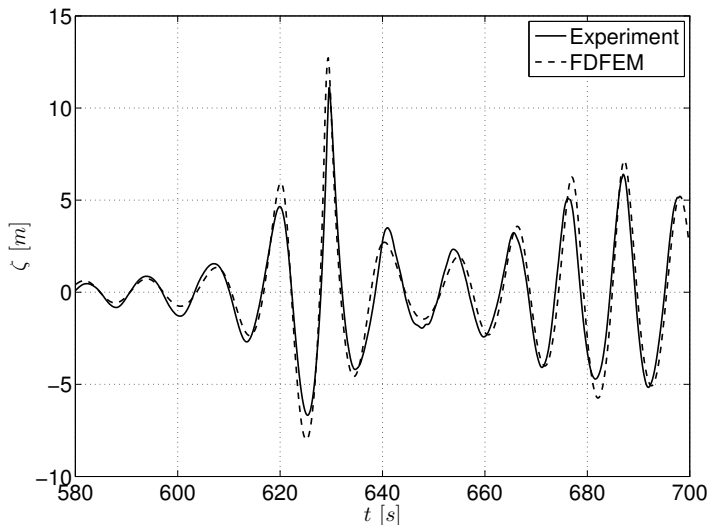


Figure 7.6: Comparison of the free surface at $x = 5315m$ between a FDFEM simulation and the results of test 202006/401009.

The downstream boundary in ComFLOW is located at $x = 5156m$. This is where the kinematics from FDFEM are used. The outflow boundary is positioned at $x = 5356m$. Here, the GABC is used to reduce reflection of waves back into the domain.

In ComFLOW, 300 cells were used in horizontal direction without any stretching. In the vertical direction 75 cells were applied with a stretching coefficient of 5% and the focus point of the stretching at the mean surface level $z = 0$.

In Fig. 7.7 the free surface at $x = 5315m$ in ComFLOW is compared with the free surface in the potential flow model. The ComFLOW simulation is started at $t = 580s$ and lasts for 120 seconds.

The initial steep wave in ComFLOW is higher than the same wave in FDFEM. In the ComFLOW simulation there has been some overturning when that first wave reaches its highest point. The subsequent wave in ComFLOW is slightly lower than the one in FDFEM. This is to be expected, because numerical dissipation in ComFLOW will affect the largest waves the most. The remainder of the free surface signals compares reasonably well.

3D Simulation

The dimensions of the domain in x and z -direction have remained the same for the 3D simulation. But in the y -direction the boundaries of the domain were chosen to coincide with the basin walls, each positioned $100m$ away from the center of the

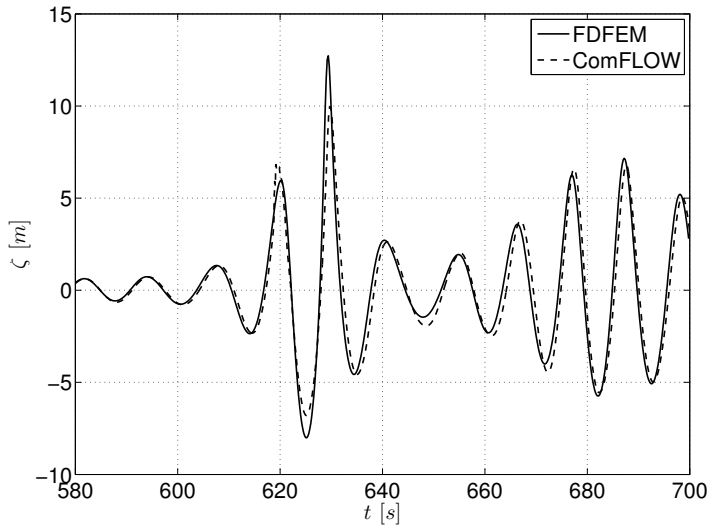


Figure 7.7: Comparison of the free surface at $x = 5315m$ between a FDFEM simulation and a ComFLOW simulation.

structure. The center position of the structure, measured with respect to position of the wave board, was fairly uncertain. Our best estimate is $x = 5306m$.

In x -direction the domain was $300m$ large and 200 cells were used, without grid stretching. In y -direction the domain was $200m$ and 75 cells were used with a stretching factor of 2%, starting at the center of the structure. In vertical direction 75 cells were used from the bottom at $z = -150m$ to the top of the domain at $z = 20m$. In z -direction a stretching factor of 5% was used.

The GABC was used at the downstream boundary but not at the upstream boundary. Fig. 7.8 shows the free surface that was determined in the 3D simulation in several snap shots. Note that the first wave in 7.8a is breaking; it is unsure if this wave was also breaking in the experiment.

The free surface has been compared to the 202006 experiment at several wave probe locations. Fig. 7.9 shows the surface elevation as a function of time for wave probes along the center line of the structure.

The surface elevation in the simulation is too high at the time of the first high wave and the resulting first impact with the structure. At the time of the second step wave the free surface is lower than in the experiment. This is expected behaviour: in the 2D simulation, where ComFLOW was indirectly compared to the experiment, it was already noticed that the first step wave in the simulation was too high and that the second step wave was not high enough.

The same results can be found in the outputs of the pressure sensors. The result for three different transducers are shown in Fig. 7.10. There the first impact leads to a

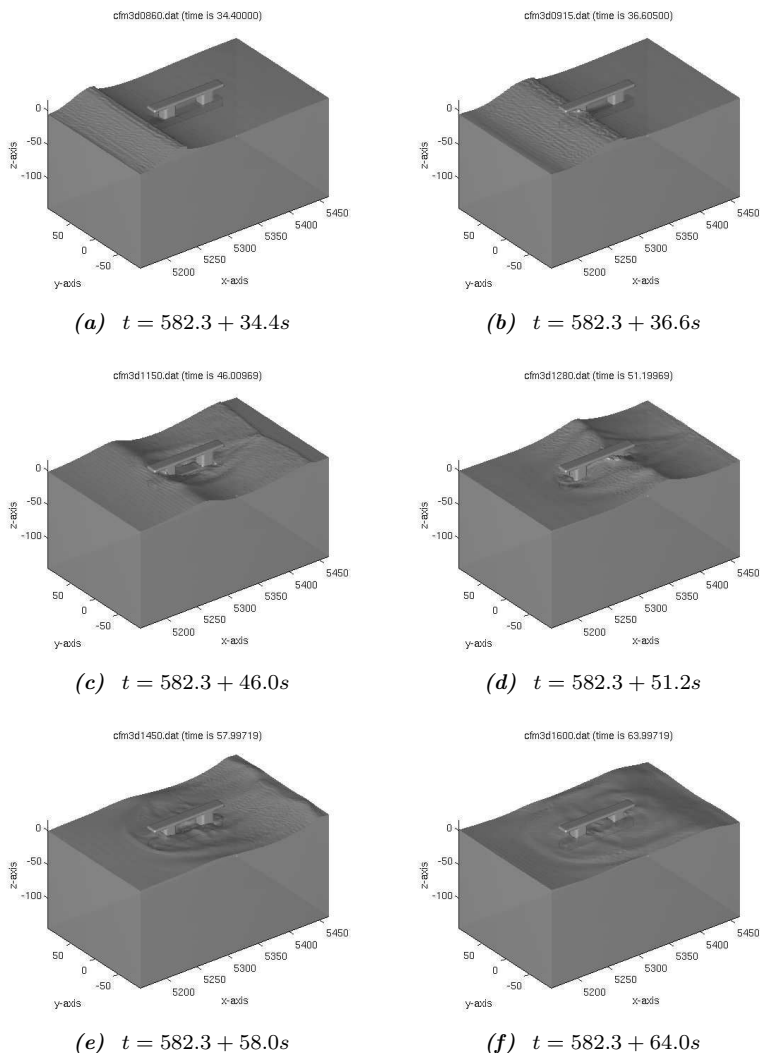


Figure 7.8: Snapshots of the simulation at several time instances.

pressure, which is too high, and the second impact shows a pressure variation that does not come high enough.

7.4 Discussion

Pressures from the simulation compare well to the experiments, albeit that they have to be corrected for the difference between the wave signal and the numerical input

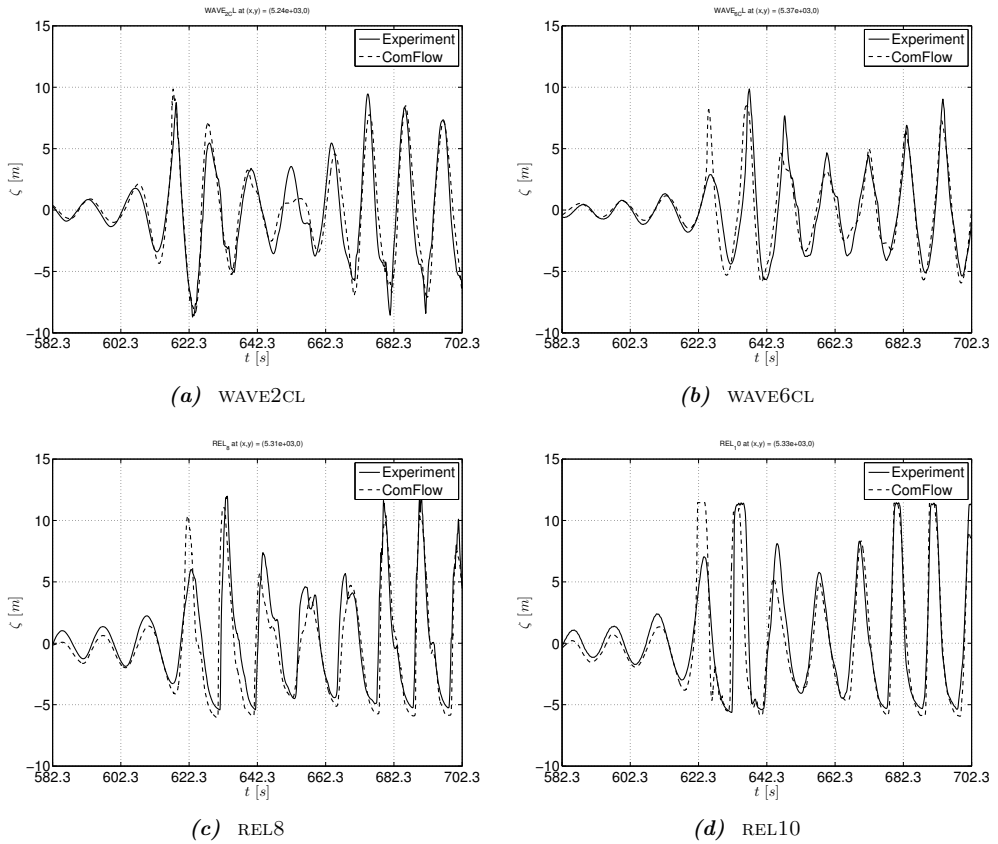


Figure 7.9: Numerical results of the surface elevation compared to the experimental results of test 202006.

signal determined with ComFLOW or FDFEM or a combination of the two. This seems fairly logical: if the input signal is not entirely correct, the output signals can never be perfect either.

Fair comparison between COMFLOW and the experiment is only possible if we can get the incoming wave signal correctly into the computational domain. The principle has been demonstrated with FDFEM in this thesis, but we believe that research should be devoted to an accurate and stable far field solver that can be used together with COMFLOW.

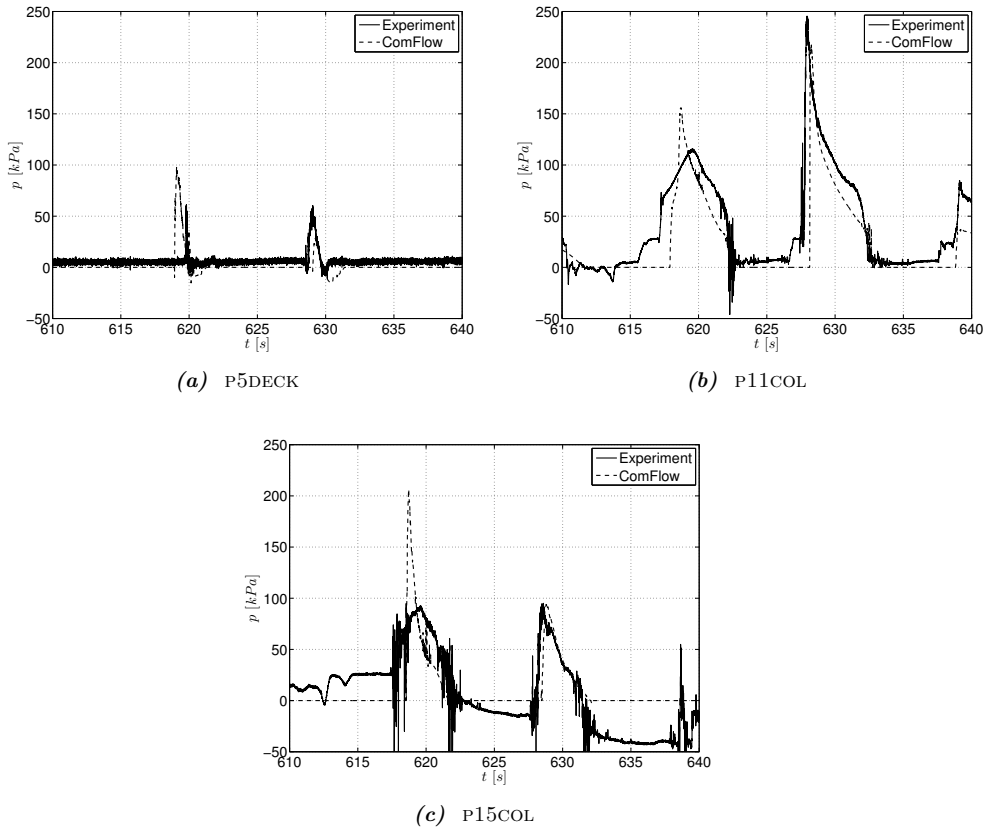


Figure 7.10: Numerical results of the pressure compared with the experimental results of test 202006.

Chapter 8

Concluding remarks

The incorporation of the numerical method in this thesis into COMFLOW yields a versatile and fast program, which is dedicated to simulating wave impacts on offshore structures where the free surface can take on any which shape. Comparison to results of experiments, designed especially for validation, has shown that it is accurate in terms of (impact) pressures and surface elevations near the structure. The method remains stable, even for highly distorted free surfaces as a result of wave breaking or otherwise overturning waves.

The discrete equations that are solved, are based on the Navier-Stokes equations for conservation of mass and momentum. A cut-cell method is incorporated to describe the structure's geometry. A very simple discretization without regard for cut cells has been adopted for the diffusive term in the momentum equation; this is justified because the method is not intended for an accurate representation of boundary layers or turbulent effects. Violent free surface impacts are dominated by convection and in coarse grid simulations used in engineering, diffusion is dominated by artificial viscosity due to upwind discretization of the convective term. The discretization of the diffusive term will only become important for very fine grids.

Energy dissipation in wave simulations

Artificial dissipation, unfortunately, also affects the simulation of standing and propagating waves, where it becomes apparent in the loss of wave height. As standing waves oscillate in time or propagating waves travel over distances in the order of a wave length, energy is lost to dissipation and the wave height becomes smaller. The effect of artificial dissipation is stronger in steeper waves. The dissipation was found to be caused by both the artificial viscosity mentioned above, and the free surface displacement algorithm to almost equal extent.

The donor-acceptor algorithm used in the Volume-of-Fluid method can be interpreted as an upwind discretization of the free surface convection and upwind discretization is known to induce dissipation. The energy dissipation can be reduced by either a

more accurate free surface reconstruction (piecewise linear in this thesis), or by a more accurate discretization of the convective term in the momentum equation. The combination of both gives good results and reduces energy dissipation to an even greater extent.

The path to improvement seems clear. Now, piecewise linear reconstruction of the free surface is used. A continuous, perhaps even quadratic, reconstruction of the free surface can be feasible and may lead to better results.

Generating and absorbing waves

In this research, wave kinematics obtained from nonlinear stream function or potential theory are imposed as Dirichlet condition for the velocity at the boundary. Rienecker-Fenton theory is used to generate steep regular waves and an external potential flow method is used to generate irregular waves. Proper simulation of waves in a numerical domain, however, is impossible without adequate measures to prevent wave reflection.

A common approach to prevent waves from reflecting, is to add a numerical dissipation zone to the calculation domain, in which the wave height is reduced over distance until there is none left to reflect. A dissipation zone, in theory, requires several wave lengths' distance to dissipate all wave energy and this takes up undesired computation time and memory. Alternatively, local absorbing boundary conditions can be employed to prevent reflection. Local ABCs do not require extending the domain and are therefore more efficient. There is an abundance of literature on the subject of ABCs, but the seemingly best performing methods were found to be inadequate for use in practical simulations that actually resemble anything found out at sea. ABCs in the literature are either very simple and do not perform well enough, or they are very complex and can only be used in combination with very simple differential equations.

This thesis introduces a newly devised generating absorbing boundary condition that yields truly open boundaries – open to outgoing waves and, at the same time and over the same boundary, open to incoming waves. The starting point for the derivation of the GABC is the Sommerfeld condition, which is perfectly absorbing for one wave component with one propagation velocity. This velocity is specified in the Sommerfeld condition by means of a tuning parameter. It was found that the range of absorbed wave components can be extended by replacing the tuning parameter with an approximation of the linear dispersion relation in terms of the wave number. When second derivatives of the solution variables in the vertical direction are substituted for the wave number, it yields an equation for the GABC giving less than two percent reflection for a range of components. Stability issues loom when the GABC is implemented, but the mechanism, by which instabilities occur, is well understood and stability criteria have been formulated. The stability criteria hardly restrain the absorbing performance of the GABC.

It was found in numerical simulations for irregular waves with the GABC that the reflection coefficient can be as low as 5% for mildly steep waves. This is somewhat higher than the 2% that was derived from theory, but quite comparable to the amount of reflection that is said to be obtained in experimental basins and flumes. The difference between theory and practice here mainly lies in the fact that non-linearity has

not been accounted for in the GABC: bound frequency components do not propagate at phase velocities that can be predicted with linear theory.

When the current formulation of the GABC is included in the system of equations, additional coefficients in the left-hand-side matrix are required. The coefficients are uncommon to default Poisson solvers and therefore a general sparse matrix solver with an ILU decomposition has been used to solve the pressure matrix equation at every time step. The general solver is slower and takes up a lot more memory than specialized, fit-to-purpose ways to obtain the solution to the system.

When research involving the GABC is continued, serious attention is to be devoted to the Poisson solver, because it can make the solution process considerably more efficient in terms of memory and noticeably faster. Since the additional coefficients are only required in the equations for cells along the boundary of the domain, simulations including the GABC should not be much slower than simulations without.

The GABC as is, still, leaves ample room for improvement. The optimization has focused on dispersivity of long crested waves in normal direction to the boundary, but in 3D domains waves can arrive at the boundary under any angle. Waves under an angle with the boundary are not absorbed very well with the current implementation of the GABC and future research involving absorbing boundary conditions will have to take directionality into account.

In the derivation of the GABC, linear potential theory has been used extensively to arrive at the final formulation. It might be possible to include non-linear effects for better performance in simulations with very steep waves. And as a final recommendation it should be noted that the GABC needs to be generalized to include currents. Incorporating the functionality into an extended formulation of the GABC seems possible, but it will require substantial effort.

Comparison to experimental results

It was not necessary to compare numerical results with the GABC to experimental results to demonstrate the absorbing performance. It is, however, required that the numerical method as a whole can be used for practical simulations for the offshore industry. In this thesis, the numerical method is compared to model scale experiments performed at MARIN.

Three dimensional simulations featuring the GABC at the incoming and outgoing wave boundary, were compared to experimental results. The side walls of the domain along the direction of wave propagation were fully reflecting, just as in the experiment itself. A schematized semi-submersible that was kept restrained during the simulations, was positioned in the middle of the domain. As a result of wave diffraction around the semi-submersible, not only wave components with normal incidence to the boundary will be present in the domain, but also wave components under an angle with the boundary.

The GABC is not designed to account for wave directionality, but performs sufficiently accurate up to incident wave angles of around 30 degrees. The absorbing boundaries need to be placed at such a distance that most of the wave components arrive at

the boundary at an angle below 30 degrees. It was found that with the GABC, the domain need not be much larger than the structure inside to obtain results that are very close to the experiment. New development of the GABC is required to place the incoming and outgoing wave boundaries even closer to the structure: it then needs to actively account for the direction of the incident wave components.

Future outlook

Currently, a new STW project involving COMFLOW, with three new PhD students, is being worked on. One of the PhD students is working on improving the GABC by including directional effects. He is also working on the free surface displacement algorithm. During his part of the project he will try to include piecewise linear reconstruction (PLIC) of the free surface in the displacement algorithm.

Another PhD student is working on the convective and viscous part of the momentum equation. His main objective is to make COMFLOW ready for simulating mild turbulent effects, but a advantageous side effect that addresses the recommendations in this thesis is that with a better discretization of the convective part of the momentum equation, the amount of numerical viscosity and, hence, spurious wave energy dissipation is greatly reduced.

The third PhD student has numerical efficiency as his main topic. One of the main disadvantages of a Cartesian grid is that grid refinement extends throughout the entire domain leading to small cells where the represented physics do not require this accuracy. We would like to use small cells near the structure and only near the structure. For this reason, the third project focuses on local grid refinement, in which grid transitions from one to two, or one to three cells can be present.

When the aforementioned project has finished, the main recommendations from this thesis will have been addressed.

Bibliography

- [1] S. Afkhami and M. Bussmann. Height functions for applying contact angles to 2D VOF simulations. *International Journal for Numerical Methods in Fluids*, 57(4):453–472, 2008.
- [2] J. P. Berenger. A Perfectly Matched Layer for the Absorption of Electromagnetic-Waves. *Journal of Computational Physics*, 114(2):185–200, 1994.
- [3] E. Blayo and L. Debreu. Revisiting Open Boundary Conditions from the point of view of Characteristic Variables. *Ocean Modelling*, 9(3):231–252, 2005.
- [4] E. F. F. Botta and M. H. M. Ellenbroek. A Modified SOR Method for the Poisson Equation in Unsteady Free-Surface Flow Calculations. *Journal of Computational Physics*, 60(1):119–134, 1985.
- [5] B. Buchner. *Green Water on Ship-Type Offshore Structures*. PhD thesis, Delft University of Technology, Netherlands, 2002.
- [6] X. Cai, H. P. Langtangen, B. F. Nielsen, and A. Tveito. A finite element method for fully nonlinear water waves. *Journal of Computational Physics*, 143(2):544–568, 1998.
- [7] K. M. Carpenter. Radiation Conditions for the Lateral Boundaries of Limited-Area Numerical-Models. *Quarterly Journal of the Royal Meteorological Society*, 108(457):717–719, 1982.
- [8] E. D. Cokelet. Steep Gravity-Waves In Water of Arbitrary Uniform Depth. *Philosophical Transactions of the Royal Society of London Series A-Mathematical Physical And Engineering Sciences*, 286(1335):183–230, 1977.
- [9] F. Collino and P. Joly. New Absorbing Boundary-Conditions for the Finite-Element Solution of 3D Maxwells Equations. *IEEE Transactions on Magnetics*, 31(3):1696–1701, 1995.
- [10] K. Dgaygui and P. Joly. Absorbing Boundary-Conditions for Linear Gravity-Waves. *SIAM Journal on Applied Mathematics*, 54(1):93–131, Feb. 1994.
- [11] M. Dröge. *Cartesian Grid Methods for Turbulent Flow Simulation in Complex Geometries*. PhD thesis, University of Groningen, Netherlands, 2007.

- [12] M. Dröge and R. Verstappen. A new symmetry-preserving Cartesian-grid method for computing flow past arbitrarily shaped objects. *International Journal for Numerical Methods in Fluids*, 47(8-9):979–985, 2005.
- [13] B. Engquist and A. Majda. Absorbing Boundary-Conditions for Numerical-Simulation of Waves. *Mathematics of Computation*, 31(139):629–651, 1977.
- [14] G. Fekken. *Numerical Simulation of Free-Surface Flow with Moving Rigid Bodies*. PhD thesis, University of Groningen, Netherlands, 2004.
- [15] J. D. Fenton. A 5th-Order Stokes Theory for Steady Waves. *Journal of Waterway Port Coastal and Ocean Engineering-ASCE*, 111(2):216–234, 1985.
- [16] J. Gerrits. *Dynamics of Liquid-Filled Spacecraft*. PhD thesis, University of Groningen, Netherlands, 2001.
- [17] D. Givoli. Non-reflecting boundary conditions. *Journal of Computational Physics*, 94(1):1–29, May 1991.
- [18] D. Givoli. High-order local non-reflecting boundary conditions: a review. *Wave Motion*, 39(4):319–326, Apr. 2004.
- [19] D. Givoli and B. Neta. High-Order Non-Reflecting Boundary Conditions for Dispersive Waves. *Wave Motion*, 37(3):257–271, Mar. 2003.
- [20] D. Givoli and I. Patlashenko. Optimal local non-reflecting boundary conditions. *Applied Numerical Mathematics*, 27(4):367–384, Aug. 1998.
- [21] D. Givoli, I. Patlashenko, and J. B. Keller. Discrete Dirichlet-to-Neumann maps for unbounded domains. *Computer Methods in Applied Mechanics and Engineering*, 164(1-2):173–185, Oct. 1998.
- [22] M. J. Grote and J. B. Keller. Exact Nonreflecting Boundary Conditions for the Time Dependent Wave Equation. *SIAM Journal on Applied Mathematics*, 55(2):280–297, 1995. ISSN 00361399.
- [23] M. J. Grote and J. B. Keller. Nonreflecting Boundary Conditions for Time-Dependent Scattering. *Journal of Computational Physics*, 127(1):52–65, Aug. 1996.
- [24] T. Hagstrom and T. Warburton. A new auxiliary variable formulation of high-order local radiation boundary conditions: corner compatibility conditions and extensions to first-order systems. *Wave Motion*, 39(4):327–338, 2004.
- [25] T. Hagstrom, A. Mar-Or, and D. Givoli. High-order local absorbing conditions for the wave equation: Extensions and improvements. *Journal of Computational Physics*, 227(6):3322–3357, 2008.
- [26] R. L. Higdon. Absorbing Boundary-Conditions for Difference Approximations to the Multidimensional Wave-Equation. *Mathematics of Computation*, 47(176):437–459, Oct. 1986.

- [27] C. W. Hirt and B. D. Nichols. Volume of Fluid (VOF) Method for the Dynamics of Free Boundaries. *Journal of Computational Physics*, 39(1):201–225, 1981.
- [28] L. H. Holthuijsen. *Waves in Oceanic and Coastal Waters*. Cambridge University Press, 2007.
- [29] M. Israeli and S. A. Orszag. Approximation of Radiation Boundary-Conditions. *Journal of Computational Physics*, 41(1):115–135, 1981.
- [30] J. B. Keller and D. Givoli. Exact Non-Reflecting Boundary-Conditions. *Journal of Computational Physics*, 82(1):172–192, May 1989.
- [31] M. S. Kim and W. I. Lee. A new VOF-based numerical scheme for the simulation of fluid flow with free surface. Part I: New free surface-tracking algorithm and its verification. *International Journal for Numerical Methods in Fluids*, 42(7):765–790, 2003.
- [32] K. Kleefsman. *Water impact loading on offshore structures - a numerical study*. PhD thesis, University of Groningen, Netherlands, 2005.
- [33] K. M. T. Kleefsman, G. Fekken, A. E. P. Veldman, B. Iwanowski, and B. Buchner. A Volume-of-Fluid based simulation method for wave impact problems. *Journal of Computational Physics*, 206(1):363–393, 2005.
- [34] M. S. Longuet-Higgins and E. D. Cokelet. Deformation of Steep Surface-Waves on Water. 1. Numerical Method of Computation. *Proceedings of the Royal Society of London Series A-Mathematical Physical and Engineering Sciences*, 350(1660):1–26, 1976.
- [35] E. Loots. *Fluid-Structure Interaction in Hemodynamics*. PhD thesis, University of Groningen, Netherlands, 2003.
- [36] G. Meskers. Realistic Inflow Conditions for Numerical Simulation of Green Water Loading. Master’s thesis, Delft University of Technology, 2002.
- [37] J. J. Monaghan. Simulating Free-Surface Flows With SPH. *Journal of Computational Physics*, 110(2):399–406, 1994.
- [38] J. N. Newman, B. Sortland, and T. Vinje. Added Mass and Damping of Rectangular Bodies close to the Free-Surface. *Journal of Ship Research*, 28(4):219–225, 1984.
- [39] I. Orlanski. Simple Boundary-Condition for Unbounded Hyperbolic Flows. *Journal of Computational Physics*, 21(3):251–269, 1976.
- [40] A. L. Perkins, L. F. Smedstad, D. W. Blake, G. W. Heburn, and A. J. Wallcraft. A new nested boundary condition for a primitive equation ocean model. *Journal of Geophysical Research-Oceans*, 102(C2):3483–3500, Feb. 1997.
- [41] W. J. Rider and D. B. Kothe. Reconstructing volume tracking. *Journal Of Computational Physics*, 141(2):112–152, Apr. 1998.

- [42] M. M. Rienecker and J. D. Fenton. A Fourier Approximation Method for Steady Water-Waves. *Journal of Fluid Mechanics*, 104(MAR):119–137, 1981.
- [43] J. E. Romate. The Numerical-Simulation of Nonlinear Gravity-Waves. *Engineering Analysis With Boundary Elements*, 7(4):156–166, 1990.
- [44] L. W. Schwartz and J. D. Fenton. Strongly Non-Linear Waves. *Annual Review of Fluid Mechanics*, 14:39–60, 1982.
- [45] J. Skourup, K. F. Cheung, H. B. Bingham, and B. Buchmann. Loads on a 3D body due to second-order waves and a current. *Ocean Engineering*, 27(7):707–727, July 2000.
- [46] A. Sommerfeld. *Partial differential equations in physics*. Academic Press, 1949.
- [47] S. V. Tsynkov. Numerical solution of problems on unbounded domains. A review. *Applied Numerical Mathematics*, 27(4):465–532, Aug. 1998.
- [48] A. R. Van Dongeren and I. A. Svendsen. Absorbing-Generating Boundary Condition for Shallow Water Models. *Journal of Waterway Port Coastal and Ocean Engineering-ASCE*, 123(6):303–313, 1997.
- [49] V. Venkatakrisnan. Perspective on unstructured grid flow solvers. *AIAA Journal*, 34(3):533–547, 1996.
- [50] G. K. Verboom and A. Slob. Weakly-Reflective Boundary-Conditions for 2-Dimensional Shallow-Water Flow Problems. *Advances in Water Resources*, 7(4):192–197, 1984.
- [51] R. W. C. P. Verstappen and A. E. P. Veldman. Symmetry-preserving discretization of turbulent flow. *Journal of Computational Physics*, 187(1):343–368, 2003.
- [52] A. Voogt, T. Bunnik, and R. Huijsmans. Validation of an analytical method to calculate wave setdown on current. *Proceedings of the 24th International Conference on Offshore Mechanics and Arctic Engineering - 2005 - Vol 1, Pts A and B*, pages 875–879, 2005.
- [53] P. R. Wellens, J. A. Pinkster, A. E. R. Veldman, and R. H. M. Huijsmans. Numerical wave run up calculation on GBS columns. *Proceedings of the seventeenth International Offshore and Polar Engineering Conference*, pages 2200–2206, 2007.
- [54] R. Wemmenhove. *Numerical Simulation of Two-Phase Flow in Offshore Environments*. PhD thesis, University of Groningen, Netherlands, 2008.
- [55] J. H. Westhuis. *The Numerical Simulation of Nonlinear Waves in a Hydrodynamic Model Test Basin*. PhD thesis, University of Twente, 2001.

Appendix A

Potential theory for waves

Consider the Laplace equation:

$$\nabla^2\Phi = 0, \quad (\text{A.1})$$

with the following linearized boundary conditions:

$$\frac{\partial\Phi}{\partial z} = 0 \quad \text{at } z = -h, \quad (\text{A.2})$$

$$\frac{\partial\Phi}{\partial t} + g\zeta = 0 \quad \text{at } z = 0, \quad (\text{A.3})$$

$$\frac{\partial\zeta}{\partial t} - \frac{\partial\Phi}{\partial z} = 0 \quad \text{at } z = 0. \quad (\text{A.4})$$

Assuming periodic behaviour in horizontal space and time, a solution to the system of equations above equals:

$$\Phi = \frac{ag}{\omega} \frac{\cosh k(h+z)}{\cosh kh} e^{i(\omega t - kx)}, \quad (\text{A.5})$$

in which ω and k are related by the dispersion relation:

$$\omega^2 = kg \tanh kh. \quad (\text{A.6})$$

Eq. A.5 is the propagating wave mode solution to the system of equations in A.1 and A.4. Other solution modes, however, also satisfy the system. If $k = -ik_i$ is substituted in A.5 and A.6, then the following is obtained:

$$\Phi = \frac{ag}{\omega} \frac{\cos k_i(h+z)}{\cos k_i h} e^{i(\omega t)} e^{-k_i x}, \quad (\text{A.7})$$

and:

$$\omega^2 = -k_i g \tan k_i h. \quad (\text{A.8})$$

This is the solution for evanescent wave modes and the dispersion relation that goes with these modes.

During our work with the absorbing boundary condition, it was found that there is another type of solution that satisfies the system of equations:

$$\Phi = \frac{ag \cos k_i(h+z)}{\alpha \cos k_i h} e^{\alpha t} e^{-k_i x}, \quad (\text{A.9})$$

with the dispersion relation:

$$\alpha^2 = k_i g \tan k_i h. \quad (\text{A.10})$$

These are modes that, depending on the sign of α , either grow or fade away. We have called them 'spurious' modes and it is imperative for stability that in numerical simulations the sign of α is always negative.

Appendix B

Reflection coefficient

Consider the Sommerfeld equation applied to a potential function Φ_j :

$$\left(\frac{\partial}{\partial t} + c \frac{\partial}{\partial n}\right) \Phi_j = 0 \text{ for } j = 1, 2, \dots, N. \quad (\text{B.1})$$

In (B.1), c is a tuning parameter and j is an index to identify propagating waves modes with different frequencies ω_j . The boundary condition has been formulated in normal direction to the boundary.

The Sommerfeld equation is an absorbing boundary condition for waves. In this section, we will derive the reflection coefficient for different types of wave modes. The following two wave modes can be identified:

- propagating wave modes
- evanescent wave modes.

Propagating wave modes

Suppose that at frequency ω_j , we can identify one outgoing and one incoming wave component. Then, potential function Φ_j is equal to:

$$\Phi_j = \Phi_j^{out} + \Phi_j^{in} \text{ for } j = 1, 2, \dots, N, \quad (\text{B.2})$$

where $\Phi_j^{out} = A_j^{out} \exp i(\omega_j t - k_j n)$ and $\Phi_j^{in} = A_j^{in} \exp i(\omega_j t + k_j n)$. A_j^{out} and A_j^{in} are the amplitudes of the respective wave modes.

Outgoing wave modes leave the domain over the boundary in the direction of n . The incoming wave mode is triggered by the outgoing wave mode when boundary condition (B.1) is not perfectly tuned to wave mode j . This is what we call reflection. The reflection coefficient is found from the quotient of incoming and outgoing wave mode amplitude.

To obtain the reflection coefficient, the following derivatives are required:

$$\begin{aligned}\frac{\partial\Phi_j}{\partial t} &= i\omega_j\Phi_j \\ \frac{\partial\Phi_j^{out}}{\partial x} &= -ik_j\Phi_j^{out} \\ \frac{\partial\Phi_j^{in}}{\partial x} &= ik_j\Phi_j^{in}\end{aligned}\tag{B.3}$$

Substitution of (B.3) into Eq. (B.1) and evaluation of the obtained expression at $x = 0$ yields:

$$(ck_j - \omega_j)A^{out} - (ck_j + \omega_j)A^{in} = 0 \text{ for } j = 1, 2, \dots, N.\tag{B.4}$$

Then, the reflection coefficient is found to be:

$$R = \frac{A^{in}}{A^{out}} = \frac{c - \omega_j/k_j}{c + \omega_j/k_j} \text{ for } j = 1, 2, \dots, N,\tag{B.5}$$

in which ω_j/k_j can be recognized as the expression for the exact phase velocity of a wave mode with frequency ω_j and wave number k_j . The value for the reflection coefficient for propagating wave modes is always between 0 and 1.

Evanescient wave modes

For evanescent wave modes, the same superposition of outgoing and incoming wave mode as for propagating modes is substituted in boundary condition (B.1), which, after manipulation, leads to a reflection coefficient for these modes. Evanescent modes are of the form:

$$\begin{aligned}\Phi_j^{out} &= A_j^{out} \exp(i\omega_j t - k_j n) \\ \Phi_j^{in} &= A_j^{in} \exp(i\omega_j t + k_j n).\end{aligned}\tag{B.6}$$

The difference between evanescent modes and propagating modes is the behaviour in n-direction. Evanescent modes decrease exponentially in space, whereas propagating modes show oscillatory behaviour.

In the boundary condition, the following derivatives need to be evaluated:

$$\begin{aligned}\frac{\partial\Phi_j}{\partial t} &= i\omega_j\Phi_j \\ \frac{\partial\Phi_j^{out}}{\partial x} &= -k_j\Phi_j^{out} \\ \frac{\partial\Phi_j^{in}}{\partial x} &= k_j\Phi_j^{in}\end{aligned}\tag{B.7}$$

Here, the main difference with the propagating modes is that the space derivatives yield $\pm k_j \Phi_j$ instead of $\pm i k_j \Phi_j$. By substituting (B.7) into Eq. (B.1), the following reflection coefficient is obtained:

$$R = \frac{c - i\omega_j/k_j}{c + i\omega_j/k_j} \text{ for } j = 1, 2, \dots, N. \quad (\text{B.8})$$

In relation (B.8), a complex vector divided by its complex conjugate is recognized. The length of the resulting vector is always equal to 1, which can easily be seen by converting (B.8) to polar coordinates: $r \exp -i\varphi / r \exp i\varphi = \exp -2i\varphi$ with φ the phase change given by $\tan^{-1} \omega_j/k_j c$. This means that evanescent wave modes always have a reflection coefficient of 1.

Dankwoord

Het is klaar. Iedereen die wel eens een onderzoekje heeft gedaan, weet echter dat *klaar* vooral betekent dat iemand vindt dat het nu wel genoeg is zo. Dat is meestal niet de onderzoeker.

Voor de inhoud van mijn proefschrift ben ik veel dank verschuldigd aan Mart Borsboom van Deltares. Halverwege mijn tijd als AIO ben ik om inhoudelijke redenen van aanpak veranderd. De aanpak uit mijn eerste twee jaar staat in twee papers, maar daar heb ik in dit proefschrift niet veel tijd en tekst aan besteed. Zonder Mart zou mijn proefschrift daarom leeg zijn; en nagenoeg alles dat er nu in staat heb ik van hem geleerd, al zal hij geen enkele verantwoordelijkheid willen nemen voor de manier waarop ik het heb opgeschreven. Ik vond en vind het leuk om met Mart aan onderzoek te werken, maar ik heb het ook leuk gevonden met hem mijn nieuwe schoenen te verpesten in de kniediepe sneeuw op de heuvels rond Oslo en om met hem naar concerten in de Boerderij te gaan van bands die voor het laatst populair waren in een tijd dat de modernste tablet niet de iPad, maar de kleitablet was.

Naast Mart is ook Arthur Veldman van de Rijksuniversiteit Groningen voor mij onmisbaar geweest. Hij is wat mij betreft de platoonse idee van de hoogleraar, in al zijn aspecten, behalve benaderbaarheid en punctualiteit. Hij is namelijk ook nog eens een zeer warme persoon en hij is altijd op tijd. Als je AIO bent bij Arthur, krijg je het idee dat je deel uitmaakt van een familie. En het moet er als een familie uit hebben gezien als we voor het project weer eens op reis gingen: Arthur in looppas voorop, omdat hij altijd bang is ergens te laat te komen, en zijn gevolg erachteraan.

Aan René Huijsmans van de TU Delft ben ik, naast mijn dank, ook mijn excuses verschuldigd. Hij heeft de ondankbare taak gehad mij te motiveren tot het afronden van mijn proefschrift in een tijd dat ik me veel te druk maakte over mijn werk bij Deltares en over de situatie thuis. Nu het bijna zover is, en mijn verdediging eraan zit te komen, ontstaat bij mij de gedachte dat het toch wel fijn is om zaken af te ronden. René is mede verantwoordelijk voor die gedachte.

Ik wil ook graag Jo Pinkster bedanken, van de TU Delft destijds, maar inmiddels van het florerende bedrijf Pinkster Marine Hydrodynamics, dat hij het na mijn afstuderen met mij aangedurfd heeft als AIO in het COMFLOW-2-project. Ik vind het jammer dat hij mijn tijd als AIO niet uit heeft kunnen zitten, maar ik begrijp heel goed dat nieuwe uitdagingen als ondernemer niet te lijden moeten hebben van de rompslomp uit het (recente) verleden.

Ik heb niet veel werkgevers versleten, in ieder geval voor zover het geschoold werk aangaat, maar ik heb in beide gevallen veel geluk gehad. Ik heb met veel plezier bij de sleeptank van Maritieme Techniek gewerkt. Toen ik net bij Deltares begon, miste ik de koffie om tien uur 's ochtends en om drie uur 's middags vreselijk. Niet vanwege de koffie, want die is bij de TU ook niet te drinken, maar omdat het zo'n prettig platform is voor intercollegiaal overleg. Dank aan Roel, Rina, Hans, Frits, Arthur, Michiel, Lex, Peter Poot, Piet, Alex, Jan en Peter Naaijen voor de koffie. Dank ook aan Guido met wie ik een paar goede avonden in de kroeg heb doorgebracht, al kan ik ze me niet herinneren. En dank aan Pepijn en Evert-Jan, mijn paranimf, met wie ik als vrienden omging.

In Groningen kwam ik altijd met veel plezier bij Rik op bezoek. Ik heb me erg aan Rik kunnen optrekken, omdat hij altijd wel alles op tijd af had. Rik talmt niet, maar raast gewoon door. Succes met je nieuwe baan. Met Roel, mijn 'broer' in Groningen, vind ik het nog steeds erg gezellig. Het is altijd fijn als er na drieëneuhalf uur treinen een kop koffie voor je klaarstaat. Jammer alleen dat je gezwicht bent en we ons tegenwoordig met automatenkoffie moeten behelpen.

Bij Deltares heb ik het gevoel op mijn plaats te zijn, niet het minst vanwege mijn collega's. Twee mensen wil ik graag expliciet noemen. Ik dank Martijn de Jong, omdat hij niet meteen op dag één naar huis is gevlogen toen hij in de gaten kreeg met wie hij drie weken in Zuid-Korea door moest brengen. Ik kijk nog steeds graag naar de foto's van dat avontuur, alle 4000 natuurlijk, niet de samenvatting van slechts 1000 stuks. Daarnaast wil ik Marcel van Gent danken, omdat hij als afdelingshoofd vierkant achter de mensen in zijn groep staat, ook als dat minder vanzelfsprekend is.

Ook onze bovenburen, Marc en Daniëlle, hebben bijgedragen aan dit proefschrift. In mijn eindsprint van jongstleden augustus, die uiteindelijk toch weer een marathon is geworden, hebben zij tijdens de vakantie hun eetkamertafel aan mij ter beschikking gesteld, zodat ik ook overdag aan mijn proefschrift kon werken zonder dat Ben met zijn versie van het verhaal het toetsenbord beroerde. Dank, en we zullen jullie missen als burens.

Mijn dank gaat uit naar mijn clubgenoten, omdat ze me alweer bijna 15 jaar, plus of min een paar maanden – ik geloof toch min een paar maanden – in hun midden dulden. Hard werken is alleen leuk als je af en toe kunt ontspannen; gedurende het weekend of tijdens een weekje bijna-Lapland, of jaarlijks op een vierkante, stalen schuit die zelfs met een kernreactor aan boord de vijf knoop nog niet zal halen. Ik wil Jan-Willem in het bijzonder nog even noemen, omdat hij zich voorafgaand aan een skivakantie door mijn proefschrift heeft weten te worstelen en daarna nog steeds zin had om op reis te gaan. Dank daarvoor.

Aan mijn tijd bij filosofie heb ik leuke vrienden overgehouden. Ik ben erg gesteld op de traditie van *candlelight suppers* met Liesbeth, Jeffrey en Freya, ook al zal het vanwege alle recente gezinsuitbreiding waarschijnlijk steeds vaker een lunch worden zoals de laatste keer. Met Jeffrey, mijn paranimf, heb ik ook menig avond in de kroeg doorgebracht. Nu ik voor een tweede keer in dit dankwoord moet zeggen dat niet alle avonden mij meer even helder voor de geest staan, realiseer ik me dat hier wel eens sprake van een probleem zou kunnen zijn. Wij moeten nodig weer eens naar de kroeg

om dat te vergeten.

Dit is de plek om mijn zusje te zeggen dat we weliswaar tegenpolen zijn, maar dat je me daardoor niet minder dierbaar bent. Ik vind het fijn om te zien dat je het nu zo goed voor elkaar hebt. Ik wil ook graag mijn ouders bedanken, omdat jullie mij altijd mijn gang hebben laten gaan en zelf mijn weg hebben laten kiezen. Ook heb ik op deze manier de gelegenheid stil te staan bij de keren dat jullie voor mij klaarstonden als ik me weer eens in de nesten had gewerkt. Dank. Ik hoop niet dat het ooit nodig is, maar ik zal er zijn als jullie een beroep op mij moeten doen.

Lieve Ben, klein begonnen en nu ben je alweer zo'n grote vent. Je had je eigen tempo, maar de laatste tijd kan ik je nauwelijks bijhouden. Je maakt het me makkelijk een trotse papa te zijn. Lieve Bernadette, ik mopper weleens dat je me van mijn werk houdt, maar je bent de fijnste afleiding die ik me kan wensen. Er is nogal wat gebeurd sinds ik je ken en we hebben ons niet uit het veld laten slaan. Dat geeft vertrouwen voor de toekomst die we binnenkort met ons vieren tegemoet gaan. Alles met jou lijkt zo vanzelfsprekend en dat is nu juist zo bijzonder. Dank dat je me zo achter de broek hebt gezeten de laatste maanden; zonder jou was het niet gelukt.

Curriculum Vitae

Petrus Reinier (Peter) Wellens was born on 19 May 1979 in Rotterdam, where he has lived for most of his life, and currently still lives with his partner and son. He received his gymnasium diploma from Scholengemeenschap Hugo de Groot in 1997, before commencing his studies.

Peter studied Civil Engineering at Delft University of Technology, specializing in Off-shore Engineering, and studied philosophy at Erasmus University Rotterdam. In 2005, he started work at Delft University of Technology as a PhD-student with financial support from STW.

His most recent employer, since the first of January 2009, is Deltares. At Deltares, Peter focusses on research and advice concerning numerical modelling and experimental work in the field of Coastal Structures and Waves. He is Deltares' project leader for the COMFLOW-3 Joint Industry Project and one of two programme leaders for the Software programme in the theme 'Bouwen in de Delta'. He is also part of the team that coordinates the EC-funded HYDRALAB network.